TRANSMIT FIELD PATTERN CONTROL FOR HIGH FIELD MAGNETIC RESONANCE IMAGING WITH INTEGRATED RF CURRENT SOURCES

A Dissertation

by

KRISHNA NAGARAJ KURPAD

Submitted to the Office of Graduate Studies of
Texas A&M University
in partial fulfillment of the requirements for the degree of

DOCTOR OF PHILOSOPHY

August 2004

Major Subject: Electrical Engineering

TRANSMIT FIELD PATTERN CONTROL FOR HIGH FIELD MAGNETIC RESONANCE IMAGING WITH INTEGRATED RF CURRENT SOURCES

A Dissertation

by

KRISHNA NAGARAJ KURPAD

Submitted to Texas A&M University
in partial fulfillment of the requirements
for the degree of

DOCTOR OF PHILOSOPHY

Approved as to style and content by:

Steven M. Wright (Chair of Committee)	Robert D. Nevels (Member)
Jay D. Humphrey (Member)	Aydin Karsilayan (Member)
Ed B. Boskamp (Member)	Chanan Singh (Head of Department)

August 2004

Major Subject: Electrical Engineering

ABSTRACT

Transmit Field Pattern Control for High Field Magnetic Resonance Imaging with Integrated RF Current Sources. (August 2004)

Krishna Nagaraj Kurpad, B.E., University of Mysore

Chair of Advisory Committee: Dr. Steven M. Wright

The primary design criterion for RF transmit coils for MRI is uniform transverse magnetic (B_1) field. Currently, most high frequency transmit coils are designed as periodic, symmetric structures that are resonant at the imaging frequency, as determined by the static magnetic (B_0) field strength. These coils are excited by one or more voltage sources. The distribution of currents on the coil elements or rungs is determined by the symmetry of the coil structure. At field strengths of 3T and above, electric properties such as the dielectric constant and conductivity of the load lead to B_1 field inhomogeneity due to wavelength effects and perturbation of the coil current distribution from the ideal. The B_1 field homogeneity under such conditions may be optimized by adjusting the amplitudes and phases of the currents on the rungs. However, such adjustments require independent control of current amplitudes and phases on each rung of the resonant coil. Due to both the strong coupling among the rungs of a resonant coil and the sensitivity to loading, such independent control would not be possible and B_1 homogeneity optimization would involve a time consuming and impractical iterative

procedure in the absence of exact knowledge of interactions among coil elements and between the coil and load.

This dissertation is based on the work done towards the design and development of a RF current source that drives high amplitude RF current through an integrated array element. The arrangement is referred to as a current element. Independent control of current amplitude and phase on the current elements is demonstrated. A non-resonant coil structure consisting of current elements is implemented and B_1 field pattern control is demonstrated. It is therefore demonstrated that this technology would enable effective B_1 field optimization in the presence of lossy dielectric loads at high field strengths.

To my late grandmothers,

Smt. K. Subbamma & Smt. Padmavathi Ramamurthy

and my maternal grandfather,

Shri. V. Ramamurthy

ACKNOWLEDGEMENTS

I would like to thank, first and foremost, Dr. Steve Wright, my advisor and teacher for his tremendous support, understanding and belief in my work. I would also like to thank him for introducing me to the exciting field of MRI and for encouraging me to think on my own.

Next, I would like to thank Dr. Eddy Boskamp, my advisor at GE Medical Systems, Waukesha, for being a wonderful teacher and patiently answering all my questions in spite of his busy schedule.

Aniruddha Tiwari and Deependra Gangakhedkar selflessly helped me out when I broke my ankle. I thank them profusely for their help.

I would like to thank David Brown at MRSL and Leroy Blawat at ASL for the many enlightening discussions on RF circuit design. I would also like to thank my lab mate, Hyokwon Nam, for helping me out with my experiments.

My brother, Shekar Kurpad, and sister-in-law, Kalpa Vithalani, have been a huge source of support throughout these past seven years. I thank them both for being there for me whenever I needed their support.

My parents, K. Nagaraj and Geetha Nagaraj, have always encouraged me to excel in academics. Their support and encouragement have meant a lot to me and they are a huge part of whatever I am and become in life.

Last, but not least, this work would not have been possible without the patience, understanding and love of my beautiful wife, Prathibha. Words would only trivialize the love and respect that I have for her.

TABLE OF CONTENTS

LIST OF TABLES

LIST OF FIGURES

FIGURE Page

CHAPTER I

INTRODUCTION

I.1. Background information on MRI

Magnetic Resonance Imaging (MRI) is a tomographic imaging technique that is mainly used to image the human anatomy. It is based on the principle of Nuclear Magnetic Resonance (NMR), a physical phenomenon that was discovered separately by Felix Bloch and Edward Purcell in 1946. The first application of the principle of NMR was in NMR spectroscopy. Paul Lauterbur, in 1973, obtained the first images of small test tube samples using magnetic field gradients (1). This signaled the birth of MRI and today, it is the preferred modality of imaging for medical diagnostic purposes.

From a system perspective, the MRI scanner consists of three major hardware components: 1) The magnet, 2) The gradient subsystem and 3) The RF subsystem. The magnet is used to provide an external static magnetic field that sets the frequency of precession of the nuclear magnetic moment at the so called Larmour frequency and also aligns the resultant magnetic moment vector of every volume element, called voxel, in the selected imaging volume in a specific direction, conventionally referred to as the ‘z’ direction. The gradient subsystem provides magnetic field gradients that serve to

---

This dissertation follows the style and format of Magnetic Resonance in Medicine.

spatially localize the voxels depending on their precessional frequencies and relative phase. The RF subsystem is used to generate and detect the NMR signal.

I.2. Motivation

Ever since the invention of MRI three decades ago, the objective of RF coil design has been to achieve highly homogeneous transverse magnetic field and high sensitivity. The transverse magnetic field in conventionally referred to as the B_1 field in MRI, though B is the standard symbol for the magnetic flux density and H is the standard symbol for magnetic field intensity. In the context of transmit coil design, B_1 field homogeneity is a primary requirement for the RF coil to be acceptable whereas high sensitivity is a desired feature of a good transmit coil, which reduces power demands on the RF power amplifier. These objectives have been traditionally met by implementing symmetric, periodic structures that are resonant at the imaging frequency or Larmour frequency. These structures are multi-modal due to the periodicity of their structure. The RF power amplifier has traditionally been used as a voltage source to excite the resonant structure at the Larmour frequency. The current distribution on the coil conductors would therefore be determined by the symmetry of the coil structure.

The most popular resonant coil to date is the birdcage coil first proposed by Hayes *et al* (2). At field strengths below 1.5T, birdcage coils efficiently generate highly homogeneous B_1 fields in large imaging volumes even in the presence of asymmetrically placed lossy, dielectric loads. This is due to the fact that the wavelength of the field is long compared to the load dimensions and the parasitic capacitances introduced by the

load are negligible compared to the value of the component capacitors that are used to tune the coil to resonance.

At field strengths of 3T and higher, the tuning capacitors required to resonate a coil of the same size become smaller and consequently, the parasitic capacitances become significant in comparison. This results in B_1 field inhomogeneity due to overlapping of resonant modes, called mode mixing (3). Furthermore, the wavelength of the RF field in the load becomes comparable to the load dimensions, leading to formation of interference patterns within the load. These two effects lead to severe B_1 field inhomogeneity. While other resonant coil designs, such as the TEM resonator (4,5), have attempted to address the problem of load-coil interactions through the use of distributed capacitors, dielectric effects have been thought to be a fundamental limitation for high field whole body imaging (6).

The challenges posed by high field imaging in terms of B_1 field homogeneity necessitates a radical shift in the approach to RF transmit coil design. RF coil designs of the future, for high field imaging, would need to possess the ability to control B_1 field patterns in the imaging volume. This would enable optimization of B_1 homogeneity in the presence of lossy, dielectric loads by a simple superposition of a number of field patterns.

This dissertation is a report of work done towards achieving such a coil design. Principles of phased array antennas and active integrated array design have been adapted to the context of MRI. High amplitude RF current sources have been designed, developed and integrated with array elements to form current elements that are well

decoupled from each other, thereby enabling independent control of the amplitude and phase of the B_1 field generated by them. These current elements have then been used in a volume coil configuration and B_1 field pattern control has been demonstrated.

I.3. Organization of the dissertation

A discussion of NMR physics has been avoided in this dissertation as no improvement on the treatment of the subject over those presented by several distinguished authors is likely. This first chapter introduces the reader to some of the pioneers in the field of NMR theory and MRI. The chapter then goes on to discuss the motivation for the research and finally presents the organization of the dissertation.

Chapter II lays the foundation for the research by giving the reader a brief theoretical background on the necessity for uniform B_1 fields, the rationale for high field imaging, the problems it poses for RF coil design and the body of work that has gone into addressing these problems. The chapter ends with a brief overview of the work presented in this dissertation

Chapter III discusses the design, development and testing of an eight channel controller module. The controller module is used to control the amplitude and phase of the RF control voltage that in turn, controls the amplitude and phase of the current on the current element. This chapter presents results showing that the amplitude and phase of the output voltage can be controlled independent of each other.

Chapter IV discusses the design of a high amplitude RF current source as a modification of a classical RF power amplifier design. This chapter discusses the constraints imposed by the parasitic output capacitance of the MOSFET on the current

source operation of the MOSFET, with respect to the rung. Results are presented that show the linear dependence of the rung current amplitude and phase on the amplitude and phase respectively of the RF control voltage. Results are presented to also show the transition of the MOSFET from a current source to a voltage source and conclusions are drawn.

Chapter V describes the construction of an eight channel volume transmit array coil. The controllability of current phase and amplitude on a current element in the presence of a neighboring current carrying element is established. The uncontrolled modal patterns of a TEM coil are reproduced in a controlled manner by adjusting the current phases and amplitudes on the current elements, thus demonstrating B_1 field pattern control.

Chapter VI summarizes the work presented in this dissertation and suggests some areas of interest for future research.

CHAPTER II

BACKGROUND

Radio frequency (RF) coils are used in MRI to transmit RF power into a sample and receive an RF signal, the NMR signal, from the sample. The most important design criteria for transmit and receive coils are respectively, the transverse RF magnetic (B_1) field homogeneity throughout the sample volume and the signal to noise ratio (SNR) of the received signal. This chapter discusses issues relating to the RF transmit coil design, specifically for high field imaging. The discussion begins with a justification for the requirement of B_1 field homogeneity. Next, the rationale for high field imaging along with the problems posed for RF coil design is discussed. This is followed by a discussion of the body of work that has gone into the design of volume coils that attempt to address the problems posed by high field imaging.

II.1. Flip angle, image intensity and contrast

The underlying phenomenon in Magnetic Resonance Imaging has been colorfully described as a choreography of proton spin magnetic moments, controlled by the application of various magnetic fields (7). This is made possible by the property of spin precession about the axis of the applied magnetic field. The angular velocity of precession, expressed in units of radians/second is given by

$$\omega_0 = \gamma B_0 \qquad \text{[II.1]}$$

where γ is the gyromagnetic ratio expressed in units of radians/tesla and B is the magnetic flux density of the applied field, expressed in units of tesla. The hydrogen nucleus, which consists of a single proton, is the most abundantly present in tissue and is most widely used for MRI. The gyromagnetic ratio of a hydrogen nucleus is 267.48 Mrad/T.

The spins of a sample volume can be binned into small volume elements called voxels, depending upon their position in the sample. The voxel size is determined by the desired image resolution and the slice thickness. Each voxel is assumed to have a uniform spin density. When the sample is placed in a static magnetic field, B_0, each voxel develops a net macroscopic magnetization, M_0, in the direction of B_0, which, by convention, is taken to be in the positive z direction. M_0 precesses about the axis of B_0 with angular velocity, ω_0, as given by [II.1]. When a transverse magnetic field, B_1, oriented orthogonal to B_0, and with the same angular velocity, ω_0, is applied for a limited length of time,τ, M_0 precesses about the rotating axis of B_1 through an angle, α. To an observer on the rotating B_1 axis, the flip angle, α is given by

$$\alpha(r) = \int_0^{\tau} \gamma B_1(r,t)\, dt \qquad \text{[II.2]}$$

where $r = (x, y, z)$ defines the position of a voxel in a coordinate system. Equation [II.2] results in the formation of a transverse component of M_0 on the x-y plane denoted by M_{xy}, which induces an exponentially decaying emf in the receive antenna. The implication of [II.2] is that uniform flip angle over the entire imaging plane requires uniform B_1 field over that plane.

The most common and basic pulse sequences used in MRI are the Spin Echo (SE) and the Gradient Echo (GE) sequences. The signal contributed by each voxel due to SE and GE pulse sequences (8) are given by

$$S_{SE}(r,t) \propto \left[M_{xy}(r) \left[1 - \exp\left(\frac{-TR}{T_1(r)} \right) \right] \exp\left(\frac{-TE}{T_2(r)} \right) \right] e^{j\omega t} \qquad \text{[II.3]}$$

$$S_{GE}(r,t) \propto \left[M_{xy}(r) \frac{\left[1 - \exp\left(\frac{-TR}{T_1(r)} \right) \right] \exp\left(\frac{-TE}{T_2^*(r)} \right)}{1 - \exp\left(\frac{-TR}{T_1(r)} \right) \cos\left[\alpha(r) \right]} \right] e^{j\omega t} \qquad \text{[II.4]}$$

where $M_{xy}(r)$ represents the x-y component of the initial longitudinal magnetization in each voxel, $M_z^0(r)$, which is a function of spin density in the voxel at r. $T_1(r)$ is the spin-lattice relaxation time due to the interaction of spins with their surroundings and is characteristic of the molecular structure of the voxel. $T_2(r)$ is the spin-spin relaxation time due to interaction with other spins in the vicinity of the voxel and local B field inhomogeneity. M_z^0 (spin density), T_1 and T_2 are the three most important contrast mechanisms in MRI (9). Pulse sequence parameters, TR and TE are the repetition and echo times respectively, that are used to determine whether the image shows a contrast map predominantly of the spin densities, T_1 relaxation properties or the T_2 relaxation properties of the tissues.

For GE images, an analysis of equation [II.4] for flip angle criterion shows that small tip angle eliminates the influence of T_1 on the image weighting. Only large spatial

variation in the flip angle causes changes in the image weighting. Furthermore, with $M_{xy}^{0} = M_{z}^{0} \sin\left[\alpha(r)\right]$ GE pulse sequence is robust for small variation in flip angle and hence, homogeneity. However, large variations can result in images that are of no diagnostic or analytical value.

For SE pulse sequence, however, it has been shown that $M_{xy}^{0} = M_{z}^{0} \sin^{3}\left[\alpha(r)\right]$ (10). This implies that the signal from each voxel is very sensitive to the local B_1 field amplitude. Small variations in B_1 homogeneity could lead to large contrast variations. Therefore SE pulse sequence is very sensitive to B_1 field variations, requiring a high degree of homogeneity.

Volume RF coils have been used extensively for the generation of uniform B_1 fields. These coils work on the principle that a current distributed as a sinusoidal function of the azimuthal angle, on the surface of an infinitely long cylinder, produces a uniform B_1 field in the imaging volume.

II.2. High field imaging

The interest in high field imaging stems from the fact that the signal intensity (SI) increases significantly with increase in field strength. This is evident from the fact that

$$SI = \left(N \frac{\hbar\omega}{2KT} \right) (\omega_0 M_0) \qquad \text{[II.5]}$$

where SI, the signal intensity increases as the square of the B_0 field (9,11). For a well designed RF coil where the noise is dominated by the sample, the rms noise voltage

increases as the B_0 field. Hence, there is a theoretical linear increase in SNR with the B_0 field. Several researchers have reported a linear increase in the SNR with field strength (12,13).

The increase in SNR has significant advantages in terms of spatial, spectral and temporal resolution. This is because SNR is the fundamental limitation to increased spectral resolution as SNR is linearly proportional to the linear voxel dimension. Since SNR increases as the square root of the number of signal averages, the imaging time for a given SNR is inversely proportional to the sixth power of the linear voxel dimension (14).

Functional MRI (fMRI) is an application of MRI that is used to analyze brain function using blood oxygenation level dependent (BOLD) contrast to detect brain response to specific stimuli (15). Therefore, for accurate analysis, high spatial and temporal imaging resolution is required. Several studies have shown the advantages of high field strength for fMRI applications (16-26). Proton MR Spectroscopy (MRS) is used for characterization of cerebral tumors and for monitoring treatment of epilepsy, infection, stroke, multiple sclerosis, trauma, metabolic disorders and degenerative processes such as Alzheimer's and Parkinson's diseases (27). Improved resolution between metabolite peaks, which translates to greater chemical shift, therefore allows for greater accuracy in identification and quantification of each metabolite. MR microscopy is used to image at sub-millimeter resolutions. All these applications require simultaneous spatial and temporal resolution. Clinical imaging applications benefit from higher spatial and temporal resolution due to high quality images with fewer motion

artifacts due to shorter breath-hold time, resulting in improved patient comfort and throughput. It is therefore evident high magnetic field strength offers very significant advantages to MR applications due to the SNR advantage and consequent improvement in spatial, spectral and temporal resolution.

The main drawback of high field imaging is the inhomogeneity in B_1 field which is known to be caused by sample electric properties (6,12,28-36). The formation of a characteristic bright central region surrounded by dark bands in the image of a high dielectric phantom is due to the dielectric properties of the sample (29,35). Tissues in the human body generally have relative permittivity ranging between 50 and 80 at 128MHz (28). This results in a reduction of wavelength by a factor of 7 to 9 as compared to free space. At the 3T imaging frequency of 128MHz, the wavelength of the B_1 field inside the body ranges between 26cm and 34cm. These wavelengths are comparable to the dimensions of the human body and hence result in phase shifts inside the body. These result in the formation of interference patterns inside the body. In addition, the human body is approximately cylindrical in shape and behaves as a lens, thereby focusing B_1 field towards the center. At frequencies higher than 128MHz, this effect is only compounded further.

Sample conductivity, on the other hand, causes the B_1 fields to attenuate inside the sample. Conductivity also results in the formation of local current vortices or eddy currents. For linearly polarized fields, eddy currents create characteristic dark spots known as quadrupole artifacts (10). At field strength of 1.5T, the quadrupole artifacts can be eliminated by circularly polarized B_1 fields.

Another effect of sample conductivity is the creation of additional parasitic capacitances between the load and the RF coil. At field strengths of 1.5T and below, the component capacitor values used to resonate the RF coil are very large compared to the parasitic capacitance. However, at field strengths greater than 1.5T, the parasitic capacitors are of the same order of magnitude as the component capacitors. Therefore, asymmetric placement of the sample would lead to unequal frequency shifts in the resonant loops of the RF coil, leading to formation of shading artifacts.

In summary, while high field MRI offers increased spatial, spectral and temporal resolution due to increased SNR, B_1 field inhomogeneity is a major drawback. B_1 field inhomogeneity occurs due to the electric properties of the sample such as the sample dielectric constant and conductivity and resulting interactions between the sample and RF coil. While sample properties cannot be altered, however, good and innovative RF coil design may help in optimizing the B_1 field homogeneity. The following section lists the work done so far in addressing the issue of B_1 field inhomogeneity at high B_0 field strengths.

II.3. RF volume coils

A perfectly homogeneous B_1 field can be created inside an infinitely long cylinder by a surface current I_z such that

$$\vec{I}_z(\varphi) = \hat{z}.I_0 \sin(\varphi) \qquad \text{[II.6]}$$

where $\hat{z}$ is a unit vector along the cylinder axis and φ is the azimuthal angle (37). RF volume coils approximate the continuous current distribution of equation [II.6] with appropriately placed discrete conductors on a cylindrical surface of finite length.

Saddle coils consist of two rectangular loops that are placed diametrically opposite to each other on the surface of a cylinder as shown in Fig. 1. The width of the rectangular loops is chosen such that the axially directed conductors subtend an angle of 120^o at the center of the cylinder. This has been shown to generate a B1 field of optimal homogeneity for four conductors (38). Such a placement of the conductors approximates the sinusoidal current distribution of equation [II.6] at six points on the circumference of the cylinder.

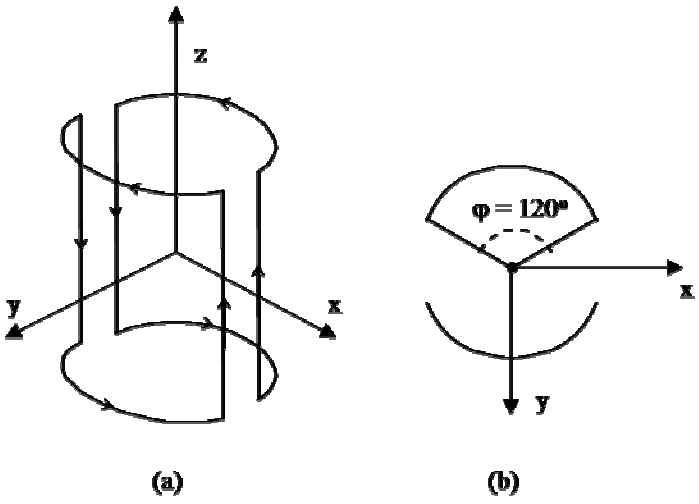

FIG. 1. Schematic of a saddle coil. Figure shows direction of current flow (a) and showing axial conductor placement (b). Uniform field is generated in the y direction.

The slotted tube resonator, proposed by Schneider and Dullenkopf (39), is a shielded conducting cylinder into which are cut two rectangular windows diametrically opposite to each other. The remaining conducting strips subtend an angle of 80^o at the center. When driven in parallel, they generate a uniform B_1 field. The slotted tube

resonator uses transmission line elements to resonate at the desired frequency and has been used for high field NMR spectroscopy. The Alderman-Grant resonator (40) is a modification of the slotted tube resonator with a guard ring, to shield the sample from E fields and improve the B_1 field homogeneity. The angle subtended by the conductor remains the same as in the slotted tube resonator. A further modification of the Alderman-Grant generator, due to Kost *et al*, is to increase the subtended angle to 90^o in order to improve the B_1 homogeneity in the absence of a shield. However, these are small coils that are mainly used for spectroscopy where the sample dimensions are in the order of millimeters. The coils need to be much bigger, with much larger homogeneous volume for human imaging and consequently, there is degradation in homogeneity due to the tendency of RF current to concentrate at the edges of the conductor. The Litz design proposed by Doty *et al* (41), is a further modification of Alderman-Grant resonator, with the Kost window optimization. Conductors are placed in the form of a litz wire in order to overcome the effects of current crowding, thereby improving B1 homogeneity.

Hayes *et al* (2) proposed, what has become, the most popular volume coil in use today. The birdcage coil, whose structure is essentially a ladder network closed on itself, supports a sinusoidally distributed standing wave pattern on its rungs. These coils generate highly homogeneous B_1 fields in large imaging volumes up to B_0 field strengths of 1.5T to 2T. Birdcage coils can be designed as low-pass, high-pass or band-pass coils, depending on the position of the tuning capacitors, as shown in Fig. 2.

The Transverse ElectroMagnetic (TEM) resonator, first proposed by Roschmann (4) and developed further by and Vaughan *et al* (5), works on the principle that coaxial cavities support propagation of TEM waves in the axial (z) direction. The TEM resonator is a resonant, re-entrant coaxial cavity which supports sinusoidally distributed standing current waves. These result in the generation of a TEM pattern in the coaxial cavity, which is stationary in the z direction. Concentration of the E fields in the space between the coaxial conductors results in the formation of uniform B_1 field in the cavity. The use of distributed capacitors as the tuning elements ensures reliable operation at high field strengths.

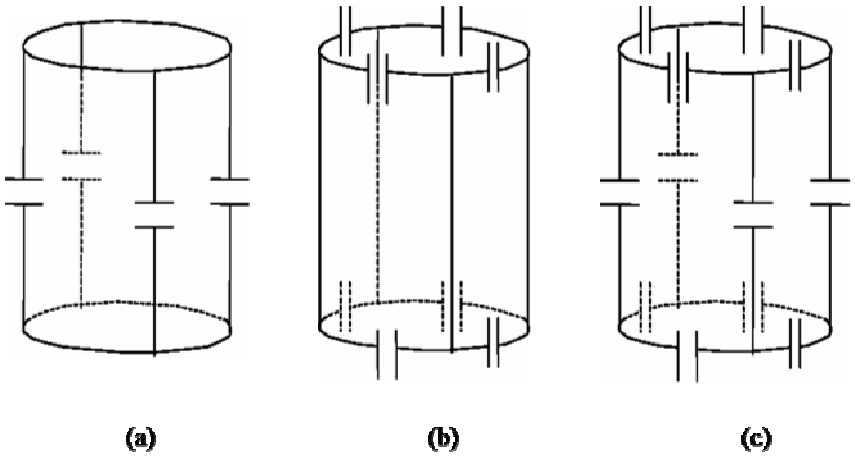

FIG. 2. Schematics of four rung birdcage coils. Low pass (a), High pass (b) and Band pass (c) birdcage coil configuration.

Birdcage and TEM coils can be driven at two points that are 90^o with respect to each other in space and time. Two-port quadrature drive results in the generation of

circularly polarized B_1 field. This reduces the transmit power requirement by a factor of 2 and increases SNR by a factor of $\sqrt{2}$.

The main problem of high field imaging is B_1 field inhomogeneity. The cause can be attributed broadly to two phenomena. These are interaction of rf with the sample and the interaction of the sample with the coils structure.

II.4. Brief overview of transmit array design

In this dissertation, a volume transmit array system has been built to overcome the B_1 homogeneity problems at high fields. The system consists of three major components. These are the controller module, the RF current element and the volume coil which consists of eight current elements placed at equal azimuthal angles apart on the surface of a cylindrical former.

CHAPTER III

MULTIPLE CHANNEL CONTROLLER MODULE

III.1. Introduction

The RF front end of a typical phase array antenna system consists of the RF amplifier, phase shifters and attenuators. The phase shifters and attenuators are used to control the beam pattern and directivity by varying the amplitude and phase of the currents on the antenna elements. In antenna literature, these are referred to as beam formers (42,43). Digitally (44-46) and optically (47,48) controlled beam formers have been implemented by other researchers with sophisticated feedback control loops to enable various tracking applications using phased array antennas.

In this chapter, an 8 channel DC voltage controlled phase shifter/ attenuator module or controller module, for short, is designed and implemented as part of the 8 channel phased array transmit coil system. The transmit coil system is designed to create controllable transverse magnetic field patterns in the imaging volume, in high field MRI applications. The desired field patterns can be generated by controlling the amplitude and phase of the currents in the rungs of the transmit coil. That control is implemented by the controller module by setting the DC control voltages to the attenuators and phase shifters. A block diagram of the controller module is shown in Fig. 3.

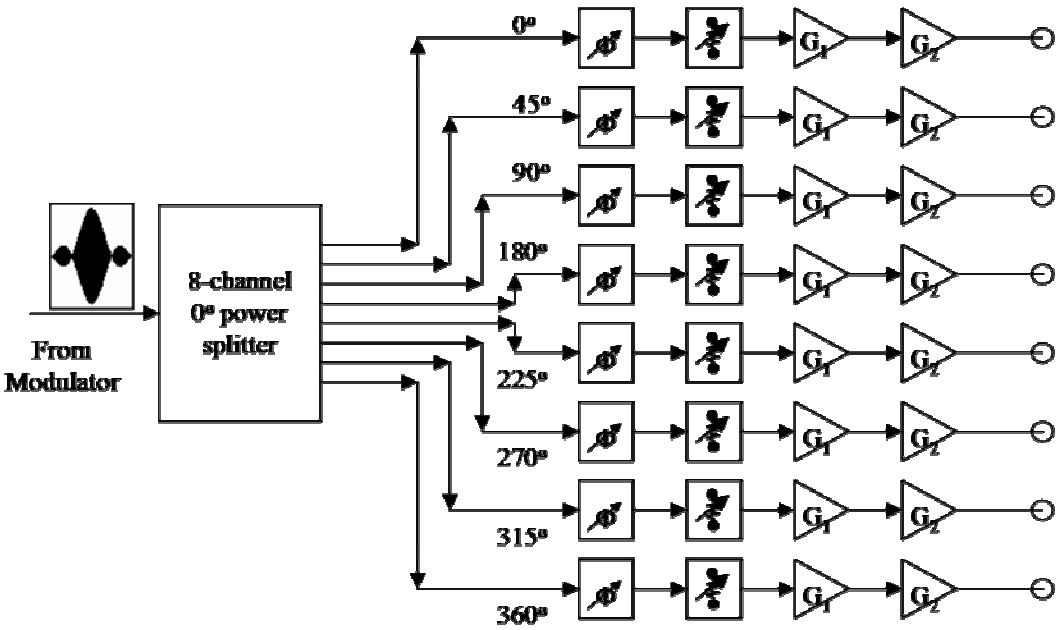

FIG. 3. Block diagram of the eight channel controller module. The single RF input is split into eight channels. A fixed phased shift of 45^{o} between adjacent channels is applied using coaxial cables. A voltage controlled attenuator and phase shifter in each channel controls the amplitude and phase of the output voltage. Each channel contains a two stage driver amplifier to provide adequate voltage drive to the current sources.

III.2. Design specification

The design specifications of the controller module are as follows:

- Number of channels : 8
- Maximum output power from each channel : 27dBm (minimum)
- Independent manual control of attenuator and phase shifter

The 8 channel phased array controller module consists of three distinct sets of paths: the RF path, the DC bias voltage path and the DC control path. The RF path consists of a single RF input into an 8-way, 0^o power splitter. The eight outputs of the splitter are fed into the eight input ports of an 8-channel voltage controlled attenuator and phase shifter and driver amplifier module through coaxial cables that are designed to provide fixed 45^o phase shifts with respect to each other. The output ports of the 8-channel module are the output ports of the system.

The DC bias path provides bias voltages for the small signal driver amplifiers and the power amplifier output stages of all eight channels. The DC control voltage path connects a DC voltage supply across two sets of eight variable voltage dividers. The two sets of eight voltage dividers provide the control voltages to the voltage controlled attenuators and phase shifters.

III.3. Materials

The components used in the design of the controller module were actually self contained modules with well defined functionality. The modules were chosen keeping in mind the output power specification for the controller module and then working

backwards. The maximum input and output power ratings and the insertion loss of each module were taken into account when selecting the modules.

The ZFSC-8-1 (Minicircuits, New York) was used as the 8-way, 0^o power splitter. The ZFSC-8-1 is specified to operate in the 0.5MHz to 175MHz frequency range with 25dB of isolation, 5^o phase imbalance and 0.5dB amplitude imbalance between channels and 1dB insertion loss.

The voltage variable phase shifter used was the JSPHS-150 (Minicircuits, New York). The JSPHS-150 is a surface mount device that comes in a hermetically sealed package. It is specified to operate in the 100MHz to 150 MHz frequency range with a typical insertion loss of 1.2dB. It is specified to provide 180^o of linear phase shift over a control voltage range of 0-12V.

The voltage variable attenuator used was the RVA2500 (Minicircuits, New York). The RVA2500 is specified to operate over a frequency range of 10-2500MHz. The other useful design specifications are insertion loss of -3dB, maximum attenuation of -55dB at control voltage of 0 volts and return loss of -20dB. The RVA2500 requires a DC supply voltage of +3 to +5V with maximum supply current of 5mA. It is specified to operate over a control voltage range of 0-17V with a maximum control current of 30mA.

The ERA-5SM was used as the first stage driver amplifier. The ERA-5SM is a small signal drop-in amplifier that is designed to be used in a 50Ω system. It is specified to operate over the DC-4GHz frequency range, providing typical gain of 20dB, with 18dBm maximum power output. The maximum no damage input power is specified at

13dBm. It is designed to operate at a DC supply voltage of 4.2V and supply current of 65mA.

The HELA-10D was used as the final amplification stage of the controller module. The HELA-10D is specified to operate in the 8-300MHz frequency range, providing a gain of 11dB. The output power at the 1dB compression point is specified at 30dBm with maximum no damage input power of 20dBm. The HELA-10D is rated for a DC supply voltage of 12V and supply current of 525mA.

The HELA-10D is designed as a push-pull amplifier. It is supplied as a kit with two ADT1.5-1 transformers, which were used simultaneously as impedance transformers and power combiners. The ADT1.5-1is specified to operate in the frequency range of 0.5-650MHz, with impedance transformation ratio of 1.5 and insertion loss of about 1dB.

III.4. Construction

Once the components to be used in the controller module were chosen, construction began with the PCB layout using a computer program (Protel). The circuit schematic of a single channel, used to create the layout, is shown in Fig. 4. Four such channels were laid out on two boards named A and B for convenience. The footprints of all the components, as recommended by the component data sheets, were first created. The trace carrying RF power was designed as a microstrip line such that the characteristic impedance of the line was 50Ω. The PC board layout was milled out on a ½ ounce, double sided copper board using a computer controlled milling machine (LPKF Protomat C30).

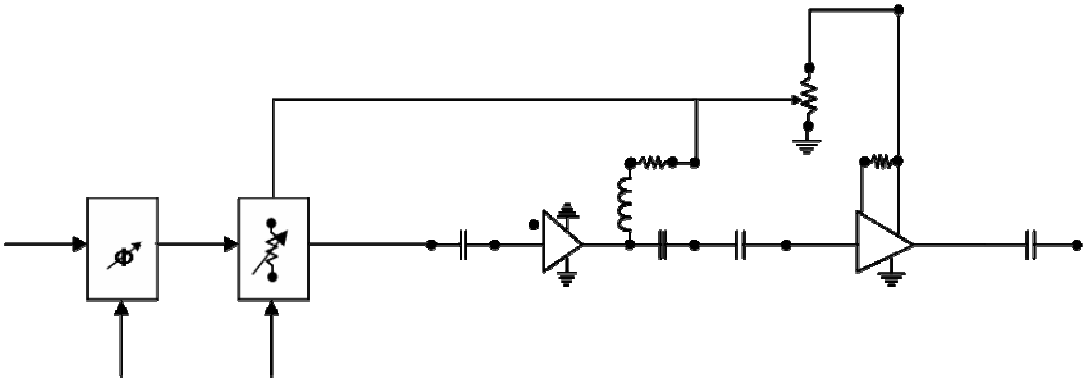

FIG. 4. Schematic of a single channel phase shifter and attenuator. The controller module consists of eight of these built into two 4-channel submodules.

The boards were populated with the components on their respective footprints. PC mount straight SMA connectors were soldered to the ends of the RF traces. Via holes were places at regular intervals. The top and bottom ground planes were then shorted through the via holes using 20 AWG tinned copper wire. This completed the RF circuit.

A single supply voltage input was used for all the DC voltage needs. Since the HELA-10D operated on a 12V supply and the ERA5SM and RVA2500 operated on 4.5V, a voltage divider was implemented on board A. For the ERA-5SM, the supply line was connected to the bias pin via a current limiting resistor to limit the bias current, as shown in Fig. 4. The control voltage lines, like the supply voltage lines, were implemented using semi-rigid coaxial cables. This was done in order to minimize coupling with the RF line, thereby eliminating the necessity for RF chokes. Fig. 5 shows a picture of the board populated with the components and the control and supply lines.

The two 4 channel boards were then mounted in an aluminium box using spacers. Before the boards were mounted, cutouts were made in the aluminium box to

accommodate the RF connectors and the 25 pin D-sub connector. A finned aluminium heat sink was mounted on the bottom side of the box. Two solid copper bars, ¾ inch wide and ¼ inch thick, were stacked inside the box, such that upon mounting the boards using ½ inch spacers, the HELA-10D amplifiers would sit smugly on the copper bars. This acted as a good heat transfer mechanism.

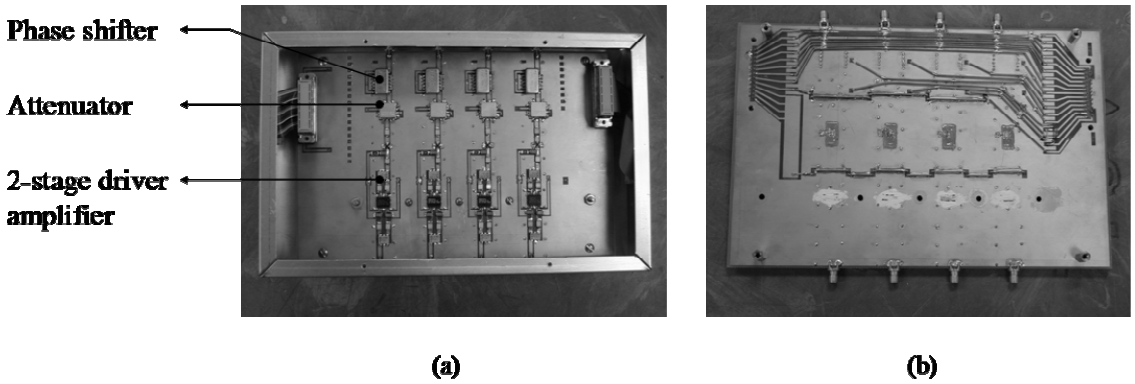

FIG. 5. Picture of the 4 channel attenuator/phase shifter module. (a) shows the phase shifter, attenuator and two stages of amplification. (b) shows the routing of the control lines and supply voltage lines.

The two 4 channel modules, A and B, were then stacked on top of each other such that A was the upper module, and fastened to the base plate of an aluminium chassis. The potentiometers providing the variable control voltage were mounted on the front plate. The ZSFC-8-1 power splitter was mounted on a side plate towards the rear of the chassis. On the back plate of the chassis were mounted the RF input BNC jack, the DC supply terminals and a cooling fan.

The variable voltages were provided by two banks of 8 potentiometers each, which were mounted on the front plate of an aluminium chassis. The potentiometers in each bank were connected in parallel to each other. One bank of potentiometers (A) provided the attenuator control voltages while the other bank (P), provided the phase shifter control voltages. A single DC voltage supply, set to 18V, was used as the control voltage supply. However, since the phase shifters used a control voltage range of 0-12V, a voltage divider was implemented such that a 12V supply was provided to the potentiometer bank, P.

DC supply and control voltages were transferred between the modules A and B through the 25 D-sub connectors. The supply voltage from the back panel of the chassis was connected to the supply voltage terminals on module A. The control voltages from the potentiometer banks A and P, were brought to the control boards via a 25 conductor ribbon cable, which was connected to module A through a 25 pin D-sub connector.

All RF connections between modules were made using RG316 coaxial cables with either BNC or SMA connectors. The channel numbers were marked out on modules A and B. The RF input jack was connected to the input of the power splitter. Eight coaxial cables of increasing length were used to connect the power splitter outputs to the inputs of the attenuator/phase shifter channels such that fixed phase shifts of 45^{o} at a frequency of 127.74MHz were implemented between adjacent channels. The outputs of the two modules were then connected to the BNC jacks mounted on the front panel of the chassis.

III.5. Characterization of controller module

The controller module built was tested for the following parameters:

- Maximum output power
- Linear range of attenuation
- Linear range of phase shift

All measurements were made in a RF screen room at an ambient temperature of about 25^{o}C. The controller module was allowed to operate at full input power for a period of 15 minutes before the measurements were recorded in order to allow it to reach thermal equilibrium. Output measurements were made for one channel at a time with all other channel outputs terminated in 50Ω and control voltages set at arbitrary levels.

III.5.1. Attenuation and maximum power

The test setup used to characterize the controller module for maximum power and linear range of attenuation consisted of the HP8712ES network analyzer which was used as the RF source. Taking into account the insertion losses of all the modules, the input power required to provide the design output power, was calculated to be 11dBm. The output power level of the network analyzer was set to 11dBm and the center frequency and sweep bandwidth were set to 127.74MHz and 0Hz respectively. The attenuator control voltage was varied over the full range of the potentiometer in steps of 1 volt. A multimeter was used to measure the amplitude of the control voltage.

The controller module channel output under test was connected to a spectrum analyzer which measured the output power of the channel. Using a T connector, the channel output was also connected to the input port of an oscilloscope through a λ/2

coaxial cable in order to measure the output voltage amplitude. The impedance of the termination at one end of the λ/2 cable is transformed to the same value at the other end. The input impedance of the oscilloscope measurement port was therefore set to 1MΩ so that there was negligible transfer of power to the oscilloscope.

Fig. 6 shows the plots of the output power measurements against the control voltage. The plots show linear variation of output power for control voltage amplitude in the range of 5-17V. The maximum output power is found to be 26.6dBm for all channels. When the input power to the controller module was increased by 3dB, the maximum output power of all channels was found to be 30.4dB. Further increase in input power did not result in any increase in the output power. The increase in insertion loss of the controller module from the calculated value could be attributed to line losses.

Fig. 7 shows the plots of the linear range of the output voltage measurements against the control voltage. This measurement is presented here because it is a more useful result than the output power for the operation of the RF current source described in the next chapter.

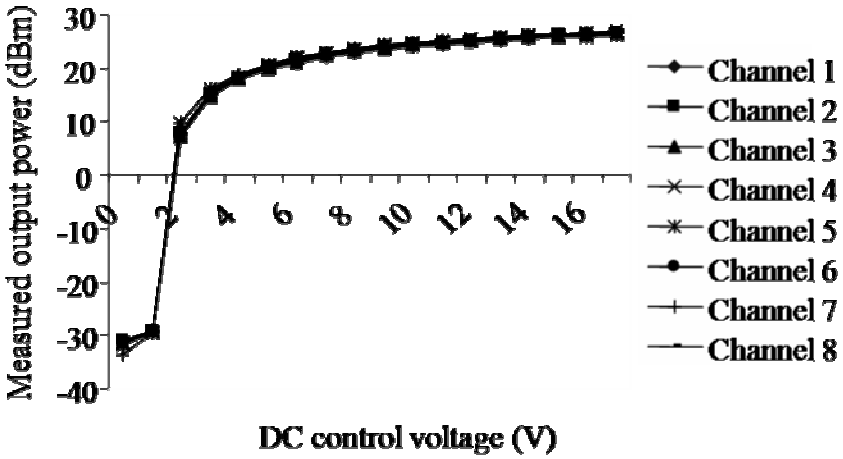

FIG. 6. 8 channel output power vs. DC control voltage. The range of DC control voltages over which the output power is linear is 5V to 17V. The maximum output power is 26.6 dBm.

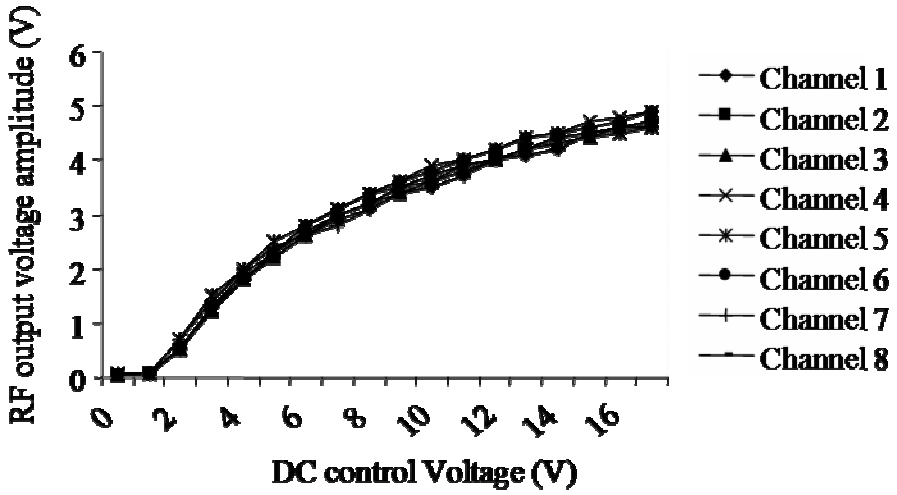

FIG. 7. 8 channel output voltage amplitudes vs. DC control voltage.

Fig. 8 is a plot of the output voltage of all the channels for a given control voltage setting of 8V. This plot shows a maximum variation of 0.2V. This is a small variation on the output voltage amplitude. As all channels other than the channel under test were set at random control voltages for both the attenuators, this result implies good isolation between channels.

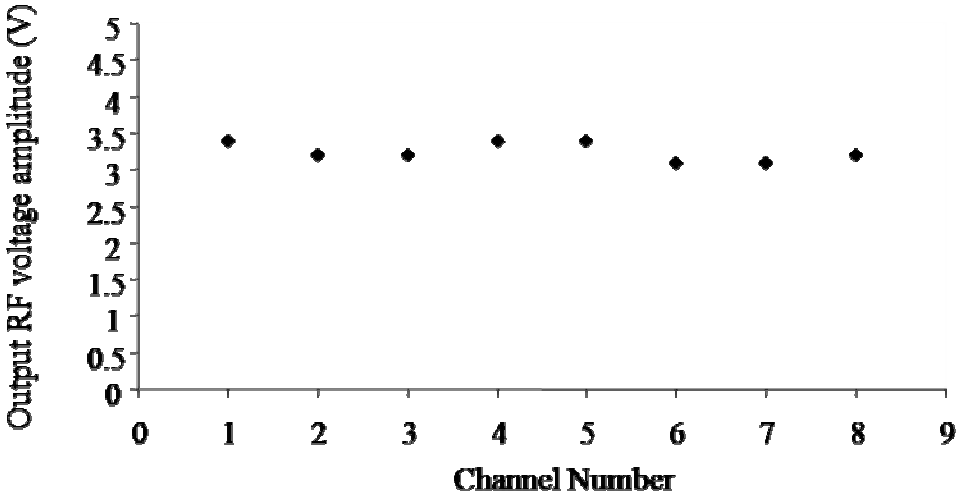

FIG. 8. Output RF voltage vs. channel number. The control voltage was set to 8V. The average voltage is 3.25 volts with a maximum deviation of under 10 percent.

III.5.2. Phase characterization

The network analyzer was used to make S21 measurements in order to characterize the controller module for phase behavior. The network analyzer was subjected to a through calibration such that the measured phase shift was that measured over the entire RF path of the controller module channel under test. Phase measurements

were made with the controller module operating under full power and phase shifts of channels other than that under test, set randomly.

Fig. 9 shows the plots of channel phase shifts with control voltage. The linear range of control voltages appears to be between 5V and 10V. The phase of the RF signal is shifted through approximately 180^{o} over this range. The phase difference of approximately 45^{o} between channels is due to the fixed phase shifts introduced by the coaxial cables. The anomalies found in the measurements of channel 4 may be attributed to a faulty phase shifter module. The anomaly does not appear to be due to interference from other channels because the same measurements were obtained even upon randomly changing the phase shifts on other channels.

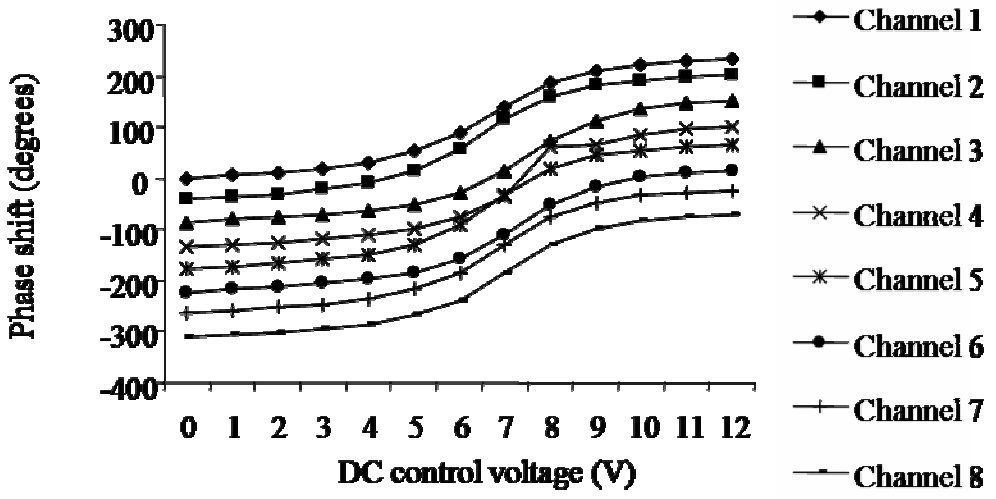

FIG. 9. Phase variation with control voltage. The anomaly in channel 4 may be because of a faulty phase shifter.

The output voltage amplitude and phase characteristics shown above may be used as look-up tables in order to set the proper DC voltages to obtain the desired RF voltage amplitude and phase using computer control.

III.6. Summary

In summary, a controller module has been implemented to control the amplitude and phase of the RF control voltage that is applied to the voltage controlled current source, described in the next chapter. The controller module has been characterized for the range of control voltages over which the amplitude and phase of the output voltage vary linearly with the control voltage settings.

CHAPTER IV

RF CURRENT SOURCE

IV.1. Introduction

Phased array antennas have been used extensively in telecommunication applications for several decades, starting with the short wave radio in the early twentieth century (43).The classical phased array antenna system consists of the antenna array and the associated feed network, also called the RF front end. The RF front end consists of attenuators, phase shifters, T/R switch and Low Noise Amplifiers on the receive path and power amplifiers on the transmit path (42).

More recently, with the ascent of wireless communication, research in phased array antenna technology has been directed towards the development of miniature planar antenna systems that are integrated with the RF front end (49-52). Such antenna systems are called Active Integrated Arrays (AIA). The antenna elements in such AIA form the output tuning elements of the active devices (53).

Phased array antennas have the ability to form directive far field radiation patterns as a cumulative effect of the main beams of individual array elements. This is achieved by specifying a relative current distribution at the array inputs. The patterns formed could also be steered in the desired direction by adjusting the phases of the currents on the array elements (43,54,55), thereby eliminating the necessity for expensive control equipment to physically turn the antenna in the desired direction. This

would necessitate accurate control of current amplitudes and phases on the antenna elements.

The RF power amplifiers are important components of the RF front end of a phased array antenna. The RF power amplifiers feed power into the array elements through matching networks. The matching networks ensure maximum power transfer between the RF amplifiers and the phased array transmitter. Since the matching networks are designed for specific impedance transformation ratios, the RF power amplifiers can be modeled as voltage sources connected across the array elements. The current on the array element is then determined by the impedance presented to the matching network in addition to the applied voltage. This is known as a free excitation scheme. In the presence of other array elements in the vicinity, the impedance presented to the matching network is a function of the current amplitude and phase on each of those elements (43,54). This is due to the unavoidable electromagnetic phenomenon of mutual impedance. Therefore, in order to be able to exercise accurate control over the amplitudes and phases of currents on each array element, it is essential to have an accurate knowledge of the mutual impedances.

In the context of MRI, the interest is in generation of uniform, near magnetic field, the B_1 field. This is, of course, generated by currents on the antenna elements. It would therefore be desirable to accurately control the current amplitude and phase on the rungs of the transmit coil. The transmit coils are designed as resonant structures that are excited by an RF amplifier which can be modeled as a voltage source. Through Finite Difference Time Domain (FDTD) simulations (33,56), it has been shown that the

optimal field homogeneity may be achieved through multi-port excitation of a RF coil with independent control of excitation amplitude and phase. However, with the currently used free excitation scheme, it would be essential to accurately know the mutual impedances between the strongly coupled loops of the transmit coil in the presence of the load in order to accurately set up the currents required to create the desired B_1 field. This would be a very tedious process and very sensitive to load position and composition. A simple way to implement multi-port excitation would then be to use forced current excitation such that each array element would be driven by an RF current source at the Larmour frequency.

In this chapter, the implementation of such a forced excitation scheme is discussed. A voltage controlled RF current source integrated with an array element or rung is implemented utilizing the concepts of MOSFET based power amplifier design and Active Integrated Antennas. The conditions under which the MOSFET behaves as a true voltage controlled RF current source are experimentally verified. The ability to independently control the rung current amplitude and phase by varying the control voltage amplitude and phase is demonstrated. The resonant behavior of the rung is studied.

IV.2. Theory

IV.2.1. Classical amplifier design

Fig. 10 shows the block diagram of a classical MOSFET based power amplifier design. The MOSFET is a three terminal voltage controlled active device. The steps involved in the fabrication of the MOSFET are described in appendix A. A detailed

explanation of the principle of operation of a MOSFET based Class A power amplifier is given in appendix B, along with a description of other classes of linear amplifiers.

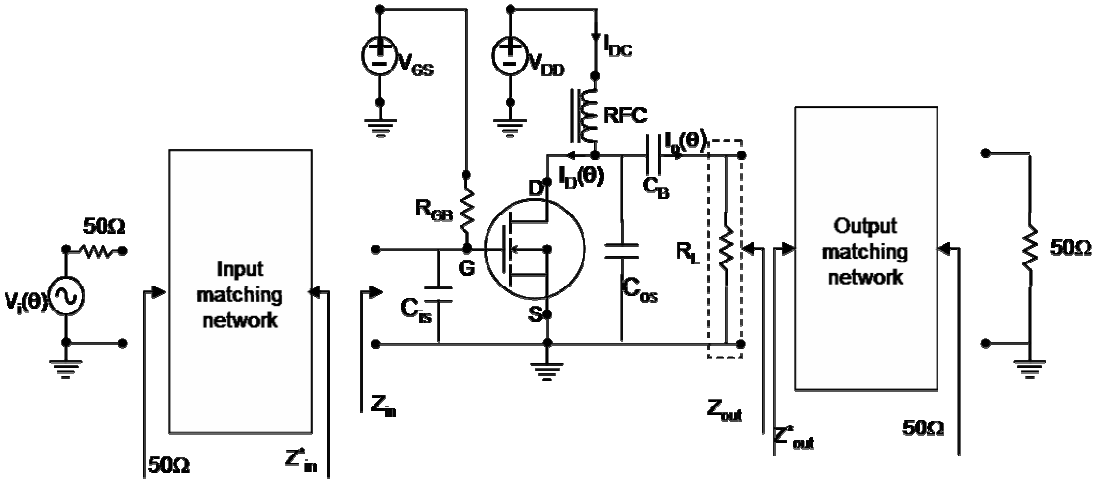

FIG. 10. Design of a conventional MOSFET power amplifier. The drain voltage supply is used to set the MOSFET in the saturation region. The gate voltage sets the operating point of the MOSFET. The output and input matching networks provide conjugate match for maximum power transfer. C_B is the DC blocking capacitor which is a short for RF.

The steps involved in the design of the above power amplifier are well documented (57-61) and are summarized below:

- The MOSFET is placed in the saturation region of its characteristic by providing an appropriate DC supply voltage at the drain terminal via the RF choke.
- The operating point or the quiescent current of the MOSFET is set by providing the appropriate DC supply voltage at the gate terminal. This determines the linear class of operation of the RF power amplifier.

- Since the internal resistance of the MOSFET is very high, the output impedance of the MOSFET is given by the output capacitor, C_{os}. The optimum load of the MOSFET is calculated as (explanation in appendix B)

$$R_L = \frac{\left(V_{DD} - V_{DSat}\right)^2}{2P_0} \qquad \text{[IV.1]}$$

The output impedance is then given by

$$Z_{out} = R_L - jX_{C_{os}} \qquad \text{[IV.2]}$$

where $X_{C_{os}}$ is the capacitive reactance due to C_{os} and R_L is the **virtual** load resistance.

- For maximum power transfer to a standard 50 ohm load, such as a coaxial cable, the output matching network (62) is implemented. The output matching network conjugate matches the output impedance of the MOSFET given by [IV.2] to the 50 ohm load as shown in Fig. 10. The impedance looking into the matching network is given by

$$Z_{om} = Z_{out}^* = R_L + jX_{C_{os}} \qquad \text{[IV.3]}$$

- The input matching network is then implemented to conjugate match the 50 ohm source impedance to the input impedance of the MOSFET as shown in Fig. 10, where

$$Z_{im} = Z_{in}^* = R_{in} + jX_{C_{is}} \qquad \text{[IV.4]}$$

where R_{in} is the input resistance of the MOSFET due to the gate contact.

Therefore, a key feature of the MOSFET RF amplifier is that the MOSFET is used to drive current through a high resistance load. This creates a voltage drop across the load. R_L is a virtual load presented to the MOSFET by the output matching network. The MOSFET therefore drives current through the components of the output matching network. Therefore, amplified power is transferred to standard load or next amplification stage through the output matching network.

IV.2.2. RF current source

Fig. 11 shows the circuit schematic of the MOSFET RF voltage controlled RF current source. The RF current source design is a modified version of the classical RF power amplifier, where the virtual load resistance, R_L, of Fig. 10 has been replaced by the array element (rung), represented by a series LCR network. The MOSFET is shown as a voltage controlled current source, integrated with the rung. The lumped element inductor and resistor represent the distributed inductance and series resistance of the rung. The variable capacitor is used to tune the rung to series resonance. This circuit design therefore uses the MOSFET to drive RF current through the low resistance rung.

In the absence of an output matching network, there is no mechanism to compensate for C_{os}. Hence, C_{os} appears as a shunt reactance across the rung and serves to divert current from the rung as the magnitude of rung impedance approaches $X_{C_{os}}$. This makes it necessary for the rung impedance to be as small as possible, compared to $X_{C_{os}}$.

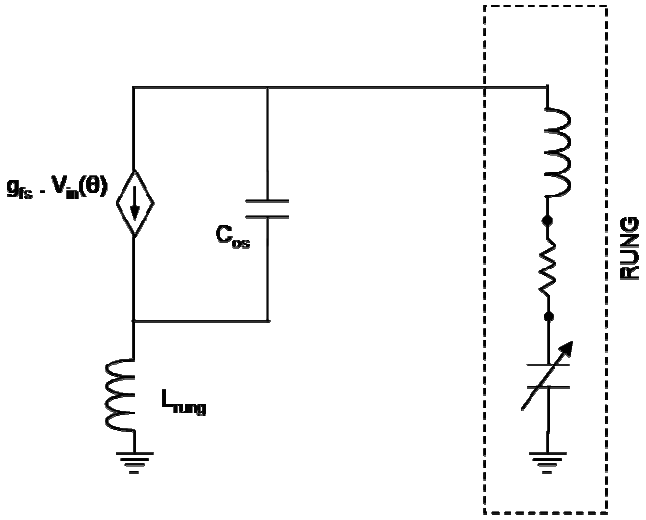

FIG. 11. Current source driving current through the rung. In the above schematic, the MOSFET is represented by a voltage controlled current source. C_{os} includes the output capacitance, and the total capacitance in the feedback path. L_{lead} represents the package lead inductance. The rung is represented by a series LRC network. The variable capacitor is used to set the impedance of the rung.

The key requirements of the RF current source are that the rung current amplitude and phase vary linearly as the input voltage amplitude and phase respectively. This would enable predictable and simple control of rung currents over the entire range of the current handling capacity of the MOSFET. Another requirement is that the current amplitude and phase are independent of each other. This would ensure linearity in response of the RF current source to the input voltage stimulus. The following sections test the RF current source for the above specifications.

IV.3. Materials

IV.3.1. The RF power MOSFET

The BLF245 is an N-channel, enhancement mode RF power MOSFET, manufactured by Philips Semiconductors, ADDRESS. Table 1 lists the important design parameters of the BLF245, extracted from the datasheet. The BLF 245, which is fabricated on a silicon die, comes enclosed in an SOT 123A plastic package.

Table 1

Symbols and definitions. List of important BLF245 MOSFET (Philips Semiconductors) datasheet parameters used in the design of the RF current source.

Symbol	Parameter	Conditions	Typ.	Unit
C_{is}	Input capacitance	V_{GS}=0, V_{DS}=28V, f=1MHz	125	pF
C_{os}	Output capacitance	V_{GS}=0, V_{DS}=28V, f=1MHz	75	pF
C_{rs}	Feedback capacitance	V_{GS}=0, V_{DS}=28V, f=1MHz	7	pF
V_T	Threshold voltage	I_D=10mA, V_{DS}=10V	3.2	V
g_{fs}	Forward transconductance	I_D=1.5A, V_{DS}=10V	1.9	

The SOT 123A is a four terminal package with a flange as shown in Fig. 12. The source metallization on the MOSFET die are wire bonded to the package source terminals. The package source terminals are shorted in order to provide a robust ground to the MOSFET. The drain and gate metallizations on the MOSFET die are similarly

wire bonded to the drain and gate package terminals, respectively. The MOSFET die is mounted on the flange, which is electrically insulated from the source terminals. The flange is used to conduct heat away from the MOSFET die and into the heat sink.

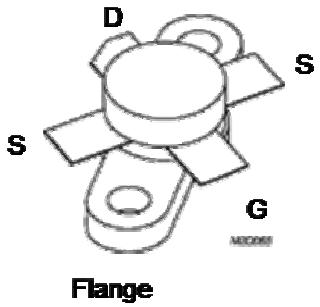

FIG. 12. A schematic of the SOT123A plastic package. Figure shows the Drain (D), Gate (G) and Source (S) terminals. Also shown is the flange which is electrically insulated from the terminals and serves to conduct heat away from the MOSFET and into the heat sink.

IV.3.2. The printed circuit board

The PCB layout that was used to implement the RF current source schematic is shown in Fig. 13. The board layout was made using a freeware version of Protel which was released in 1994 and allows a maximum of twenty five components to be placed on the layout. A two sided copper board of dimensions with G-10 dielectric was then milled using a computer controlled milling machine (Protomat C30, LPKF corporation).

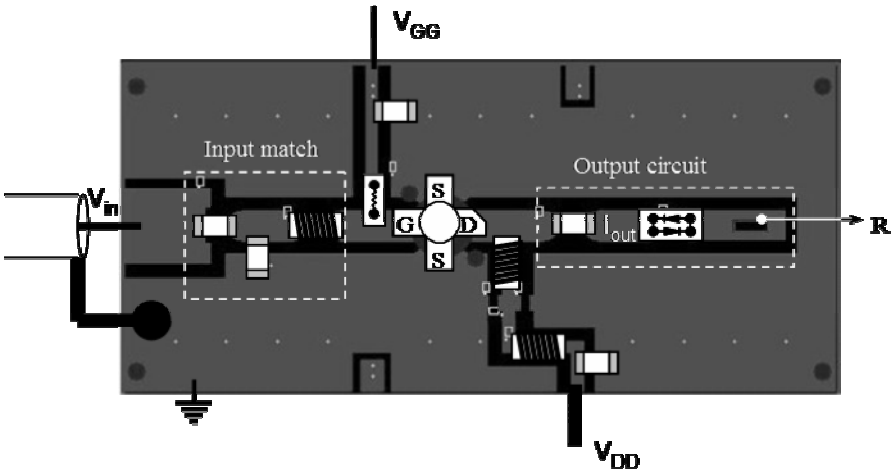

FIG. 13. Layout of the MOSFET based RF current source. The input matching network and part of the output circuit are marked out. R is the hole through which the rung enters the coil cavity.

It can be seen in Fig. 13 above, that the majority of the board area is taken up by the ground plane The RF and DC conductive paths make up a very small percentage of the total board area. This is good design practice that properly defines a ground plane by minimizing inductance between any two points on it. A similarly dimensioned PCB was used as a base plate to lend structural strength to the main PCB. 20 AWG bare copper wires were then inserted into the corresponding via holes on the top and bottom PCB's and soldered to the copper so as to create a continuous and well defined ground plane. The via holes were placed at ½ inch intervals to ensure good continuity between the top and bottom ground planes.

As shown in Fig. 13, the layout has traces for the input RF voltage, output RF current and DC bias voltages. These traces were designed as microstrip lines with an

extensive ground plane on the bottom side of the PCB. The points where the continuity of the traces is broken correspond to the points where the components of the matching network were mounted. The output trace was also broken where the DC blocking capacitor and one of the rung capacitors was mounted. The rectangular hole that is visible in the output trace is where the rung broke through the RF shield and entered the coil cavity.

IV.3.3. Mounting the BLF245

The BLF245 was inserted from the bottom of the reinforced board through the hole made for it. It was then positioned with the drain terminal facing the rectangular hole in the RF trace. The flange was then positioned between the top PCB and the heat sink, described in section (IV.3.7). The corresponding holes on the PCB, flange and the heat sink were aligned and fastened firmly together with non-magnetic machine screws. Before placing the heat sink under the flange, thermal compound was sparingly applied to the bottom of the flange to maximize contact area between the flange and heat sink. This prevented overheating of the MOSFET by efficiently transferring heat to the heat sink for dissipation to the atmosphere.

The gate and drain leads of the MOSFET were then soldered to the input and output RF traces. The two source leads were soldered to the ground plane on the top of the board. Before the MOSFET was mounted, strips of copper tape were used to connect the top and bottom ground planes through the mounting hole. This was done to properly ground the source terminals of the MOSFET in order to ensure stability during RF operation of the MOSFET into a low resistance load.

IV.3.4. The DC bias voltages

Two Astron DC voltage supplies rated at 13.8 volts and 12 amps output were connected in series, thereby making up a DC power supply unit rated at 27.6 volts and 12 amps as explained in appendix B. This set the MOSFET in the saturation region of its DC characteristic, where it behaves as a voltage controlled current source.

Bench measurements on the RF current source were made in both, the continuous wave mode (CW) and the pulsed mode. For the pulsed mode, a TTL blanking pulse was taken from the blanking output of the system cabinet of the GE Signa 3T scanner at GE Medical Systems. This pulse was inverted using a simple op-amp unity gain inverting circuit. A rectangular pulse of amplitude 3.6 volts at a 10 percent duty cycle was obtained from the inverter and supplied to the MOSFET gate. The timing of the shaped input pulse was synchronized internally with the blanking pulse. Hence, the MOSFET was biased ON only for the duration of the pulse.

For the CW mode, a simple resistive voltage divider was implemented. The gate bias was adjusted to 3.6 volts. The quiescent current, I_{DQ}, was measured to be 2 amps. This made the current source of operating class AB (see appendix B).

IV.3.5. Output circuit

The output circuit of the MOSFET consisted of the array element or rung. One end of the rung was connected to the drain terminal of the MOSFET through the rectangular opening, R, shown in Fig. 13. The rung was broken up into five segments by four chip capacitors, each of 47pF capacitance. This was done to increase the uniformity of current amplitude along the z direction and also to push the self resonance frequency

of the rung higher. The other end of the rung was connected to the RF shield by a trimmer capacitor (Johanson Dielectrics, Sylmar, CA). The range of the trimmer was chosen such that the rung impedance, as measured from the drain terminal of the MOSFET, varied from capacitive to inductive through a series resonance point.

Two air core inductors were implemented by winding 10 turns of a 20 AWG copper magnet wire around a plastic former. The diameter of the inductors was 0.5cm and the inductance of each inductor was measured to be 125nH. Two of these connected in series in the drain supply DC path acted effectively as a high current RF choke. This is shown in Fig. 13.

IV.3.6. Input circuit

The power source for the RF current source was a driver amplifier. This amplifier was designed to operate in a 50 ohm system. Therefore the source impedance for the RF current source was 50 ohms, which had to be matched to the input impedance of the MOSFET for maximum power transfer into the MOSFET and also to prevent reflections back into the cable, which would result in formation of standing waves, leading to cable coupling problems.

The input impedance of the MOSFET, with the series resonant load, was measured to be (2.3-j9.1) ohms. This measurement was made using a network analyzer (Agilent 8712 ES). A long length of 50 ohm coaxial cable connected the network analyzer to the input port of the RF current source. The network analyzer was then calibrated to measure the impedance at the gate terminal of the MOSFET. This procedure ensured that the effects of cable length and trace length were removed from

the impedance measurements. The MOSFET was then reintroduced into the circuit and the input impedance measured. The input impedance is a complex quantity because of the presence of C_{is}. The matching network was then designed to present the complex conjugate of the input impedance of the MOSFET. The matching network therefore compensated for the effect of C_{is} and at the same time, transformed the real part of the input impedance of the MOSFET to the source impedance of 50 ohms.

A three element matching 'tee' network configuration was chosen due to the fact that the Q of the matching network could be controlled by the designer. This would mean that the Q of the matching network could be sufficiently reduced to implement a broader bandwidth of match. A schematic of the matching network is shown in Fig. 14. The Smith Chart option of the network analyzer was used to match the source impedance to the input impedance of the MOSFET. The series inductor set the Q of the matching network. The series and shunt capacitors were then used to match and tune the input impedance of the MOSFET to the 50 ohm source impedance.

IV.3.7. Heat sink design

Integration of the current source with the rung as described in chapter III would require the PCB to be as close to RF shield as possible for two reasons. One is to minimize the length of the rung that is not utilized in the creation of B_1 field. The other reason is to maintain low coil profile when it is placed on the patient table for patient comfort. The chief requirement for heat sink design was therefore a low profile with maximum surface area, allowing free circulation of air.

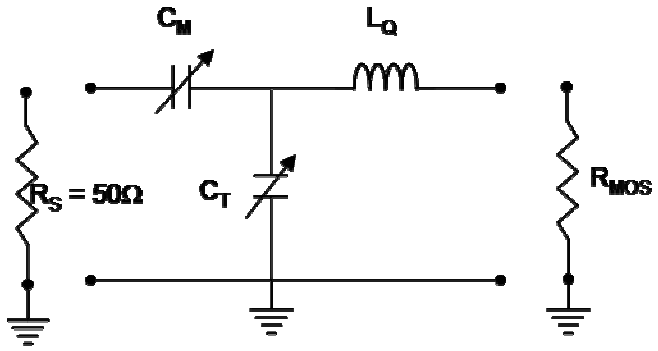

FIG. 14. The three element “Tee” matching network. The matching network conjugate matches the input impedance of the MOSFET to the 50Ω source impedance. L_Q sets the Q of the matching network. C_M and C_T are the match and tune capacitors, respectively. The Q of this matching network is independent of the match and tune capacitors.

A sheet of copper, 0.06 inch thick, was cut into a rectangular piece, 2.5 inches wide and 3 inches long. The copper piece was then rolled using a sheet metal roller so as to produce a curvature along its breadth. The distance between the rollers was adjusted such that the radii of curvature of the copper piece and cylindrical coil former matched. This ensured that the entire surface area of the copper piece made good thermal and electrical contact with the RF shield.

Three rectangular pieces of the same dimensions as the PCB were cut out of a roll of copper gauze. Rectangular holes corresponding to the one on the PCB were cut out to allow passage of the rung. The three pieces were stacked on top of each other and then sandwiched between the MOSFET flange and the copper piece described above. Thermal compound was applied sparingly at the point of contact with the flange to

ensure good thermal conductivity. The gauze pieces acted as fins for dissipation of heat though convection.

IV.4. Methods

A number of experiments were performed in order to understand the behavior of the MOSFET as a voltage controlled current source at RF.

- Experiments were performed to quantitatively determine the constraints imposed by the MOSFET parasitic capacitances and to understand the behavior of the MOSFET under different settings of rung impedance. The rung integrated current source model of Fig. 11 was validated using a simple computer simulation.
- Experiments were performed to determine the linear dependence of rung current amplitude and phase on the amplitude and phase of the input RF voltage.

All measurements were made at a center frequency of 127.74 MHz, corresponding to the Larmour frequency for a static magnetic field magnitude of 3 tesla. The first set of experiments was performed using a continuous wave (CW) sinusoidal signal, derived from a frequency synthesizer, as the input signal. The second set of experiments was performed using a pulsed, amplitude modulated (AM) sinusoidal signal, derived from the system cabinet of the GE Eclipse 3T imaging system. Bench measurements were made at an ambient temperature of about 25^{o}C inside a shielded room. For the CW rung current measurements, the MOSFET was air cooled with the help of a bench fan. This precaution was found to be unnecessary for the AM signal as the maximum duty cycle of 10 percent did not result in overheating of the MOSFET. Under these conditions, the MOSFET was operated at full power for a period of 15

minutes before measurements were recorded. This was done in order to allow the MOSFET to reach thermal equilibrium, thereby improving the accuracy and repeatability of measurements.

In order to determine the constraint imposed by the parasitic output capacitance of the MOSFET on its behavior as a true current source, the rung impedance was measured for various settings of the trimmer capacitor, both with and without the MOSFET in the circuit as shown in the schematics of Fig. 15.

An Agilent 8712ES network analyzer (Agilent) was set in the S-parameter mode with a center frequency of 127.74 MHz and sweep band of 20 MHz. A long RG-58 coaxial cable with BNC connectors was connected at one end to the measurement port of the network analyzer through a bias tee and at the other end, to an open BNC panel mount jack. The bias tee was used to prevent DC voltage at the measurement port of the network analyzer. The network analyzer was calibrated at the terminals of the BNC jack. The terminals of the BNC jack were then soldered to the PCB such that the hot terminal of the BNC jack was connected to the Drain terminal and the ground terminal was connected to the Source terminal of the MOSFET as shown in the layout of Fig. 16. The MOSFET was then removed from the circuit and the rung impedance was recorded for various settings of the trimmer capacitor. The MOSFET was then reintroduced into the circuit and biased with a drain supply voltage of 28 volts and gate supply voltage of 3.6 volts. The rung impedance was again recorded for the same settings of the trimmer capacitor as in the previous measurement.

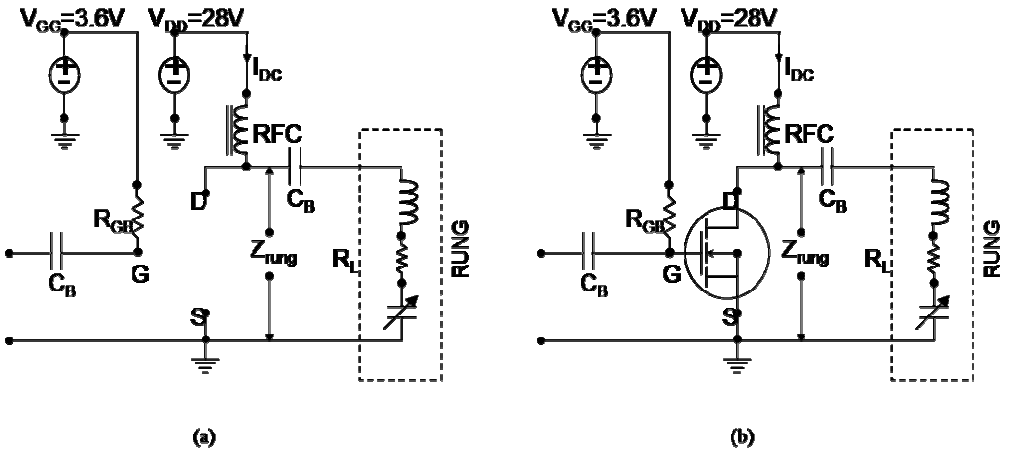

FIG. 15. Schematics showing the measurement of rung impedance. The measurements are made with (a) and without (b) the MOSFET in the circuit. The point of measurement is indicated by Z_{rung}.

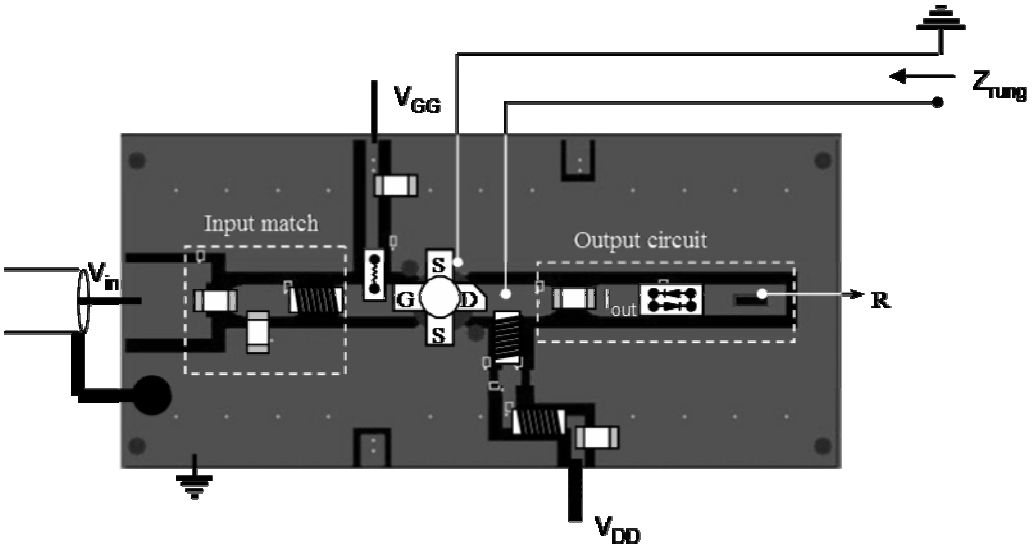

FIG. 16. PCB layout of the RF current source. The figure shows the measurement point of the rung impedance.

The network analyzer was then set to the S21 measurement mode with center frequency and sweep bandwidth set as above. The long coaxial cable was then connected to the source port and the built-in magnetic field probe was connected to the receive port of the network analyzer as shown in Fig. 17. With the MOSFET biased as described above, the center frequency and Q of the resonant peak was recorded for every setting in the range of the trimmer capacitor. The recorded data was then used to accurately compute the value of the output capacitance of the MOSFET and was used to validate the output circuit model shown in Fig. 11 through a simple computer simulation.

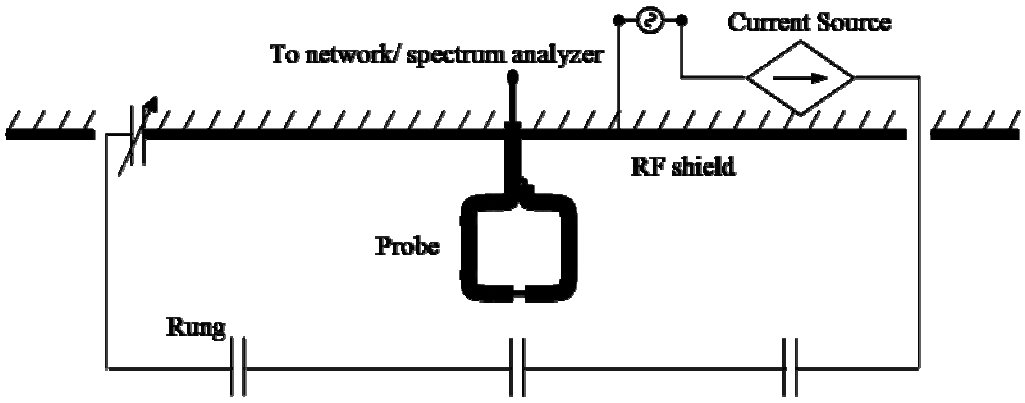

FIG. 17. Schematic of the placement of a magnetic field probe. The probe is placed between the rung and the RF shield which is the ground plane.

In order to determine the linear dependence of rung current amplitude and phase on the amplitude and phase of the input voltage, the latter was derived from the pulse sequence generator, housed in the system cabinet of the GE Eclipse 3T MRI system (GE Medical Systems in Waukesha, Wisconsin). The pulsed sinusoidal carrier was amplitude modulated (AM) with a sinc waveform. The AM signal at 3dBm power level was then amplified by a power amplifier (Minicircuits, 34dB gain, 5W maximum output power), attenuated to 15dBm and fed to the input of the controller module. Only channel one of the controller module was used and the other channels were terminated in 50 ohms. The output of channel one was fed to the input port of the RF current source.

A TDS 3054 (Tektronix) oscilloscope was used to measure the input voltage and the rung current. The rung current was measured as a voltage drop across a 10nF capacitor. The capacitive reactance of the 10nF capacitor was measured to be 2Ω. The input impedance of the measurement ports of the oscilloscope was set to 1MΩ and coaxial cables of length λ/2 were used to make voltage measurements. The λ/2 cables transferred the 1MΩ input impedance of the oscilloscope measurement ports to the point of measurement, thereby leaving the signal path on the RF current source undisturbed. The port shunt capacitance of the oscilloscope was specified at 15pF. This corresponds to a capacitive reactive reactance of 80Ω. Since this is large compared to the reactance presented by the 10nF capacitor, rung current was not influenced by the measurement apparatus.

The input voltage to the current source was measured at the output of the controller module. The current through the rung was measured indirectly by measuring the voltage drop across a 10nF capacitor connected in series with the rung. The power output of the controller module was ramped up in steps, maintaining the phase control constant. Voltage measurements were recorded at the output of the controller module and across the 10nF capacitor for each amplitude setting of the controller module. The phase relationship between the input voltage and the output current was also recorded for each setting.

IV.5. Results and discussion

IV.5.1. Determination of design constraints for RF current sources

In order to determine the range of rung impedances over which the amplifier behaves as a current source, it is essential to precisely determine the value of the parasitic output capacitance, C_{os}. Fig. 18a is a plot of the measured rung impedances for various settings of the trimmer capacitor, both in the presence (i) and absence (ii) of the MOSFET at a frequency of 127.74 MHz. At the trimmer capacitor setting of 17.5pF, corresponding to a rung impedance of (2.5+j15.5) ohms, plot (a) exhibits a parallel resonance peak. Since at parallel resonance, the reactances cancel out, the value of the capacitive reactance can be deduced from the above result to be

$$X_{C_{os}} = -j15.5\Omega$$

$$C_{os} = \frac{1}{j\omega X_{C_{os}}} = 80.3pF \qquad \text{[IV.5]}$$

Both plots, (i) and (ii), show a coincident dip in the measured impedance for a trimmer capacitor setting in the range of 7.02pF to 9.77pF. The lowest value of rung impedance occurs at series resonance and is purely resistive. The value of the trimmer capacitor at the point of series resonance of the rung is 8.8pF.

The rung forms a resonant loop with C_{os}, according to the output circuit model shown in Fig. 11. This loop is henceforth referred to as the output circuit loop. The resonance frequency of the output circuit loop depends on the value of the trimmer capacitor. Fig. 18b is a plot of the center frequency of the output circuit loop. At the trimmer capacitor value of 8.8pF, corresponding to series resonance of the rung, the center frequency of resonance of the output circuit loop is shown to be 134 MHz. The value of the MOSFET output capacitance is given by:

$$\frac{C_{os}}{C_{os}+C}=\left(\frac{127.74}{134}\right)^2$$

$$\therefore C_{os}=80.5\,pF \qquad \text{[IV.6]}$$

[IV.5] and [IV.6] are almost identical, which shows the value of C_{os} obtained is accurate.

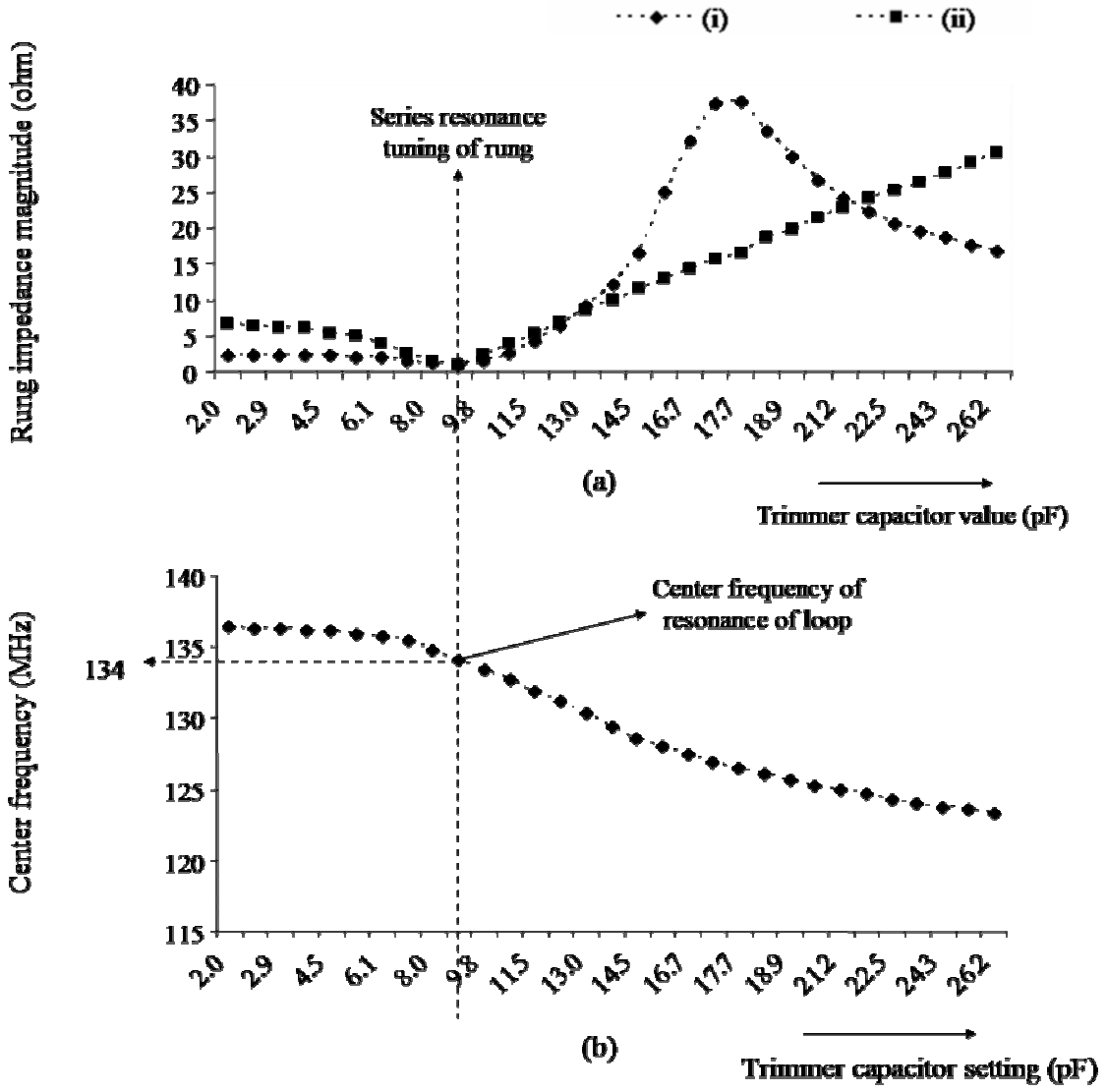

FIG. 18. Rung impedance and resonance frequency of output loop. (a) Plots of measured rung impedance with the MOSFET in the circuit and biased (i) and without the MOSFET in the circuit (ii). The coincident dip in the two plots is the area in which the MOSFET behaves as a true current source with respect to the rung. (b) Plot of the center frequency of resonance of the output circuit loop with increase in trimmer capacitance. When the rung is in series resonance, the resonant frequency of the output circuit loop is 134MHz.

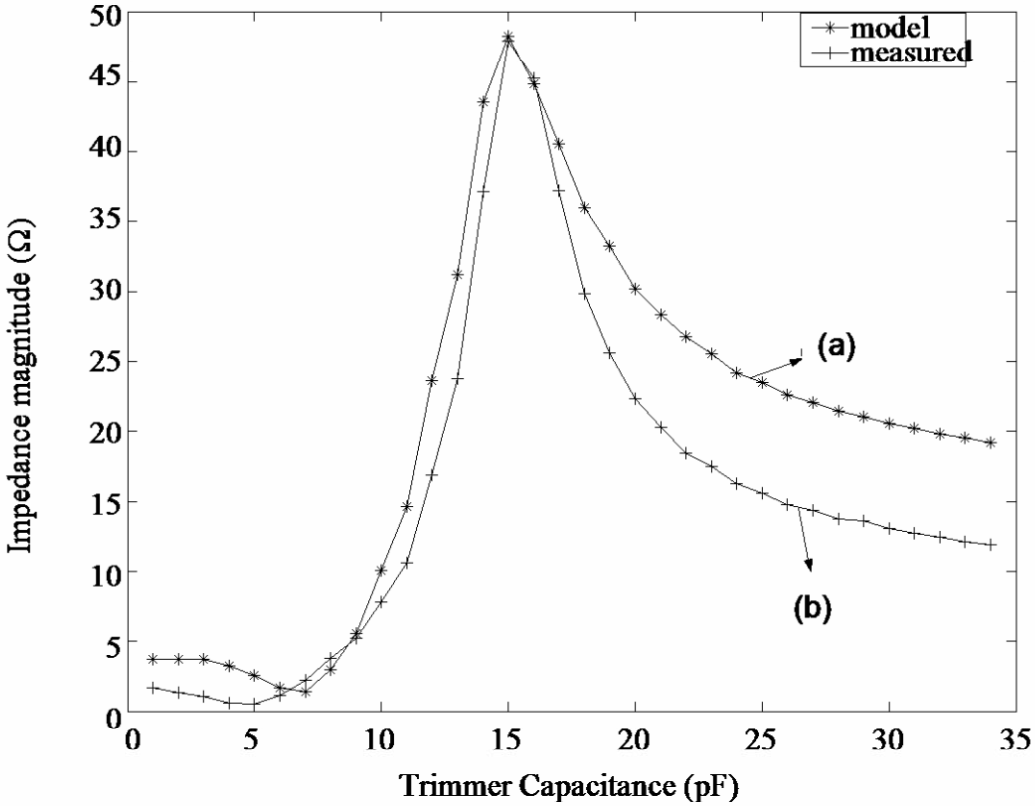

FIG. 19. Simulated curve of output circuit of RF current source. Simulated curve closely approximates the measured curve, thereby validating the output circuit model of the rung integrated amplifier shown in Fig. 11.

With knowledge of C_{os} and the rung impedances for different trimmer capacitor settings, a comparison of the calculated values of the impedance of the output circuit loop as seen from the rung terminals with the measured values shows close agreement up to loop resonance as shown in Fig. 19. Beyond loop resonance, there is a significant deviation between the calculated and measured values. The deviation may be attributed to semiconductor processes in the MOSFET, which are not accounted for here.

A significant conclusion that can be drawn from Fig. 18a is that when the rung is tuned to series resonance, it provides an alternative low resistance path to ground for RF current and is in parallel with C_{os}. For this condition, the RF current sourced from the MOSFET flows entirely through the rung. The amplitude of the rung current is linearly related to the amplitude of the gate voltage. This is confirmed by the result shown in Fig. 20. The phase difference between the rung current and the input voltage is found to be constant at 47^{o} both, with variation in amplitude of the rung current and with variation of phase of the RF gate voltage. These results show that the MOSFET behaves as a true voltage controlled RF current source for the rung when the rung is tuned to series resonance. The series resonant rung, integrated with the MOSFET can therefore be termed as a “current element”. The amplitude and phase of the magnetic field generated by the current element is linearly dependent on the RF gate voltage.

When the value of the trimmer capacitor is increased beyond the series resonance value, the rung becomes progressively more inductive with consequent increase in the magnitude of the rung impedance. It would be reasonable to expect that current in the rung would decrease as C_{os} would divert RF current from the rung. On the contrary, the probe measurements presented in Fig. 21 show that the rung current amplitude increases beyond series resonance and reaches peak amplitude slightly before the measured resonance peak of the rung. One implication of this result is that as the output circuit loop moves into resonance, the MOSFET behaves as a voltage source in series with the output circuit loop. The other implication is that the transition from a current source to a voltage source occurs with the introduction of a series impedance, which moves the

circuit into resonance at a lower value of rung inductance. The rung therefore behaves as a voltage driven element and can be represented as shown in Fig. 22.

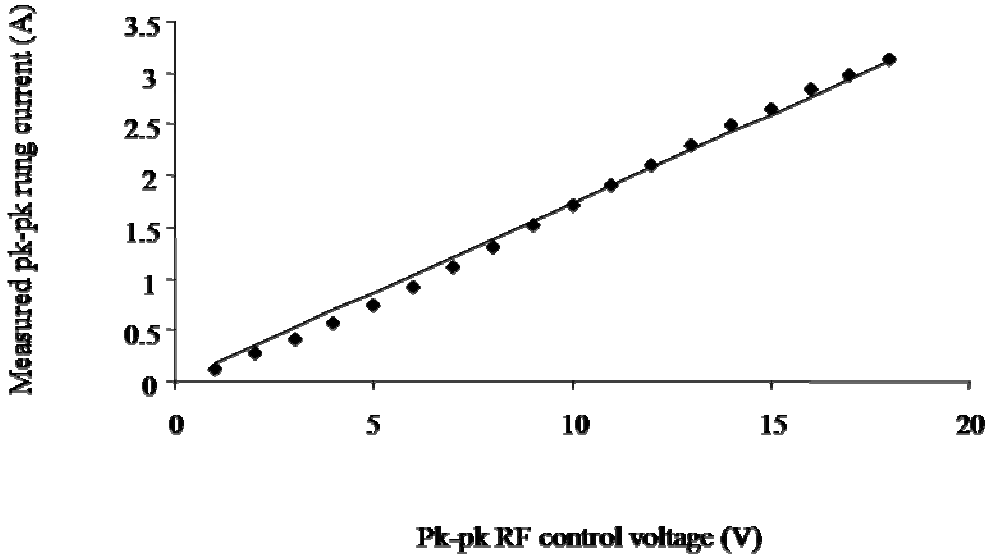

FIG. 20. Pk-pk RF rung current vs. the pk-pk RF control voltage. The solid line shows a linear curve fit applied to the data points. A maximum deviation of 28 percent occurs at the lower end of the scales. This would necessitate the use of a look-up table in order to set the current amplitude to within 10 percent of the desired value at low current amplitudes. At the higher end of the scales, the current amplitude deviates from linearity by less than 4 percent.

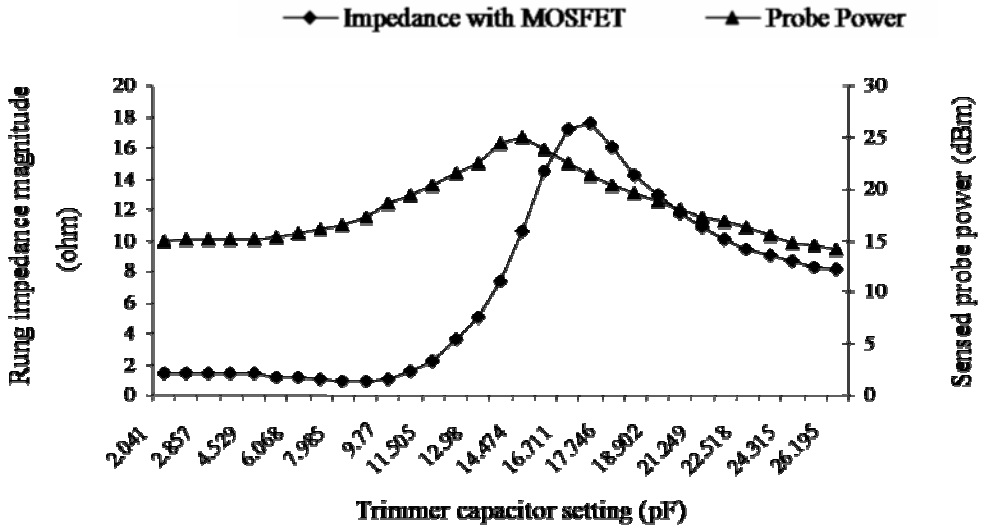

FIG. 21. MOSFET driving a parallel resonant loop. The sensed field due to rung current increases beyond series resonance and reaches a peak value when the output circuit loop is in resonance as seen by the MOSFET. It is evident that the MOSFET behaves as a voltage source in series with the resonant loop.

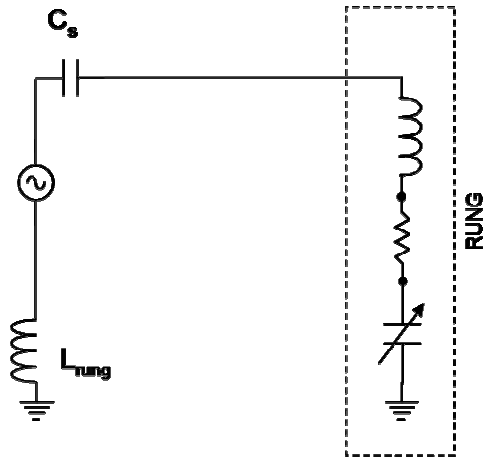

FIG. 22. Schematic of the equivalent circuit of a voltage element. The series capacitance is shown to explain the slight shift in resonance tuning of the output circuit loop as seen by the MOSFET.

Though larger rung currents may be achieved using voltage driven elements or voltage elements, the current elements have specific advantages in terms of reduced coupling with neighboring elements. It is evident from a comparison of the current element and voltage element models that the path traversed by the induced and driven currents is the same in a voltage element whereas for a current element, the induced current traverses a different loop, whose resonance frequency is shifted from the Larmour frequency as demonstrated by the results shown in Fig. 18. The topic of mutual coupling and its effect on the independent controllability of the magnetic field amplitude and phase is discussed in greater detail in the following chapter.

The gate bias voltage of the current source discussed thus far is set at 3.6 volts. This categorizes the RF current source as a class AB amplifier. The advantage of a class AB amplifier lies in its improved efficiency over a class A amplifier because it draws less direct current from the supply. However, efficiency is defined only for a standard amplifier design as the ratio of the RF power output to the DC power drawn from the supply and does not hold good for the RF current source design.

The disadvantage of a class AB amplifier is that the conduction angle of the MOSFET is less than 360^{o}. This means that the MOSFET is turned OFF for some part of the input sine wave. This introduces distortion in the output waveform. The fly-wheel effect of a resonant circuit, however, completes the waveform. In the context of the current source, this implies that the best performance in terms of linear response can be expected when the rung is tuned to series resonance.

IV.6. Summary

In summary, the key results of this chapter are:

- When the rung is tuned to series resonance, the MOSFET behaves as a linear current source.
- The range of rung impedances for which the MOSFET behaves as a true current source is limited by the output parasitic capacitance of the MOSFET.
- The amplitude and phase of the current are linearly dependent on the amplitude and phase, respectively, of the input control voltage.
- The resonance of the loop formed by the rung and the output capacitance is at a higher frequency than the Larmour frequency.
- The MOSFET transitions from a current source to a voltage source as the rung is tuned to parallel resonance with the output capacitance of the MOSFET. The loop current is higher than in the case of current source operation. However, current source mode may be the preferred mode of operation due to reduced coupling as will be discussed in the following chapter.

CHAPTER V

EIGHT CHANNEL PHASED ARRAY TRANSMIT COIL

V.1. Introduction

The RF volume coils currently used in MRI, such as birdcage coils and TEM coils, are multi-modal resonant structures. The component loops or rungs, which are the building blocks of such structures, are tuned to resonance at the Larmour frequency and are strongly coupled to each other. Hence, independent control of current amplitudes and phases on individual rungs would be difficult to achieve with conventional voltage sources as the current on one rung would induce large currents on all the other rungs. Hence, any change in the amplitude or phase of the current on one rung would strongly influence the amplitudes and phases of currents on all other rungs.

In the previous chapter, the implementation of a MOSFET voltage controlled RF current source, integrated with a rung, has been described in detail. The effects of the MOSFET parasitic capacitance, C_{os}, and rung tuning on the behavior of the MOSFET have been discussed. It is shown that the MOSFET behaves as a true current source with respect to the rung, when the rung is tuned to series resonance at the Larmour frequency. Such a tuning of the rung is henceforth referred to as “Series tuning”. A series tuned rung integrated with the current source is henceforth referred to as a “Current element”. It is also shown that when the rung is tuned such that it forms a parallel resonant loop with C_{os}, the MOSFET behaves as a voltage source for the resonant loop. Such a rung

tuning is henceforth referred to as “Parallel tuning”. A parallel tuned rung is henceforth referred to as a “Voltage controlled element” or “Voltage element” for short. It is also shown that for a current element, the center frequency of resonance of the loop formed with C_{os} is shifted substantially from the Larmour frequency.

The objective of this chapter is to show that a current element is well decoupled from the neighboring elements whereas voltage elements are strongly coupled. Experimental results are presented to prove that current elements provide superior range of current amplitude and phase control as compared to voltage elements. Finally, the current elements are placed in a volume coil configuration such that the structure as a whole is non-resonant at the Larmour frequency. A non-resonant structure is defined here as one in which the coil elements are weakly coupled to each other. The non-resonant volume coil is then used to demonstrate the capability of controlled pattern formation in the imaging volume by suitably adjusting the amplitudes and phases of the currents on the current elements. The well known modal patterns of a birdcage coil are replicated in a controlled manner by setting up the appropriate currents on the current elements.

V.2. Theory

V.2.1. Decoupling

In the previous chapter, the output circuit model of a current element was proposed and validated. Fig. 23 is a schematic of two current elements, A and B, placed close to each other. It follows from Faraday’s law of electromagnetic induction that any current on A induces an emf in B and vice-versa.

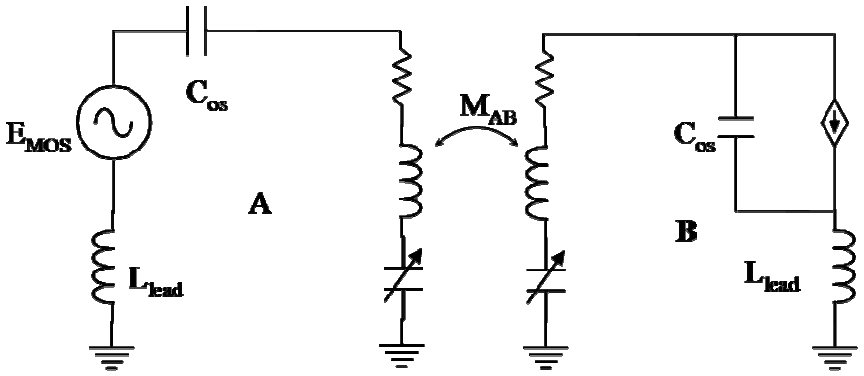

FIG. 23. Schematic of two elements placed close to each other. A is the test element and is tuned first as a current element and then as a voltage element. B is tuned as a current element. M_{AB} denotes the coupling between the two elements.

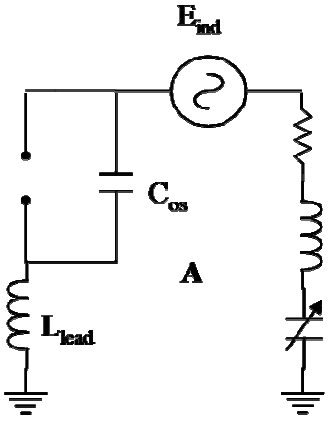

FIG. 24. Schematic of element A. Figure shows the induced emf due to current element B as a voltage source in series with the rung. The MOSFET, placed in saturation but biased OFF, is represented as an open circuit.

Let A be the test element with its MOSFET placed in its saturation region and biased OFF ($V_{GS} < V_T$, $V_{DS} = V_{DD}$), but not driven. The MOSFET can then be represented as an open circuit due to the high internal resistance in its saturation region. Let B be the current element with RF current of amplitude I_o flowing through it. Let E_{ind} be the induced emf in A due to the current in B. Element A can now be represented by the circuit schematic of Fig. 24, where E_{ind} is represented by a voltage source placed in series with the rung and the current source is replaced by an open circuit.

The complex impedance of the loop formed by the series tuned loop and C_{os} is given by

$$Z_s = R_{rung} - jX_{C_{os}} \qquad [V.1]$$

where R_{rung} is the series resistance of the rung. The rung impedance is a pure resistance because of the series tuning of the rung. The amplitude of the induced current in the loop is given by

$$|I_s| = \frac{E_{ind}}{|Z_s|} \qquad [V.2]$$

where $|Z_s| = \sqrt{R_{rung}^2 + X_{C_{os}}^2}$. Now, let the tuning of the rung be changed such that it forms a resonant loop with C_{os}. The loop impedance, Z_p, is then a real quantity and is equal to R_{rung}. The emf induced in A due to B is governed by Faraday's law of electromagnetic induction and remains unchanged for a given current on B, irrespective of the tuning of A. The amplitude of the induced current in the resonant loop is therefore given by:

$$\left|I_p\right| = \frac{E_{ind}}{R_{rung}} \qquad [V.3]$$

The ratio of the induced currents in the two cases is then

$$I_{ratio} = \frac{\left|I_s\right|}{\left|I_p\right|} = \frac{R_{rung}}{\left|Z_s\right|} \qquad [V.4]$$

Expressed in decibels,

$$I_{ratio}\Big|_{dB} = 20\left[\log_{10}\left(R_{rung}\right) - \log_{10}\left(\left|Z_s\right|\right)\right] \qquad [V.5]$$

From Ohm's law, the amplitude of current induced in a current element is dependent on the magnitude of impedance presented to the induced emf. The impedance magnitude is, in turn, governed by the magnitude of C_{os} since R_{rung} is ideally, a constant and small compared to $X_{C_{os}}$. Therefore, from [V.4] and [V.5], it is evident that the current induced in a current element is less than that induced in a voltage element. This statement is quantified experimentally in section (V.4.1).

V.2.2. Rung current amplitudes and phases for TEM coil modes

Let *N* be the number of rungs in the birdcage coil. Let *j* be the index number of the rung such that $j = 0,1,2,.....,N-1$ and *m* be the mode number. Then the modal rung currents for a linearly excited high pass birdcage coil are given by (63)

$$\left(I_j\right)_m = \begin{cases} \cos\dfrac{2\pi mj}{N} \; m = 0,1,2,....., \dfrac{N}{2} \\ \sin\dfrac{2\pi mj}{N} \; m = 1,2,3,....., \dfrac{N}{2}-1 \end{cases} \qquad [V.6]$$

For a high pass birdcage coil, mode 0 is the endring mode and is not of much interest. Modes 1 through (N-1), where N is the number of rungs, are degenerate modes

which occur at the same frequency but are opposite in sense. Therefore, in order to calculate the rung currents required to create the birdcage modal patterns, it is sufficient to consider the cosine term.

If the rung currents of another linearly excited birdcage coil are rotated geometrically through 90^o, phase shifted through 90^o and then superimposed on [V.6], then the rung current distribution of a quadrature birdcage coil is obtained. Therefore, the rung currents on a quadrature birdcage coil are given by

$$\left(I_l\right)_m = \left(I_j\right)_m + i * \left(I_k\right)_m \qquad \text{[V.7]}$$

where $l = j$ and $k = j + \left(\frac{3N}{4} - 1\right)$.The magnitude and phase of the rung currents are given by

$$\begin{aligned} \left|\left(I_l\right)_m\right| &= \sqrt{\left(I_j\right)_m^2 + \left(I_k\right)_m^2} \\ \angle\left(I_l\right)_m &= \tan^{-1}\left(\frac{\left(I_k\right)_m}{\left(I_j\right)_m}\right) \end{aligned} \qquad \text{[V.8]}$$

The rung current amplitudes are uniformly distributed over all the rungs for m=1,5. The rung current amplitudes are not uniformly distributed for m=3,7 because the two excitation points are not orthogonal to each other for these modes. The rung currents given by [V.6] and [V.8] generate respectively, linearly and circularly polarized B_1 fields in the imaging volume.

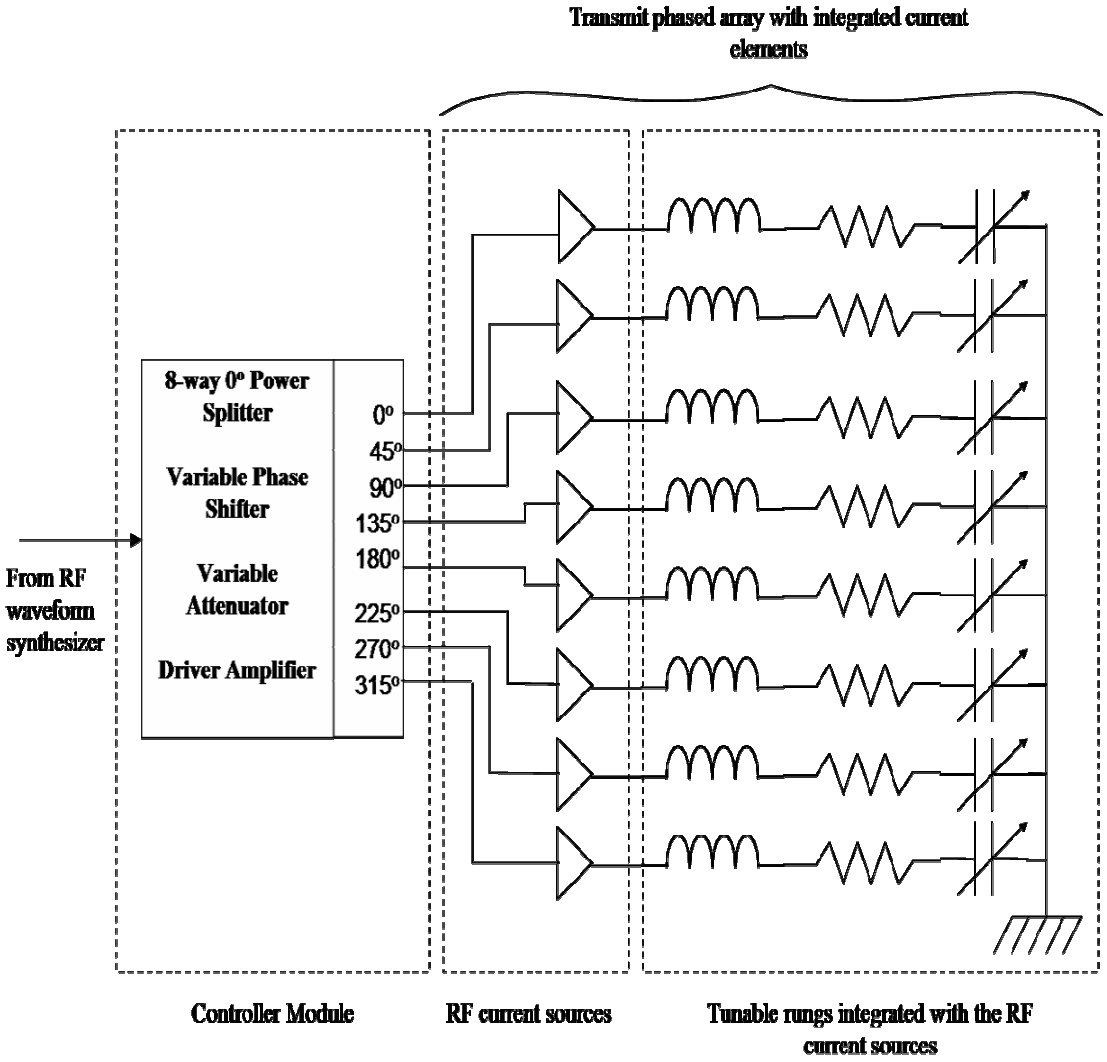

FIG. 25. The 8-channel phased array transmit coil system. In this block diagram, the B_1 field generator of each channel is a current element which consists of a rung integrated with a MOSFET voltage controlled current source. The control voltage is supplied by the controller module.

V.3. Materials and methods

Fig. 25 shows a block diagram of the transmit coil system. The transmit coil system consists of the controller module, described in chapter III and eight current elements, described in chapter IV, arranged on a cylindrical former to form a transmit phased array volume coil.

V.3.1. Construction of 8 channel volume transmit array coil

A cylindrical acrylic former was used as the base structural material for the transmit array coil design. The outer diameter of the former was 12 inches and the inner diameter was 11.5 inches. The length of the former was 12 inches. Eight rectangular acrylic strips, 11 inches long and ¾ inch wide were glued to the inner surface of the former at equal radial angles of 45^{o} with respect to each other. Strips of copper tape ¼ inch wide and 10 inches long were affixed to the long face of the rectangular strips, facing into the cylindrical cavity, such that they were centered on the strips. These were the rungs of the RF transmit coil.

An RF shield made of two flexible copper clad dielectric materials (G-10), 10mils thick, was tightly wrapped around the outer circumference of the cylindrical former. The two components of the shield were capacitively coupled such that it formed a continuous conductor for RF but was discontinuous for DC. This design was used to minimize eddy current formation on the shield due to gradient waveforms. Small rectangular holes which could accommodate a ¼ inch wide copper tape were cut out of the RF shield and cylindrical former 1 inch from either end of the former such that they opened into the cavity just beside the rectangular strips.

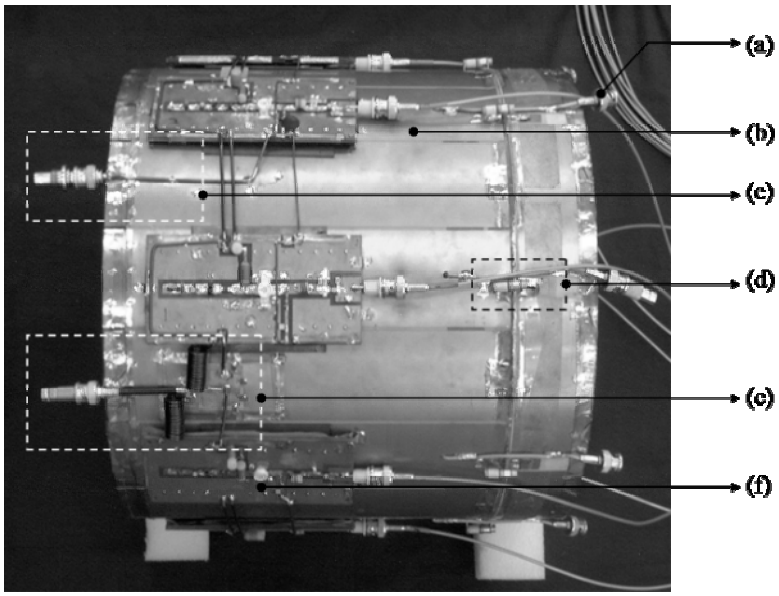

FIG. 26. Top view of the completed transmit coil. The rung integrated current sources are shown to be mounted on it. (a) is the output of the built-in magnetic field probe, (b) is the RF shield, (c) is the gate voltage input connector, (d) is the trimmer capacitor connecting the rung to the RF shield, (e) is the drain voltage input connector and (f) is the MOSFET voltage controlled current source.

The PC boards containing the RF current source circuitry as described in chapter IV were then mounted on top of the RF shield such that the rectangular opening of each PC board was aligned with the hole drilled into the former. The boards were then screwed onto the former through the mounting holes on the MOSFET flange. Short strips of ¼ inch copper tape were passed through the rectangular holes and soldered to the rungs. Each rung was divided into five segments which were connected to each other

through 47pF chip capacitors (ATC corp.). At the other end, the rungs were connected to a copper strip cut out on the RF shield by passing ¼ inch copper tapes through the rectangular holes at the other end of the former. The copper strips on the shield were then connected to the RF shield through trimmer capacitors. Fig. 26 shows a picture of the completed coil.

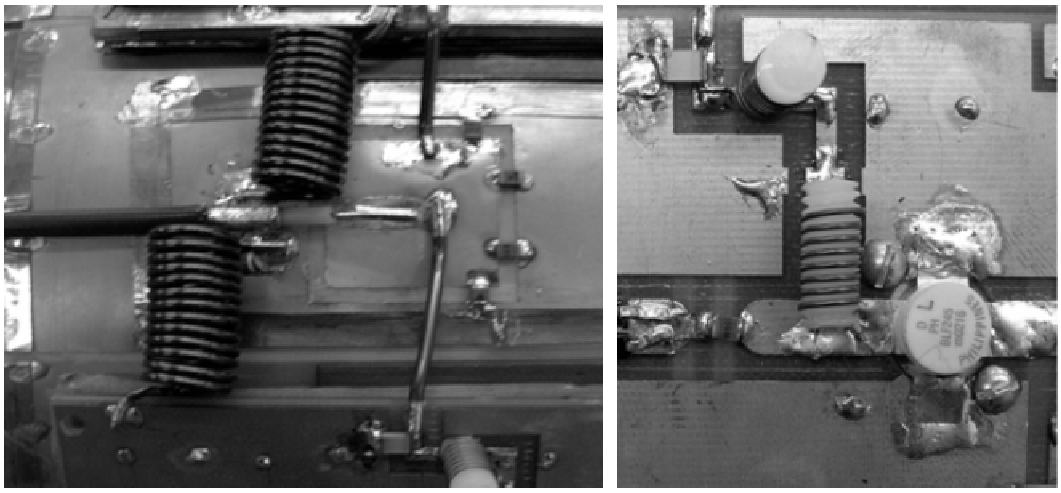

(a) (b)

FIG. 27. Implementation of MOSFET drain DC supply line. The figure shows heavy duty air-core RF chokes on the DC return path (a) and series connected RF chokes on the supply path to each MOSFET.

The RF current source boards were divided into two groups of four boards each. This was done in order to simplify the DC supply connections while at the same time, reducing the amplitude of direct current on the conductors connecting the boards to the

main supply line. The drain supply traces on boards of each group were connected in parallel using 14AWG insulated copper wire. The two groups were in turn connected in parallel to an external high current, fixed voltage DC power supply (Astron corp.) through heavy duty RF chokes as shown in Fig. 27. The gate supply traces on all eight boards were connected in parallel.

V.3.2. Bench experiments

A pair of adjacent current elements, which represented the worst case scenario for coupling, was chosen arbitrarily in order to test the theory presented in section V.2. The two current elements were labeled A and B. All coupling measurements were performed on element A, while element B was used as the source for the induction current.

A block diagram of the test setup is shown in Fig. 28. The HP 8712ES network analyzer was used as the RF source. The source was set to deliver a single frequency output at 127.74MHz at a power level of 15dBm. The output of the network analyzer was connected to the RF input connector of the controller module. Channels 1 and 2 of the controller module were used to provide the RF control voltage to the inputs of the current elements A and B respectively. The remaining channels were all set to maximum attenuation and minimum phase shift and terminated in 50Ω.

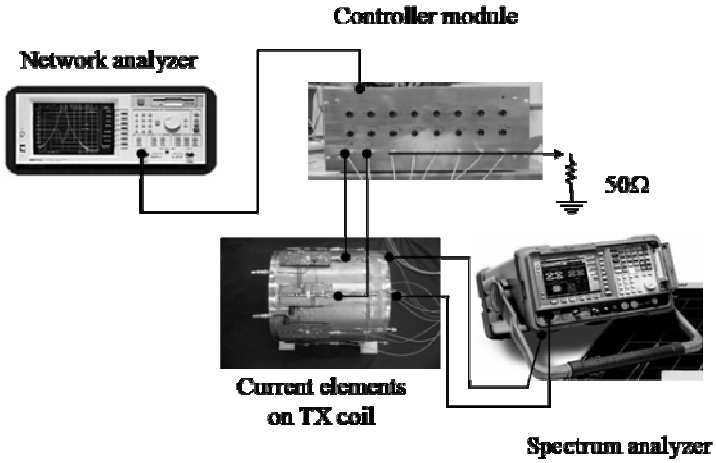

FIG. 28. Coupling between adjacent elements. A block diagram of the test setup for bench measurements of coupling between adjacent elements of the transmit coil.

The measurement apparatus consisted of a magnetic field probe mounted on a mechanism that would allow the probe to be moved in both the axial and azimuthal directions. This enabled the probe to be placed directly under the current element of interest at any position along its length. Fig. 29 shows pictures of this mechanism, which consisted of a plastic rod that was placed coincidental to the axis of the cylindrical former. A spring loaded fixture, which pressed against the inner cylinder, was mounted on the rod and fastened firmly to it. The magnetic field probe was fabricated on a small copper clad PC board as a 1cm x 1cm trace of copper and mounted on the spring loaded fixture. The current induced in the probe was transferred to the measurement apparatus by a RG316 coaxial cable, through a lattice balun that was mounted on the plastic rod at the mouth of the cylindrical cavity. The balun was used to prevent currents induced on

the cable shields from entering the measurement apparatus. This ensured reliable and repeatable measurements.

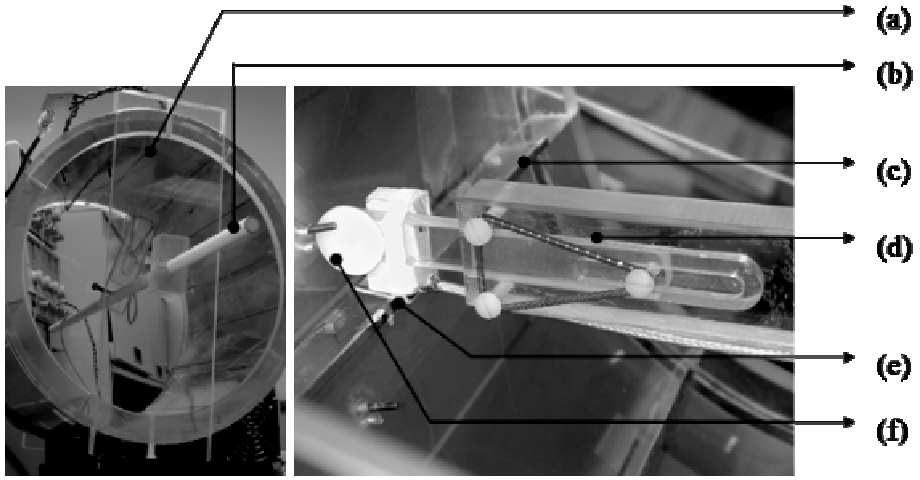

FIG. 29. Picture of the magnetic field probe fixture. Figure shows the end plates (a) used to support a plastic rod (b). A spring loaded fixture (d) which presses against the inner surface of the former is fastened to the rod. A magnetic field probe (e) is mounted on the spring loaded fixture and can be placed close to the rung (c) by moving it along the inner surface of the cylindrical former.

Two sets of four experiments each were performed in order to obtain the desired coupling data. The first set of experiments was performed with element A tuned as a current element. The second set of corresponding experiments was performed with element A tuned as a voltage element. All experiments were performed in a RF screen room. The MOSFETs were externally cooled with a fan. The MOSFETs were allowed to run at full power for a period of 15 minutes to allow them to reach thermal equilibrium.

The experiments were performed with a continuous wave sinusoidal control voltage. The experiments are described as:

- *Experiment 1*: Element A was open circuited by disconnecting the drain terminal from the rung. The current on element B was ramped up. The magnetic field probe was placed under element A. The purpose of this experiment was to determine the magnitude of the field sensed by the probe when placed under element A due to the current on element B alone. This was a baseline measurement. Comparisons between subsequent measurements were made with respect to this baseline
- *Experiment 2*: The MOSFET drain terminal on element A was reconnected to the rung. The MOSFET was turned OFF, with its drain biased to saturation. The current on element B was ramped up. The magnetic field probe was placed under element A. The purpose of this experiment was to determine the magnitude of the current induced in output circuit loop of element A.
- *Experiment 3*: The input to element A was ramped up. The MOSFET on element B was turned OFF. The magnetic field probe was placed under element A. The purpose of this experiment was to determine the magnitude of current driven in element A under no influence from element B.
- *Experiment 4*: The input to element A was ramped up. The current on element B was set to maximum amplitude. The magnetic field probe was placed under element A. The purpose of this experiment was to determine the controllable

range of the current amplitude on element A for the worst case scenario of the neighboring element carrying current at maximum amplitude.

V.3.3. Imaging experiments

The MOSFET packages were found to have a magnetic lead frame. A simple experiment was performed in order to assess how far from the sample the MOSFET would have to be in order to avoid distortion in the images due to static field warping in the vicinity of the MOSFET. A cuboidal phantom containing water doped with copper sulphate was imaged using a spin-echo sequence in the presence of the MOSFET in a GE Omega 4.7T scanner. The MOSFET was moved away from the phantom in ½ inch steps after every image taken. It was found that the MOSFET did not distort the image when placed 2 inches away from the phantom. Fig. 30 shows the progression of images as the MOSFET was moved away.

A quadrature saddle coil (see Fig. 1 for schematic and section (II.3) for brief description) was designed as a receive coil in order to perform imaging experiments. The diameter of the receive coil was arbitrarily chosen to be 8 inches. A saddle pair consisted of two loops that were placed on a cylindrical former such that they faced each other. The conductors on each loop subtended an angle of 120^{o} for optimal field uniformity (38). The two loops of the saddle coil were driven in a parallel configuration. Another similar saddle pair was implemented on the same cylindrical former such that the two saddle pairs were geometrically orthogonal to each other. When the signal from one drive point was shifted by 90^{o} in phase, the coil would sense a circularly polarized field in the sample volume. Four active decoupling networks were built, two for each saddle

pair. These ensured that the receive coil was decoupled from the transmit coil during the transmit pulse.

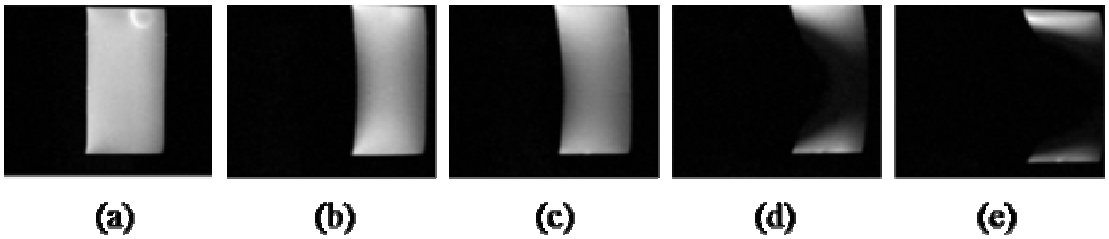

FIG. 30. Coronal images of a $CuSO_4$ doped cuboidal water phantom. Images show image distortion caused by the magnetic package of the MOSFET. (a) shows the image without the MOSFET. (b)-(e) show images with the MOSFET placed 3", 2.5", 2" and 1.5" from the phantom. These show that the MOSFET has to be placed at least 2.5" from the phantom in order to obtain undistorted images.

The transmit coil was integrated with the system cabinet of the GE Eclipse 3T scanner. It was found that the imaging system had some checks built into it that disabled image acquisitions if the system power amplifier was bypassed. The system power amplifier had two RF outputs. One was a 13kW output for the body coil and the other was a 2kW output for the head coil. The head coil output of the power amplifier was attenuated such that the maximum power input to the controller module did not exceed 15dBm at the maximum transmit gain setting allowed by the system. The eight outputs of the controller module were connected to the inputs of the eight RF current sources mounted on the transmit coil.

The drain DC power supply for the MOSFETs was provided by two 13.6V, 12A power supplies (Astron corp.) that were connected in series. In order to prevent overheating of the MOSFETs, the gate bias was provided to them only during the RF transmit pulse. The unblanking signal which is used to enable the RF power amplifier during the transmit pulse, was used for this purpose. The unblanking pulse was found to go from 3.6V to 0V during the transmit pulse. A simple unity gain inverter circuit was implemented using 741 opamp. The inverted pulse was then supplied to the MOSFET gates. The MOSFETs were thus biased to class AB operation during the RF transmit pulse.

The receive coil outputs were connected to a quadrature hybrid. A quadrature hybrid is a power combiner which phase shifts one of the input signals by 90^{o} before combining with the other signal. The PIN diode bias for the active decoupling networks was drawn from four PIN diode bias drivers. The imaging experiments were performed using the head coil configuration. Head coils are generally used in MRI as Transmit/Receive (T/R) coils. In such a configuration the T/R switch decouples the transmit chain from the receive chain and hence, there is no requirement for the PIN diode drivers. However, since the system under test was a transmit only/receive only system, the coil configuration was modified such that the PIN diode drivers were activated during the transmit pulse such that the transmit and receive coils were decoupled. The transmit loops were passively decoupled from the receive coil by using back to back diodes in series with the rungs (see Fig. 13). This step was necessary

because even though the current elements were sufficiently decoupled from each other for transmit purposes, they were not decoupled sufficiently from the receive coil.

The receive coil was centered inside the cavity of the transmit coil. A cylindrical, homogeneous silicon oil (ε_r = 2.2, σ = 0 S/m) phantom, used for all imaging experiments, was placed in the imaging volume of the receive coil. With the network analyzer (HP8712ES) alternatively set in S11 and S21 modes, the match, tune and isolation capacitors on the receive coil were iteratively adjusted until the return loss and the isolation between the orthogonal saddle coils were less than -20dB.

With the system now set up for imaging, an appropriate pulse sequence had to be chosen for imaging. A Spin Echo (SE) sequence would be the ideal sequence to demonstrate the B_1 field patterns of the transmit coil due to the cubic dependence of the signal intensity on the amplitude of the B_1 field (10). However the low current handling capacity of the MOSFETs used would not ensure a 90^o flip angle in the center of the phantom. Therefore, Gradient Echo (GE) pulse sequence with low flip angle and short echo time (TE) was chosen as a viable alternative, to obtain the images. The imaging parameters are listed in Table 2. From equation (II.4), it is evident that a low flip angle minimizes T1 effects and short TE minimizes T2 effects. The resulting images, therefore, were spin density maps, which are a better approximation of the B_1 fields.

Table 2

List of imaging parameters. The parameters listed are used to image the silicone oil phantom with the transmit coil array. These parameters are entered into the GUI on the control computer of the GE Eclipse 3T imaging system.

Imaging parameter	Setting
Imaging plane	Axial
Dimensions	2
TE	20 ms
TR	800 ms
Flip angle	20^{o}
Field of View (FoV)	48 cm
Slice thickness	5 mm
Number of slices	1
Image matrix size	128 X 256
NEX	1

A MATLAB code was written using equations [V.6] and [V.8] to calculate the current amplitudes and phases on the current elements required to set up linear and quadrature birdcage mode patterns. The current amplitudes and phases on the current elements were set using the controller module. For linear birdcage mode patterns, the relative phase between the current elements was set to zero and only the current amplitudes were adjusted. For the quadrature birdcage mode patterns, the current amplitudes were set to fixed ratios and only the relative phases were adjusted. All the images obtained were compared to simulated field patterns of birdcage coil modes.

V.4. Results and discussion

V.4.1. Bench experiments

The B field sensed by the probe under the open circuited current element A, due to current element B alone, is a baseline measurement and is a good reference for subsequent measurements recorded at the same location. Comparisons are drawn as ratios between the induced currents in series and parallel tuned circuits as described by equation [V.4]. These are expressed as differences in the logarithmic scale as described by equation [V.5].

A current on the rung generates a magnetic field, whose amplitude is proportional to that of the rung current. The magnetic field, in turn, induces an emf on the magnetic field probe placed close to the rung. The amplitude of the current induced is proportional to the amplitude of the magnetic field and hence to that of the rung current. The measurement, recorded as a power level, is proportional to the square of the current on the probe. However, from equation [V.5] and the fact that

$20\log\left(I_s/I_p\right)=10\log\left(P_s/P_p\right)$, difference in dB of the recorded probe power measurement reflects the same difference in dB, in rung currents.

With reference to Fig. 31, the average increase in B_1 field strength sensed by the magnetic field probe due to current induced by current element B in series tuned rung of element A is 13.6dB. This means that with the MOSFET in A turned OFF, the B_1 field generated by the induced current is a factor of 4.8 higher than that due to element B alone. For the parallel tuned case, the increase in field due to induced rung current is 29.12dB by average or a factor of 28.6 over the baseline. The average difference in the measured induced currents in the series and parallel tuned cases is 15.52dB.

The resistance of the series tuned *rung* (current element) is measured to be 0.4Ω. The impedance of the parallel tuned *rung* (voltage element) is measured to be (2.7+j15.8)Ω. Therefore, the impedance of the series tuned *loop* at a frequency of 127.74MHz is (0.4-j15.8)Ω and the impedance of the parallel tuned *loop* at the same frequency is 2.7Ω. Substituting these values in [V.4] and [V.5], the current in the voltage element is found to be greater than that in the current element by 15.34dB. The calculated and measured values are in good agreement.

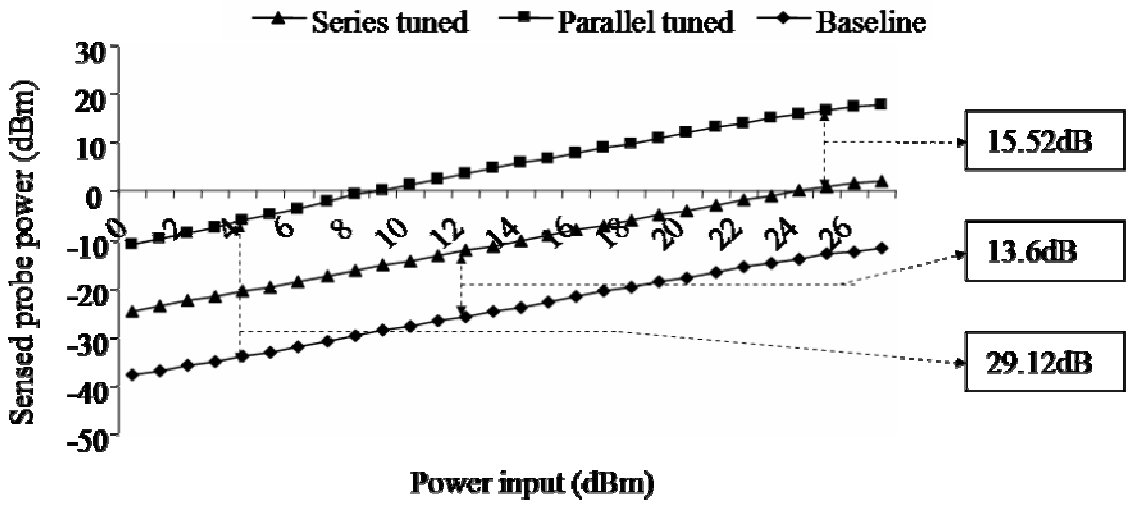

FIG. 31. Plots of B_1 field measurements. Measurements are made using the magnetic field probe placed directly under element A. The baseline measurement was made with A open circuited. The series tuned and parallel tuned measurements were made with A tuned as a current element and voltage element, respectively. The average differences in dB, between the measurements are shown.

The results presented above show that the induced current in a current element is a factor of 6 less than that induced in a voltage element. This is due to the fact that in a voltage element, the driven and induced currents traverse the same resonant path. In a current element, the driven current traverses the loop formed by the series tuned rung and the current source while the induced current traverses the loop formed by the same rung and C_{os}, since the internal resistance of the current source is very high. It is therefore evident from the theory and results presented that a smaller value of C_{os} results in improved suppression of induced current.

The curves shown in Fig. 32 are plots of B_1 field measurements made under element A with both elements tuned as current elements. Curve (a) is a plot of measurements due to the current on element B alone. This is the baseline measurement shown in Fig. 31 above. Curve (b) is the plot of the B_1 field sensed by the probe due to the induced current on element A. Curve (c) represents the B_1 field sensed by the probe due to current in element A alone and curve (d) represents the resultant B_1 field sensed by the probe due to the current on element A with element B carrying maximum current. This represents the worst case scenario for coupling between neighboring current elements.

Curve (d) can be divided into three regions as shown above. In region 1, the field sensed by the probe is predominantly due to the currents induced on element A by current on B. Region 2 is where the magnitude of current on A is comparable to that induced by B. Hence the field sensed by the probe is the resultant field due to the resultant of the driven and induced currents on A. Region 3 is where the driven current in A dominates the induced current due to B and the magnetic field probe senses the field predominantly due to A.

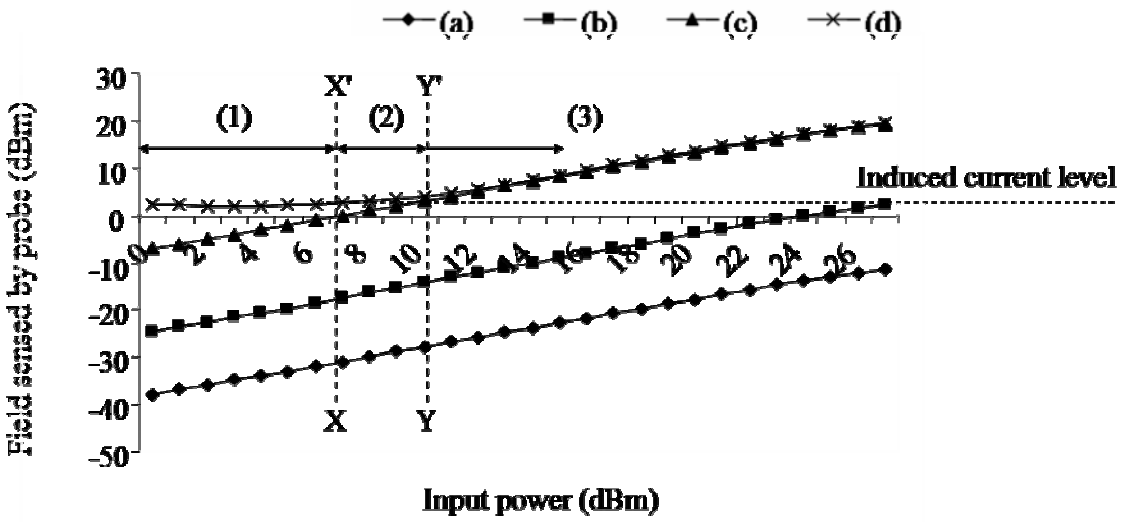

FIG. 32. Controllable range of rung currents on current element. Curves show the controllable range of current amplitudes and phases on the current element. (a) is the baseline measurement, (b) is the sensed field due to induced current on current element A, (c) is the sensed field due to driven current on A with the current element B tuned OFF and (d) is the sensed field due to driven current on A with element B carrying maximum current. Region (1) of curve (d) is induced current dominated and region (3) is driven current dominated. The current probe senses the resultant current due to driven and induced currents on A in region (2).

The curves in Fig. 33 correspond to those in Fig. 32 and are due to element A, tuned as a voltage element. Comparison of curves (b) and (c) in this case shows that the induced current is on an average, only 5.2 dB down from the driven current. This is only a factor of 1.8 less than the driven current. For the worst case scenario of maximum current on element B, the driven current on element A never completely dominates the induced current. This is borne out by the fact that curve (d) can be divided into only two regions where region 1 is induced current dominated and region 2 represents the resultant field due to the driven and induced currents.

The field measurements have been made with a small magnetic field probe placed very close to the rung in order to reflect the behavior of the current on the rung under consideration. The baseline measurement confirms that the field due to a neighboring rung is well attenuated at the point of measurement so that the field probe is sensitive to small currents on the rung under consideration, whether induced or driven.

The results presented for a voltage element show that significant induced currents from neighboring elements determine the amplitude and phase of the resultant B_1 field. While it may be easy to predict the amplitude and phase of the resultant B_1 field due to a pair of elements, introduction of an arbitrarily large number, N, of such voltage elements in the vicinity would make such a prediction a complicated exercise. The reverse problem of determining the amplitude and phase of the drive voltages for the N MOSFETs, required to generate a desired B_1 field at some arbitrary point in space would be highly complex and perhaps, untractable.

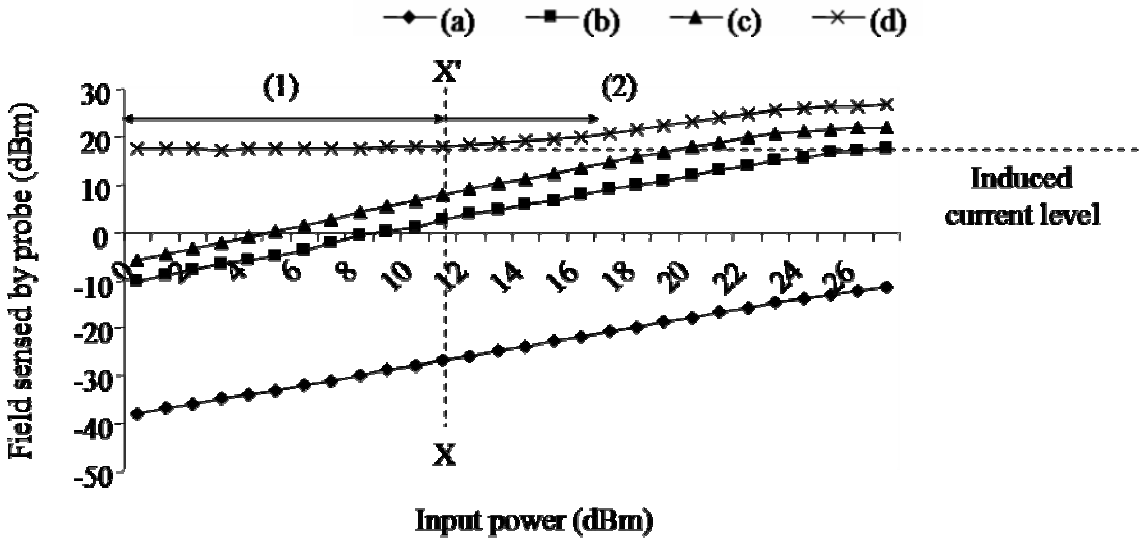

FIG. 33. Controllable range of rung currents on voltage element. Curves show the effect of induced currents on the controllable range of current amplitude and phase on voltage element, A. (a) is the baseline measurement, (b) is the sensed field due to induced current on element A, (c) is the sensed field due to driven current on A and (d) is the sensed field due to driven current on A under worst case conditions of maximum current on B. This set of curves shows that there is no region dominated by the driven current on A.

The results presented for the current element show that independent control of the amplitude and phase of the B_1 field may be achieved in region 3. This means that current elements generate B_1 fields whose amplitude and phase are completely determined by the driven current on the respective rungs and by extension, the MOSFET drive voltage, regardless of the number of neighboring elements. It would therefore be an easy problem to achieve the desired B_1 field at any arbitrary point in space because of the exact knowledge of the B_1 fields generated by the current elements. In the following section, imaging results are presented to demonstrate this property of current elements.

V.4.2. Imaging experiments

The images obtained using several combinations of current elements and current amplitudes and phases on them are shown in appendix C. The imaging results presented in this section demonstrate the capability of the transmit array to generate controlled B_1 patterns by linearly adjusting the amplitudes and phases of the currents on the current elements.

The simulated field patterns of the degenerate modes of an 8-rung TEM resonator, excited at a single port, are shown in row (A) of Fig. 34. These modal field patterns are generated by current amplitude distributions as shown in the corresponding charts in row (C). For single port excitation, the relative phase between the rung currents is zero. Images obtained by setting up similar current amplitude distributions on the current elements that make up the transmit array show field patterns that are in close agreement with the simulated results. It should be noted however, that with the transmit array, the modal patterns are generated at a single frequency, the Larmour frequency, by

independently controlling the current amplitudes on the current elements. This demonstrates the advantage of independent control of current amplitude on the current elements.

The simulated field patterns of the degenerate modes of a quadrature excited 8-rung TEM coil are shown in row (A) of Fig. 35. In this case, the modal field patterns are generated by the current phase distributions on the rungs as given by the charts shown in row (C). The current amplitudes are held constant and equal on all the rungs. Comparison of the real and simulated images shows that there is a good correspondence between modes 1 and 5. This could be explained by the fact that excitation ports are orthogonal to each other for modes 1 and 5 and hence the fields do not interfere with each other. For modes 3 and 7, the excitation points are not in quadrature and hence the currents do not add up to produce circularly polarized fields. In the case of the transmit coil, the current amplitude was held constant on all the rungs and the phase was varied, thus creating modal patterns that closely match the simulated patterns.

The bright spots seen at the edges of both, the simulated and real images is due to the fact that the phantom almost completely filled the cavity of the receive coil. Since the magnetic flux density is the highest near a current carrying conductor, the B_1 field patterns show bright spots in these regions.

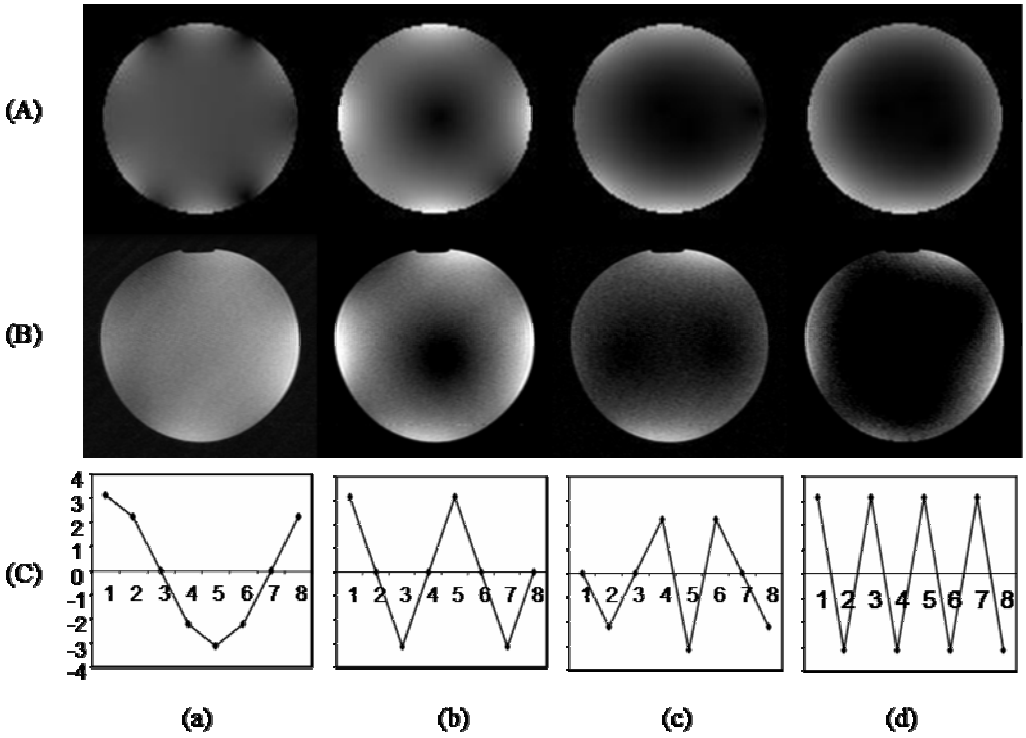

FIG. 34. Modal patterns of a linearly excited resonant coil. Generation of modal patterns of a linearly excited resonant coil such as a TEM coil using the transmit array with a non-resonant structure. The figure is a [3 x 4] matrix with rows labeled (A)-(C) and columns labeled (a)-(d). The simulated modal patterns of an 8 rung TEM coil are [(A), (a)-(d)] are obtained by exciting the modes at their characteristic frequencies of 130.38 MHz (a), 131.94 MHz (b), 132.9 MHz (c) and 133.23 MHz (d). These modal patterns are generated at a single frequency (127.74 MHz) by the non-resonant transmit phased array [(B), (a)-(d)] by setting the current amplitude distributions on the current elements as shown in the charts of [(C), (a)-(d)]. The relative phases are set at zero.

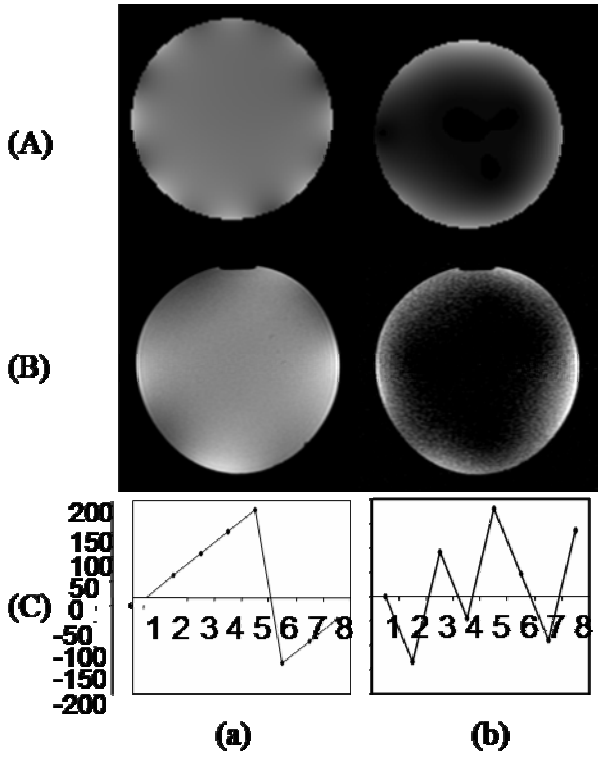

FIG. 35. Modal patterns of a quadrature resonant coil. Generation of modal patterns of a quadrature resonant coil such as a TEM coil using the transmit array with a non-resonant structure. The figure is a [3 x2] matrix with rows labeled (A)-(C) and columns labeled (a) and (b). The simulated modal patterns of an 8 rung TEM coil are [(A), (a), (b)] are obtained by exciting the modes 1 and 5 at their characteristic frequencies of 130.38 MHz (a) and 132.9 MHz (b).For modes 3 and 7, excitation at the quadrature points do not produce orthogonal fields and hence the resultant fields are not circularly polarized. These modal patterns are generated at a single frequency (127.74 MHz) by the non-resonant transmit phased array [(B), (a)-(b)] by setting the current phase distributions on the current elements as shown in the charts of [(C), (a)-(b)]. Current amplitudes are held constant for both modes.

Mode 7 of the linear excitation image does not seem to agree well with the simulated image. This could be attributed to the fact that as shown in the simulated images, the mode 7 B_1 field is intense in the regions close to the conductors and attenuates quickly towards the center. Since the phantom in the transmit coil had to be placed far away from the current elements due to the magnetic nature of the MOSFETs, the B_1 field may have attenuated considerably before reaching the phantom.

The mode patterns of a birdcage or TEM coil occur at distinct frequencies as determined by the mutual inductances between their resonant loops. This is characteristic of a periodic, resonant structure. The resonant modes of a resonant structure are a potential liability at high field strengths. Load-coil interactions at high field strengths cause significant shift in the resonant frequency of the loops of a resonant coil. With asymmetric loading, the resonant frequencies of the heavily loaded loops may shift more than those of the lightly loaded loops, thereby exciting higher order modes in some loops. This phenomenon is called mode mixing and some of the B_1 inhomogeneity may be attributed to this (3).

In contrast, the mode patterns of the non-resonant transmit array of current elements are generated at a single frequency, the Larmour frequency, by adjusting the amplitudes and phases of the currents on the current elements. This ability of the transmit array to generate controlled B_1 patterns could potentially be a useful tool to optimize homogeneity in the presence of lossy dielectric loads. For instance, it is known that images of samples with high dielectric constants have a bright central spot with alternating dark and bright bands around it (6,12,29,35,64,65). This is a typical

interference pattern. In such cases, it may be advantageous to generate a mode 2 or mode 3 pattern or even a combination of modal patterns which would be possible with a current element array due to results presented in section (V.4.1).

Resonant coils such as the birdcage and TEM coils are highly efficient as they exhibit high current gain. This is the nature of a resonant structure. The main disadvantage of the transmit array design is its low efficiency. The amplitude of the current driven through the rung is entirely dependent on the MOSFET drive voltage and the current handling capacity of the MOSFET. Therefore, the large current requirements of bigger volume coils would necessitate the use of MOSFETs with very high current handling capacity. However, efficiency is only a secondary requirement in transmit coil design. The specification of primary importance in transmit coil design for high field imaging is B_1 field homogeneity in the presence of asymmetrically placed lossy dielectric loads such as the human body. It is shown in literature that resonant coils do not meet that specification. It would also be very difficult to implement multi-port excitation on a resonant coil, in order to optimize B_1 field homogeneity, because of the results presented in section (V.4.1) for a voltage element. The demonstrated ability of the transmit array to generate desired field patterns by independently controlling the current amplitude and phase on the component current elements may be used to optimize B_1 field homogeneity in a simple and predictable manner.

As a final comment, silicone oil has a very low dielectric constant ($\varepsilon_r = 2.2$) and is lossless ($\sigma = 0$ S/m). It is therefore a non loading phantom that does not produce any phase shifts in the B_1 fields. The rationale for the selection of such an imaging medium

lies in the fact that the objective of the imaging experiments is to demonstrate that the array of current elements are able to generate controlled B_1 field patterns in the imaging volume and not to optimize field homogeneity. The results of these experiments can later be used to optimize the B_1 field homogeneity in lossy, high dielectric media.

V.5. Summary

In summary, this chapter has demonstrated the following:

- Superior decoupling between neighboring current elements.
- Independent control of current amplitudes and phases on the current elements over a wide range of drive voltage amplitudes.
- Controllable field patterns in a silicone oil phantom due to the transmit array which consists of 8 current elements arranged in a volume coil configuration.

CHAPTER VI

CONCLUSIONS, FUTURE WORK AND APPLICATIONS

VI.1. Conclusions

Volume coils such as birdcage and TEM coils are highly efficient, resonant structures that are excited by voltage sources at the Larmour frequency. At frequencies of 64 MHz and above, it is common to use two voltage sources in space and time quadrature to generate a circularly polarized B_1 field. However, at 128 MHz and above, the parasitic capacitances between the load and coil approach the same order of magnitude as the tuning capacitors, thus making the coil current distribution sensitive to loading. This leads to degradation in the circular polarization, resulting in B_1 field inhomogeneity. Further, load dielectric properties shorten the wavelength, thereby causing phase shifts, leading to formation of interference patterns within the load. Finite Difference Time Domain (FDTD) simulations have shown that excitation of all 24 ports of a TEM coil, with the ability to control the amplitudes and phases of the excitation sources independently of each other, enable optimization of the B_1 field homogeneity (33). However, coupling effects in a resonant system excited by standard voltage sources makes the effective impedance of each leg dependent on the current in the other legs. Thus adjusting the excitation voltages to obtain the desired currents requires detailed knowledge of this (load-dependent) coupling or a time-consuming iterative procedure.

The single most important contribution of this dissertation to the existing body of knowledge on RF coil design is the design, development and study of RF current sources integrated with the magnetic field generator or rung. A MOSFET based voltage controlled RF current source has been implemented as a modification of standard RF power amplifier design. The true current source operation of the MOSFET is found to be constrained by the parasitic output capacitance of the MOSFET. The range of rung impedance values within which the MOSFET behaves as a true current source with respect to the rung has been established. It has also been found that for maximum linearity of response, the rung should be tuned to series resonance at the frequency of interest. Linear dependence of rung current amplitude and phase on the amplitude and phase of the input control voltage has been demonstrated.

A controller module has been designed and built in order to provide the RF current source with the RF control voltage. The linear range of control of the amplitude and phase of the RF control voltage has been established as a function of amplitudes of the DC control voltages used to control the attenuators and phase shifters in the controller module. This is a very significant result which shows that the amplitude and phase of the magnetic field generated by the current on the rung can be directly controlled by the DC control voltages that are used to control the attenuators and phase shifters in the controller module.

Another significant result that is discussed in chapter IV is that the resonance frequency of the loop formed by the rung and the parasitic output capacitance of the MOSFET is substantially shifted from the Larmour frequency. It has been shown

through simulation of the output circuit model that extent of the frequency shift depends on the value of the output capacitance. In other words, lower the output capacitance, greater the shift away from the Larmour frequency. Since the induction currents follow this path, the amplitude of the induction currents is significantly reduced compared to its amplitude had the loop been on resonance at the Larmour frequency. This fact has been demonstrated in chapter V with measurements recorded from adjacent rungs. The significance of this result is that adjacently placed rungs or current elements are weakly coupled to each other with the resultant increase in the range over which independent control over the amplitude and phase of the currents on the rungs can be exercised by the attenuators and phase shifters of the control module. This means that the magnetic field pattern inside a sample can be controlled by adjusting the current amplitudes and phases on each of the rungs independently of the others. In other words, the importance of mutual impedances is significantly diminished. This capability of pattern control of the B_1 field has been demonstrated in chapter V with the generation of field patterns of various birdcage coil modes.

In conclusion, a volume coil phased array has been implemented in a non-resonant structure. The array is composed of rungs integrated with MOSFET RF current sources. The current amplitudes and phases on the rungs can be adjusted independently of each other by adjusting the amplitudes and phases of the control voltages input to the RF current sources. This results in the generation of controlled B_1 field patterns, a feature that would be useful for optimization of B_1 field homogeneity in an asymmetrically placed lossy load at high field strengths.

VI.2. Future work

The ultimate objective for research in transmit coil design driven by RF current sources would be to implement a whole body RF coil for human imaging at ultra-high field strengths of 7T and above. The capability of such a coil would include the ability to optimize the B_1 field homogeneity in real time through a simple feedback loop. The foundation for such a system has been laid in this work, where it has been established that the B_1 field generated by a current element is a linear function of the DC voltages that control the attenuation and phase shifts in the controller module. However, there are a number of areas that would require further study. Some of these are discussed in this section.

VI.2.1. The RF current source

The MOSFET used in this work can drive a peak current amplitude of 1.75A into the rung. This is not sufficient to create a 90^o flip angle in the center. Hence, MOSFETs with higher current handling capacity have to be used in order to image with the spin echo sequence. Unfortunately, MOSFETs with higher current handling capacity also come with larger parasitic capacitances.

Alternatively, a push-pull design could be considered, where two MOSFETs are driven 180^o out of phase with each other. One possible configuration of such a design is shown in the schematic of Fig. 36. In this configuration, C_{os} of the MOSFET 2 would be used as part of the series resonant rung connected to MOSFET 1 and vice-versa. When driven 180^o out of phase, with class A gate biasing, this would lead to doubling of current in the rung.

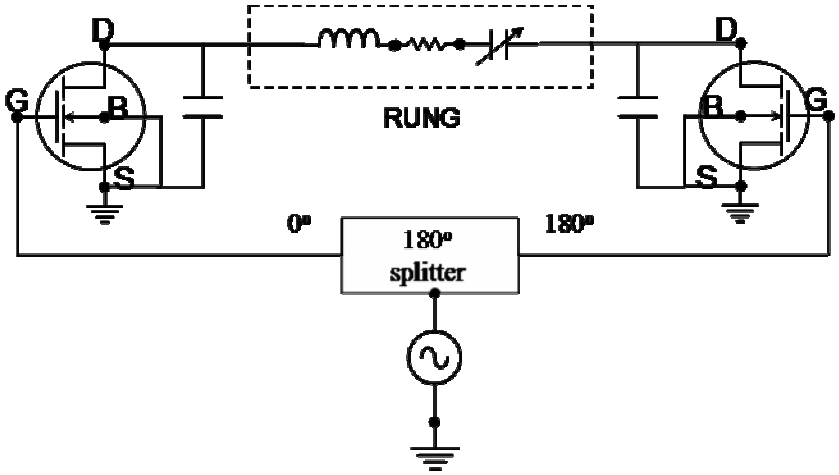

FIG. 36. Push-pull configuration of MOSFETs. This would be a balanced configuration with the C_{os} of either MOSFET used as part of the series resonant rung as seen by the other MOSFET.

As another alternative, the output currents of several small MOSFETs could be combined using principles of distributed amplification. Current combining techniques would need to be investigated.

MOSFETs are generally enclosed in plastic packages with a lead frame. The MOSFET terminals are wire-bonded to the lead frame. Unfortunately, the lead frames used by most MOSFET manufacturers are made of an alloy of iron and nickel, called Alloy42. Iron and nickel are both ferromagnetic and will cause severe distortions in the static magnetic field homogeneity leading to severe image distortion. In an experiment described in chapter V, it was found that no noticeable distortion occurred if the sample

was placed about 2.5 inches away from the MOSFET. This result was used in the design of the receive coil for this work. Therefore, if the receive coil is to be built big enough to accommodate the human head, the size of the transmit coil would have to be increased by the same amount. While this may not be a constraint for head coils, it would be an important issue for body coil designs where radial space is at a premium. Alternatively, a remote current source design may be considered, where a coaxial cable whose length is a multiple of $\lambda/2$ can be used to conduct the RF current to the coil elements. In this case, the effects of cable coupling and cable losses would have to be assessed carefully.

VI.2.2. Homogeneity optimization

This work describes the generation of controllable magnetic field patterns in the sample volume. The field patterns have been generated in a homogeneous silicon oil phantom. As discussed in chapter V, silicon oil has a low dielectric constant and is lossless and as such does not represent real imaging situations. The next logical step is therefore to use the capability to independently control current amplitudes and phases on the rungs to optimize the B_1 field homogeneity in the presence of homogeneous dielectric and lossy loads by superimposing the various birdcage modes. Quantitative assessments of sensitivity to the type and position of the load within the coil would have to be made.

VI.2.3. Receive coil

This work describes the implementation of a transmit only coil design. In order to investigate the effectiveness of the transmit coil in optimizing the B_1 field homogeneity in the presence of lossy, dielectric loads, a good volume receive coil would

be required. One option would be to design a stand-alone receive-only coil that could accommodate the human head and at the same time, fit into the transmit coil former. This would necessitate increasing the size of the transmit coil. High voltage MOSFETs may have to be used in order to generate the currents required to enforce a 90^{o} tip angle in the center of the sample. The other option would be to convert the existing transmit only coil into a transmit/receive configuration by implementing PIN diode switches to switch resonating elements into the circuit. In order to understand the design requirements for such an arrangement, a simple surface coil loop could be implemented in transmit/receive mode. Fig. 37 illustrates such a transmit/receive loop. During transmit mode, the capacitor that is part of the matching network could be switched OFF by reverse biasing the PIN diode. The series tuning capacitor in the RF current path could be tuned to series resonate the current loop. During receive mode, the matching capacitor would be switched back into the circuit by forward biasing the PIN diode.

VI.3. Applications

Current elements are versatile magnetic field generators and can be used in several configurations, custom made for specific applications. One area that has been discussed in this dissertation, that is the motivation for the development of this technology, is for optimization of B_1 fields in the presence of asymmetrically placed lossy dielectric loads for high field MRI. Two other applications of current elements, not necessarily at high fields, are described below

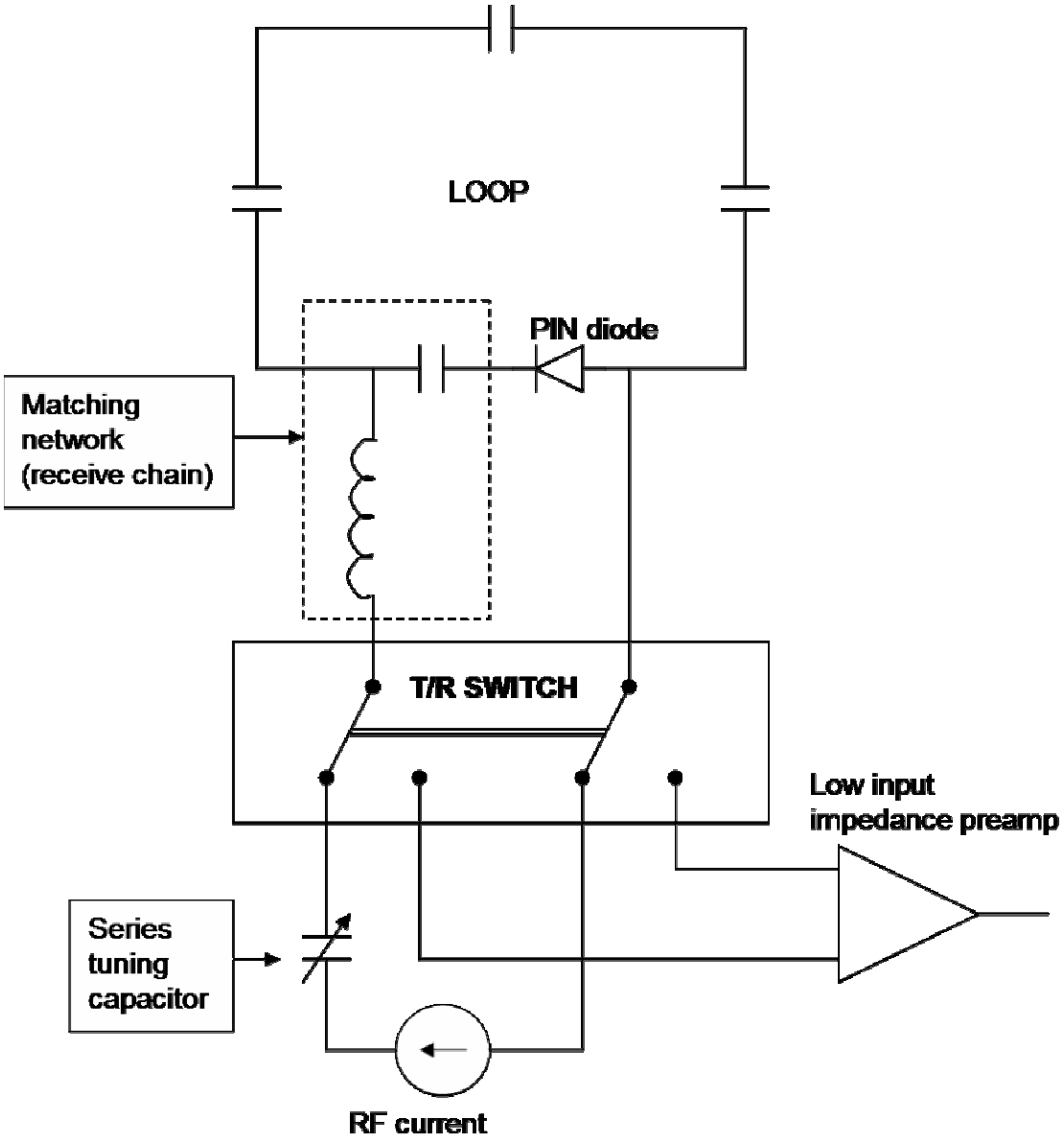

FIG. 37. Simple surface coil loop. The loop could be switched between current element mode and resonant receive mode.

VI.3.1. Surface transmit/receive coils

The current elements could be placed in specific arrangements and the current phase and amplitudes could be set so as to obtain any desired excitation pattern. A simple example would be a rectangular loop, in which only the z-directional currents generate useful fields. Conductors in the transverse direction only serve to complete the circuit. The size of each loop has to be varied for different applications and hence would have to be constructed all over again with different component values. On the other hand, a pair of current elements, placed parallel to each other along the z direction, with current phase relation of 180^{o} would achieve the same result. The distance between the current elements could be adjusted to simulate any size of rectangular loop.

VI.3.2. Spatially selective excitation

Multi-dimensional spatially selective excitation (66-70) can be used in a number of applications such as fast imaging with field-of-view restriction, selective flow tagging (68), three dimensionally localized spectroscopy (67) and curved slice imaging (71), among others. Spatially selective excitation is implemented using specialized magnetic field gradient pulses. In such applications, the volume transmit array would be useful in providing selective RF excitation in the region of interest by turning ON the required number of current elements, thus reducing the RF power requirement. This would be possible because the current elements are well decoupled from each other as described in chapter V.

VI.3.3. Transmit SENSE

Transmit SENSE (71) is a recent development that is specifically intended to reduce the RF pulse length during multi-dimensional spatially selective excitation. This involves the use of multiple RF transmit coils, each of which exhibits a spatially different sensitivity pattern and is driven by a specific RF waveform in order to shorten the path of k-space traversal, thereby reducing the RF pulse length. Innovative methods have been used to implement such transmit coils in order to demonstrate the principle of transmit SENSE (71). However, in practical situations, such methods defeat the purpose of technique.

Transmit arrays, with decoupled current elements, would be ideally suited for transmit SENSE applications. The additional hardware requirements would be a dedicated modulator and waveform synthesizer for each channel.

REFERENCES

1. Lauterbur PC. Image formation by induced local interactions: example employing nuclear magnetic resonance. Nature 1973;242(190):3-6.

2. Hayes CE, Edelstein WA, Schenck JF, Mueller OW, Eash M. An efficient, highly homogeneous radiofrequency coil for whole-body NMR imaging at 1.5 T. J Magn Reson 1985;63:622-628.

3. Tropp J. A model for image shading in multi-mode resonators. In: Proceedings of the 9th Annual Meeting of ISMRM; Glasgow, 2001; 1129.

4. Roschmann PKH. High-frequency coil system for a magnetic resonance imaging apparatus. U.S. patent 4,746,866; 1988.

5. Vaughan JT, Hetherington HP, Otu JO, Pan JW, Pohost GM. High frequency volume coils for clinical NMR imaging and spectroscopy. Magn Reson Med 1994;32(2):206-218.

6. Ibrahim TS, Lee R, Abduljalil AM, Baertlein BA, Robitaille PM. Dielectric resonances and B(1) field inhomogeneity in UHFMRI: computational analysis and experimental findings. Magn Reson Imaging 2001;19(2):219-226.

7. Freeman R. Spin choreography: basic steps in high resolution NMR. Sausalito, Calif. : University Science Books, 1996.

8. Liang Z-P, Lauterbur PC. Principles of magnetic resonance imaging: a signal processing perspective. New York: IEEE Press; 2000.

9. Haacke EM. Magnetic resonance imaging: physical principles and sequence design. New York: Wiley; 1999.

10. Glover GH, Hayes CE, Pelc NJ, Edelstein WA, Mueller OM, Hart HR, Hardy CJ, O'Donnell M, Barber WD. Comparison of linear and circular polarization for magnetic resonance imaging. J Magn Reson 1985;64:255-270.

11. Takahashi M, Uematsu H, Hatabu H. MR imaging at high magnetic fields. Eur J Radiol 2003;46(1):45-52.

12. Vaughan JT, Garwood M, Collins CM, Liu W, DelaBarre L, Adriany G, Andersen P, Merkle H, Goebel R, Smith MB, Ugurbil K. 7T vs. 4T: RF power, homogeneity, and signal-to-noise comparison in head images. Magn Reson Med 2001;46(1):24-30.

13. Uematsu H, Dougherty L, Takahashi M, Butler NS, Song HK, Ohno Y, Gefter WB, Schnall MD, Hatabu H. A direct comparison of signal behavior between 4.0 and 1.5 T: a phantom study. Eur J Radiol 2003;45(2):154-159.

14. Callaghan PT. Principles of nuclear magnetic resonance microscopy: New York: Oxford University Press; 1991.

15. Kim DS, Garwood M. High-field magnetic resonance techniques for brain research. Curr Opin Neurobiol 2003;13(5):612-619.

16. Franke C, van Dorsten FA, Olah L, Schwindt W, Hoehn M. Arterial spin tagging perfusion imaging of rat brain: dependency on magnetic field strength. Magn Reson Imaging 2000;18(9):1109-1113.

17. Gati JS, Menon RS, Ugurbil K, Rutt BK. Experimental determination of the BOLD field strength dependence in vessels and tissue. Magn Reson Med 1997;38(2):296-302.

18. Hall WA, Liu H, Martin AJ, Pozza CH, Maxwell RE, Truwit CL. Safety, efficacy, and functionality of high-field strength interventional magnetic resonance imaging for neurosurgery. Neurosurgery 2000;46(3):632-641.

19. Kruger G, Kastrup A, Glover GH. Neuroimaging at 1.5 T and 3.0 T: comparison of oxygenation-sensitive magnetic resonance imaging. Magn Reson Med 2001;45(4):595-604.

20. Marti-Bonmati L, Kormano M. MR equipment acquisition strategies: low-field or high-field scanners. Eur Radiol 1997;7 Suppl 5:263-268.

21. Norris DG, Zysset S, Mildner T, Wiggins CJ. An investigation of the value of spin-echo-based fMRI using a Stroop color-word matching task and EPI at 3 T. Neuroimage 2002;15(3):719-726.

22. Rutt BK, Lee DH. The impact of field strength on image quality in MRI. J Magn Reson Imaging 1996;6(1):57-62.

23. Wang J, Alsop DC, Li L, Listerud J, Gonzalez-At JB, Schnall MD, Detre JA. Comparison of quantitative perfusion imaging using arterial spin labeling at 1.5 and 4.0 Tesla. Magn Reson Med 2002;48(2):242-254.

24. Yacoub E, Shmuel A, Pfeuffer J, Van De Moortele PF, Adriany G, Andersen P, Vaughan JT, Merkle H, Ugurbil K, Hu X. Imaging brain function in humans at 7 Tesla. Magn Reson Med 2001;45(4):588-594.

25. Yacoub E, Duong TQ, Van De Moortele PF, Lindquist M, Adriany G, Kim SG, Ugurbil K, Hu X. Spin-echo fMRI in humans using high spatial resolutions and high magnetic fields. Magn Reson Med 2003;49(4):655-664.

26. Yang Y, Wen H, Mattay VS, Balaban RS, Frank JA, Duyn JH. Comparison of 3D BOLD functional MRI with spiral acquisition at 1.5 and 4.0 T. Neuroimage 1999;9(4):446-451.

27. Di Costanzo A, Trojsi F, Tosetti M, Giannatempo GM, Nemore F, Piccirillo M, Bonavita S, Tedeschi G, Scarabino T. High-field proton MRS of human brain. Eur J Radiol 2003;48(2):146-153.

28. Bottomley PA. NMR imaging techniques and applications: a review. Rev Sci Instrum 1982;53(9):1319-1337.

29. Alecci M, Collins CM, Smith MB, Jezzard P. Radio frequency magnetic field mapping of a 3 Tesla birdcage coil: experimental and theoretical dependence on sample properties. Magn Reson Med 2001;46(2):379-385.

30. Collins CM, Li S, Smith MB. SAR and B1 field distributions in a heterogeneous human head model within a birdcage coil. Specific energy absorption rate. Magn Reson Med 1998;40(6):847-856.

31. Collins CM, Smith MB. Signal-to-noise ratio and absorbed power as functions of main magnetic field strength, and definition of "90 degrees " RF pulse for the head in the birdcage coil. Magn Reson Med 2001;45(4):684-691.

32. Collins CM, Yang QX, Wang JH, Zhang X, Liu H, Michaeli S, Zhu XH, Adriany G, Vaughan JT, Anderson P, Merkle H, Ugurbil K, Smith MB, Chen W.

Different excitation and reception distributions with a single-loop transmit-receive surface coil near a head-sized spherical phantom at 300 MHz. Magn Reson Med 2002;47(5):1026-1028.

33. Ibrahim TS, Lee R, Baertlein BA, Abduljalil AM, Zhu H, Robitaille PM. Effect of RF coil excitation on field inhomogeneity at ultra high fields: a field optimized TEM resonator. Magn Reson Imaging 2001;19(10):1339-1347.

34. Robitaille PM, Abduljalil AM, Kangarlu A, Zhang X, Yu Y, Burgess R, Bair S, Noa P, Yang L, Zhu H, Palmer B, Jiang Z, Chakeres DM, Spigos D. Human magnetic resonance imaging at 8 T. NMR Biomed 1998;11(6):263-265.

35. Yang QX, Wang J, Zhang X, Collins CM, Smith MB, Liu H, Zhu XH, Vaughan JT, Ugurbil K, Chen W. Analysis of wave behavior in lossy dielectric samples at high field. Magn Reson Med 2002;47(5):982-989.

36. Roschmann P. Radiofrequency penetration and absorption in the human body: limitations to high-field whole-body nuclear magnetic resonance imaging. Med Phys 1987;14(6):922-931.

37. Haase A, Odoj F, Kienlin MV, Warnking J, Fidler F, Weisser A, Nittka M, Rommel E, Lanz T, Kalusche B, Griswold M. NMR probeheads for i*n vivo* applications. Concepts in Magnetic Resonance 2000;12(6):361-388.

38. Ginsberg DM, Melchner MJ. Optimum geometry of saddle shaped coils for generating a uniform magnetic field. Rev Sci Instrum 1970;41(1):122-123.

39. Schneider HJ, Dullenkopf P. Slotted tube resonator: A new NMR probe head at high observing frequencies. Rev Sci Instrum 1977;48(1):68-73.

40. Alderman DW, Grant DM. An efficient decoupler coil design which reduces heating in conductive samples in superconducting spectrometers. J Magn Reson 1979;36:447-451.

41. Doty FD, Entzminger G, Jr., Hauck CD. Error-tolerant RF litz coils for NMR/MRI. J Magn Reson 1999;140(1):17-31.

42. Fourikis N. Advanced array systems, applications and RF technologies. San Diego: Academic Press; 2000.

43. Stutzman WL, Thiele GA. Antenna theory and design. New York: Wiley; 1981.

44. Teramoto K. Exact inverse problem solution in digital beam former. In: IECON '90., Proceedings of the 16th Annual Conference of IEEE; Pacific Grove, CA, 1990; p. 244.

45. Mori K, Arai H, Qian Y, Itoh T. Direct conversion receiver for digital beamforming at 8.45 GHz. In: Microwave Symposium Digest, 2001 IEEE MTT-S International; Phoenix, AZ, 2001; 1375-1378.

46. Kang B-S, Ku B-J, Ahn D-S. Ka band active phase array antenna with digital beam former for the haps systems. In: Proceedings of the 14th International Symposium on PIMRC; Beijing, 2003; 2475-2479.

47. Benjamin R, Zaglanikis CD, Seeds AJ. Optical beam former for phased arrays with independent control of radiated frequency and phase. Electronics Letters 1990;26(22):1853-1855.

48. Zaglanikis CD, Benjamin R, Seeds AJ. Optical beam-former for microwave phased array antennas. In: IEE Colloquium on Microwave Optoelectronics; London, 1990. 16/1-16/6.

49. Chang K, York RA, Hall PS, Itoh T. Active integrated antennas. In: IEEE Trans MTT, 2002;50(3):937-944.

50. Parini CG. What are active integrated antennas? Can successful CAD be achieved? In: Symposium on EDMO; London, 1999; 53-57.

51. Pobanz CW, Itoh T. Active integrated antennas. IEEE Potentials, 1997;16(2):6-10.

52. Lin J, Itoh T. Active integrated antennas. IEEE Trans. MTT, 1994;42(12):2186-2194.

53. Chang K, Hummer KA, Gopalakrishnan GK. Active radiating element using FET source integrated with microstrip patch antenna. Electronics Letters 1988;24(21):1347-1348.

54. Balanis CA. Antenna theory: analysis and design. New York: Harper & Row; 1982.

55. Balanis CA. Antenna theory: a review. Proc IEEE 1992;80(1):7-23.

56. Ibrahim TS, Lee R, Baertlein BA, Kangarlu A, Robitaille PL. Application of finite difference time domain method for the design of birdcage RF head coils using multi-port excitations. Magn Reson Imaging 2000;18(6):733-742.

57. Cripps SC. RF power amplifiers for wireless communications. Boston: Artech House; 1999.

58. Denyer CW, Lidgey FJ, Zhu QS, McLeod CN. A high output impedance current source. Physiol Meas 1994;15 Suppl 2a:A79-A82.

59. Hella MM, Ismail M. RF CMOS power amplifiers: theory, design, and implementation. Boston: Kluwer Academic Publishers; 2002.

60. Krauss HL, Bostian CW, Raab FH. Solid state radio engineering: New York: Wiley; 1980.

61. Pothecary N. Feedforward linear power amplifiers. Boston: Artech House; 1999.

62. Becciolini R. AN721: Impedance matching networks applied to RF power transistors. RF device data. 5 ed. Volume 2: Phoenix: Motorola Inc.; 1988. 7-82-7-92.

63. Jin J, Shen G, Perkins T. On the field inhomogeneity of a birdcage coil. Magn Reson Med 1994;32(3):418-422.

64. Bottomley PA, Andrew ER. RF magnetic field penetration, phase shift and power dissipation in biological tissue: Implications for NMR imaging. Phys Med Biol 1978;23(4):630-643.

65. Chen J, Feng Z, Jin JM. Numerical simulation of SAR and B1-field inhomogeneity of shielded RF coils loaded with the human head. IEEE Trans Biomed Eng 1998;45(5):650-659.

66. Hardy CJ, Cline HE. Spatial localization in two dimensions using NMR designer pulses. J Magn Reson 1989;82:647-654.

67. Hardy CJ, Cline HE. Broadband nuclear magnetic resonance pulses with two-dimensional spatial selectivity. J Appl Phys 1989;66(4):1513-1516.

68. Pauly J, Nishimura D, Macovski A. A linear class of large tip-angle selective excitation pulses. J Magn Reson 1989;82:571-587.

69. Pauly J, Nishimura D, Macovski A. A k-space analysis of small-tip-angle excitation. J Magn Reson 1989;81:43-56.

70. Pauly JM, Hu BS, Wang SJ, Nishimura DG, Macovski A. A three-dimensional spin-echo or inversion pulse. Magn Reson Med 1993;29(1):2-6.

71. Katscher U, Bornert P, Leussler C, van den Brink JS. Transmit SENSE. Magn Reson Med 2003;49(1):144-150.

APPENDIX A

THE RF POWER MOSFET

Field Effect Transistors (FET) are a class of three terminal solid state devices in which the current flow between a pair of terminals, the drain and source, is regulated by an electric field. The electric field is created by the application of a control voltage to the third terminal called the gate. The Metal-Oxide-Semiconductor FET (MOSFET) is a special class of FET's where the electric field is created due to the formation of a MOS capacitor. In this appendix is given a summary of the fabrication process and the DC characteristics of the MOSFET. The MOSFET DC characteristics are the basis upon which the operational principles of a MOSFET RF amplifier are explained.

Fabrication of a power MOSFET

The RF power MOSFET is fabricated on a silicon substrate called a die. MOSFET die fabrication involves several steps of solid state processes, which can be broadly summarized into four steps. These are illustrated by the schematics in Fig. A1, in the development of an N-channel enhancement mode MOSFET.

The first step in the fabrication process starts with a p-type substrate, in which the holes are the majority carriers and the electrons, the minority carriers. This is shown in Fig. A1a.

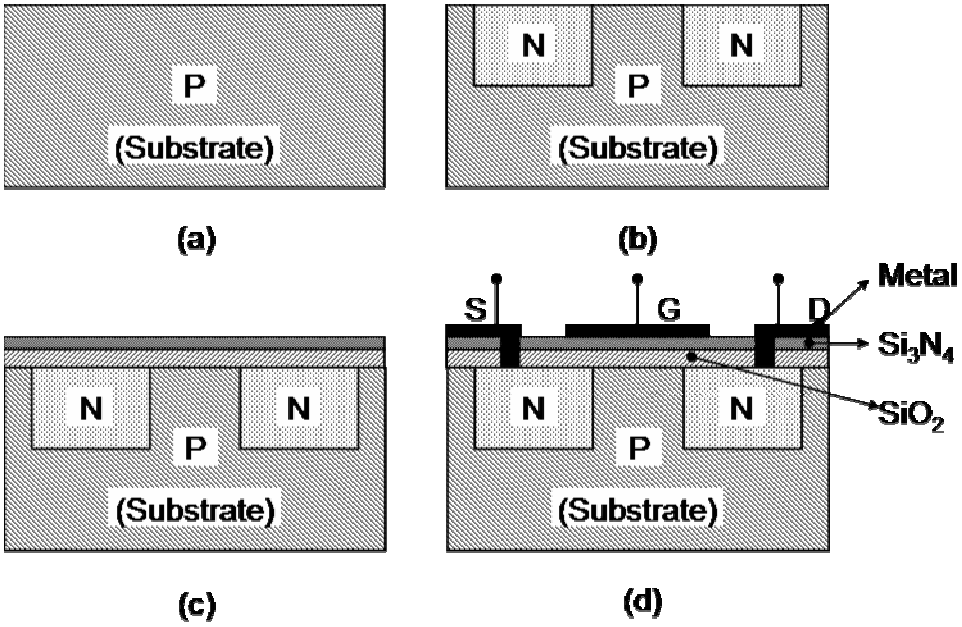

FIG. A1. Steps involved in the fabrication of the MOSFET. Starting with the p-type substrate (a), the source and drain regions are formed by the diffusion of n-type wells into the substrate (b). The third step involves the deposition of the insulating oxide layer and the passivating nitride layer (c) and the final step involves the metallization in order to develop the gate, drain and source contacts (d).

Next, two low resistivity n-type regions are diffused into the p-type substrate as shown in Fig. A1b. These form the drain and source regions of the MOSFET. The region between the drain and the source is where the channel is formed. The process of channel formation is explained in the following section.

Next, a thin layer of Silicon dioxide is deposited on the surface of the die as shown in Fig. A1c. The characteristics of the MOSFET are very sensitive to the purity and thickness of the oxide layer. Hence, these two parameters are carefully controlled during the deposition of the oxide. The oxide layer is also prone to contamination by sodium ions and moisture that are known to be present in varying degrees of concentration in the atmosphere. The oxide is therefore passivated with a layer of Silicon Nitride, which is known to be impervious to sodium ions and moisture.

In the final fabrication step, holes are etched into the oxide and nitride layers to allow for metallic contact with the drain and source regions. Metal is overlaid on the insulator, covering the entire channel region, to form the gate terminal. Simultaneously, metallic contact is made with the drain and source regions as shown in Fig. A1d thus forming the drain and source terminals

When the conduction of current from the drain to source is facilitated by the formation of an n-type channel in a p-type substrate, the MOSFET is classified as an N-Channel Enhancement mode MOSFET. In this type of device, the drain is positive with respect to the source and the gate must be biased to a positive voltage to the source for the drain source current to flow. This is the most commonly used MOSFET in the design

of modern solid state amplifiers. Table A1 is a list of useful symbols and their definitions, commonly used in a discussion of MOSFETs and RF amplifiers.

Table A1

Symbols used in the discussion of MOSFETs and RF amplifiers and their definitions.

Symbol	Definition
C_{DS}	Drain-source capacitance
C_{DG}	Drain-gate capacitance (same as C_{rs})
C_{GS}	Gate-Source capacitance
C_{is}	Input capacitance, common source
C_{os}	Output capacitance, common source
C_{rs}	Feedback capacitance, common source
g_{fs}	Forward transconductance
I_D	On state drain current
I_{DSS}	Drain-source leakage current
I_{om}	Output RF current amplitude
$R_{DS(on)}$	On-state drain-source resistance
R_L	Load resistance
θ	Angular time in radians; $\theta=\omega t$
$V_{BR(DSS)}$	Drain-source reverse bias breakdown voltage
V_{DSat}	Drain-source saturation voltage

Symbol	Definition
V_{DD}	Drain DC supply voltage
V_{DS}	Drain-source voltage
$V_{DS}(\theta)$	Drain-source instantaneous RF voltage
V_{GG}	Gate DC supply voltage
V_{GS}	Gate-source voltage
$V_{GS}(\theta)$	Gate-source instantaneous RF voltage
V_{im}	Input RF voltage amplitude
V_{om}	Output RF voltage amplitude

DC characteristics of the MOSFET

The symbol used to represent MOSFETs is shown in Fig. A2a. Fig. A2b is a schematic of a test circuit that is commonly used to obtain the DC characteristics of a MOSFET. Variable DC voltage sources, V_{GG} and V_{DD}, are connected to the gate and drain terminals of the MOSFET, respectively. The source terminal of the MOSFET is grounded, resulting in the commonly used "common source" configuration. The ammeter A_D and voltmeters V_G and V_D are used to measure I_D, V_{GS} and V_{DS} respectively.

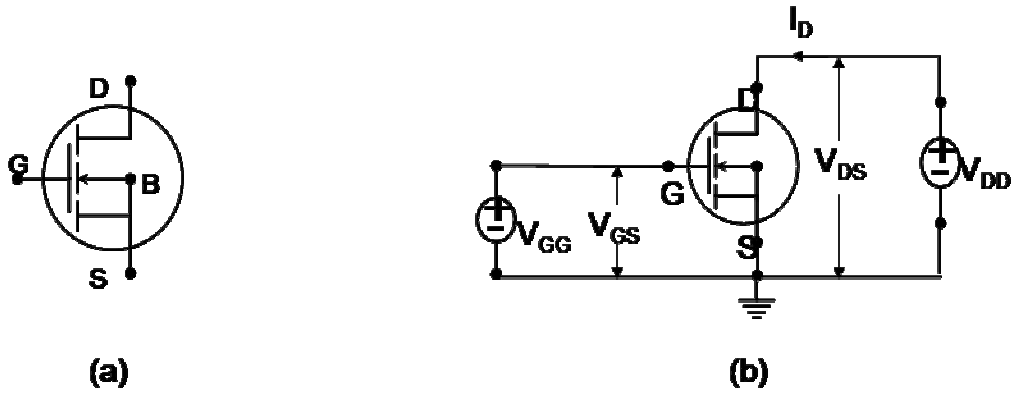

FIG. A2. Circuit used to obtain the DC characteristics of the MOSFET. (a) The symbolic representation shows the gate (G), drain (D), source (S) and bulk (B) contacts. (b) is the schematic of the curve tracer circuit which is used to determine the DC characteristics of the MOSFET.

When V_G is increased from zero to some positive value, V_{GG} (of the order of a few volts), holding V_D at a constant large value, V_{DD} (of the order of a few tens of volts), a plot of I_D against V_{GS} results in the characteristic curve of Fig. A3. This curve is called the "transfer curve" of the MOSFET. The transfer curve shows zero I_D for $V_{GS} < V_T$, a small increase in I_D for $V_T < (V_{GS} - V_T) < V_L$ and a large, linear increase in I_D for $V_L < (V_{GS} - V_T) < V_U$. The forward transconductance of the MOSFET is commonly defined for the linear region of the transfer curve as

$$g_{fs} = \frac{\Delta I_D}{\Delta V_{GS}} \qquad [A.1]$$

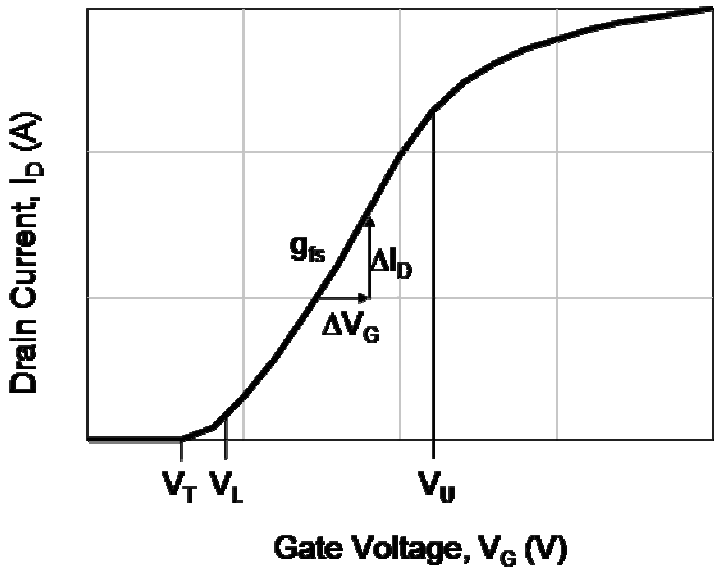

FIG. A3. Transfer curve of MOSFET. This shows the Drain current flow for any applied gate voltage.

In the design of RF amplifiers, the transfer curve is used to define the quiescent (or operating) point of the RF amplifier. The RF behavior of the MOSFET is based on the periodic traversal of the transfer curve corresponding to the periodic swing of the gate voltage.

When V_G is increased in steps from zero to V_{GG}, with V_D varied from zero to V_{DD}, plots of I_D against V_{DS} for each V_G, result in the characteristic curves of Fig. A4. These curves are called the I-V curves of the MOSFET.

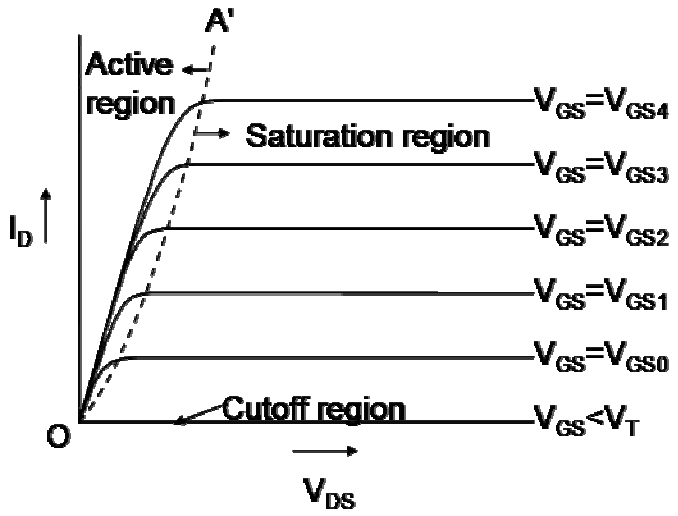

FIG. A4. I-V curves of the MOSFET. Each curve corresponds to a specific setting of V_{GS}. The three regions of operation are shown.

Three distinct regions of operation are defined in the above characteristic curves of the MOSFET.

- When $V_{GS} < V_T$, I_D is zero and the MOSFET is said to be "cut off". This region is indicated in Fig. A4 and symbolically represented in Fig. A5a.
- When $V_{GS} > V_T$ and $V_{DS} < V_{DSat}$, I_D increases linearly as V_{DS}. The projection of OA' on the abscissa in Fig. A4 represents the range of V_{DSat} over the range of V_G. This region, called the active region, is symbolically represented as a series resistor, $r_{DS(on)}$, in the drain-source path, in Fig. A5b.
- When $V_{GS} > V_T$ and $V_{DS} > V_{DSat}$, I_D changes negligibly with V_D. The MOSFET behaves as a true current source in this region, called the saturation region, as shown symbolically in Fig. A5c.

It should be noted that the transfer curve of the MOSFET is defined in the saturation region of the I-V curve.

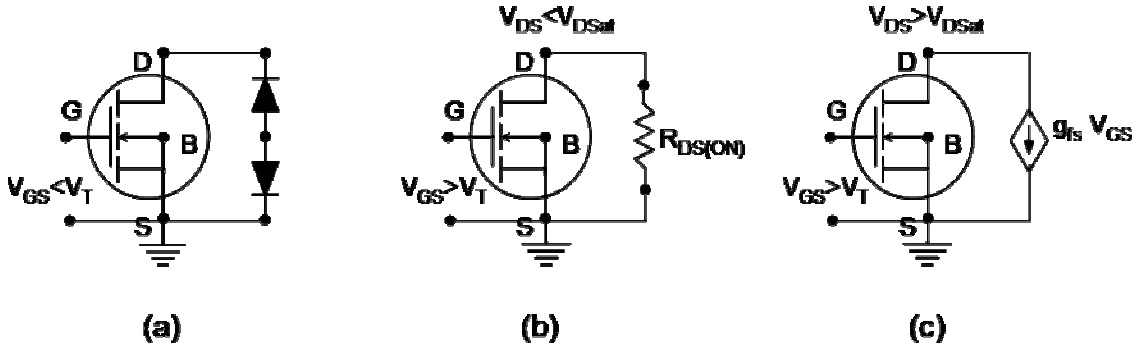

FIG. A5. Symbolic representation of the three MOSFET states.

The structure of the MOSFET results in the formation of parasitic capacitances that are not significant at low frequencies but have significant effect on the MOSFET response at RF. The origins of these capacitances are shown in Fig. A6. C_{DS} is a parasitic capacitance that is formed as a result of junction capacitance of the reverse biased diode at the interface of the drain and substrate. C_{DS} depends on the applied reverse voltage across the diode. C_{GS} and C_{GD} are parasitic capacitances that are formed as a result of overlap of the gate metallization over the drain and source regions and these are not voltage dependent.

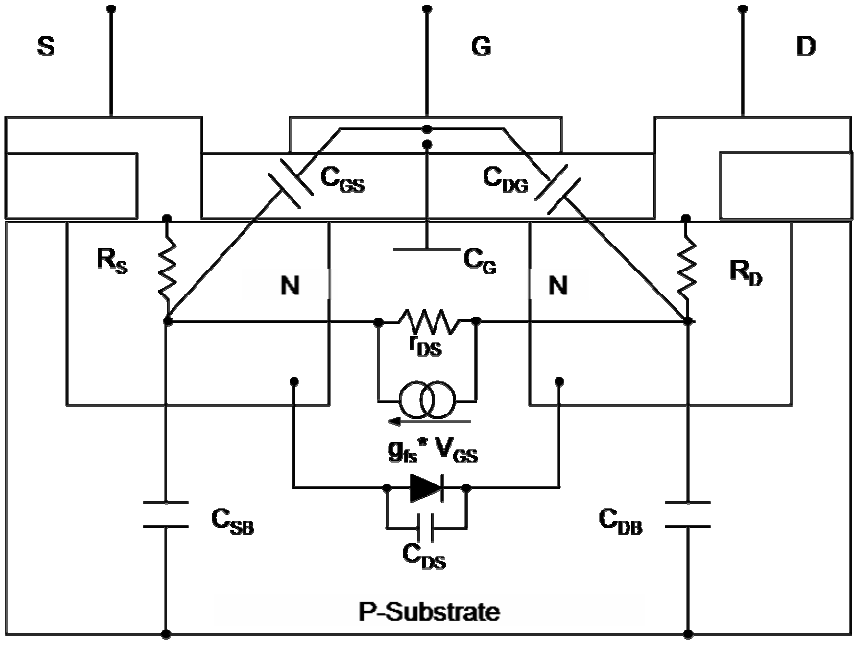

FIG. A6. Parasitic capacitances of the MOSFET. C_{GS} and C_{DG} are the parasitic capacitances formed due to overlap of the gate metallization over the source and drain regions respectively. C_{DS} is the drain-source capacitance formed due to the reverse biased diode at the drain-substrate interface.

MOSFET datasheets generally specify output capacitance, C_{os}, input capacitance, C_{is} and feedback capacitance, C_{rs}.

- C_{os} is measured with V_{GG} set to ground potential and is given by

$$C_{os} = C_{DS} + C_{GD} \qquad [A.2]$$

  C_{os} appears as a capacitance across the output terminals of the MOSFET. Since the internal resistance of the MOSFET current source is very high, the output impedance of the MOSFET is essentially the output capacitance.

- C_{is} is measured with the drain shorted to the sourced terminal and appears across the input terminals of the MOSFET. C_{is} is given by

$$C_{is} = C_{GS} + C_{GD} \qquad [A.3]$$

  C_{is} does not vary significantly with the applied gate voltage. The effect of C_{is} is to reduce the input impedance of the MOSFET. This makes matching to a 50 ohm generator more difficult.

- C_{rs} is the feedback capacitance and is the same as C_{GD}. Through proper layout of the MOSFET, this capacitance is minimized.

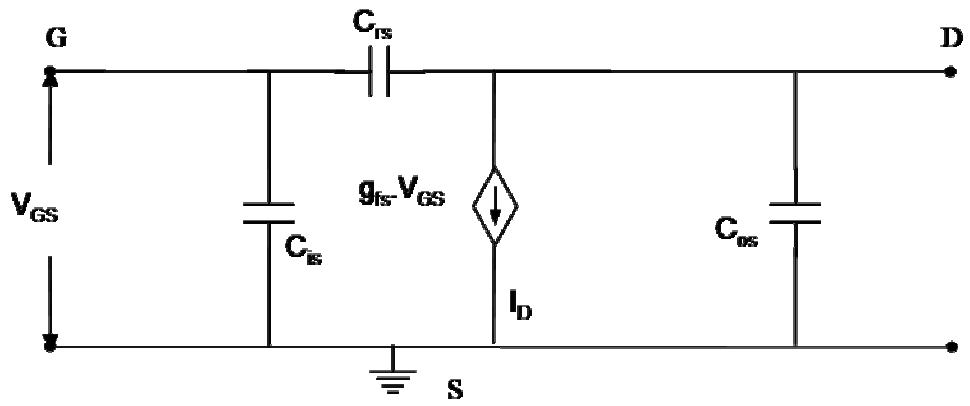

FIG. A7. Equivalent circuit of the MOSFET. This figure depicts the MOSFET as a voltage controlled current source. The parasitic capacitances between the MOSFET terminals are also shown.

From the above description of the MOSFET, it may then be conveniently represented by the simplified equivalent circuit shown in Fig. A7. Fig. A7 depicts the MOSFET as a voltage controlled current source with the parasitic capacitors that affect its performance at RF.

APPENDIX B

RF POWER AMPLIFICATION

Linear amplification of RF power is achieved when the MOSFET behaves as a true current source. This is possible only when $V_{DS} > V_{DSat}$ at any instant of time. Here, linearity is a measure of the extent to which the output waveform is a faithful reproduction of the input waveform.

Another factor that determines the linearity of an RF amplifier is the quiescent point about which the MOSFET operates. The quiescent point is that value of constant drain current, denoted by I_{DQ}, which corresponds to a constant V_{GS}, as defined by the transfer curve of the MOSFET. Fig. B1 is a reproduction of the transfer curve of Fig. A3 with four commonly used values of V_{GS} and their corresponding I_{DQ} marked out.

RF power amplifier classes

When $V_{GS} = V_{GS(A)}$, $I_{DQ} = I_{DQ(A)}$ is a large constant current of the order of a few amps for a high power device. However, application of an RF input voltage (Fig. B2a), whose amplitude is less than $(V_{GS(A)} - V_T)$ ensures that the MOSFET never goes into the cut off region. Conduction angle is 360^o and the amplifier is very linear. RF amplifiers of this class are known as Class A amplifiers.

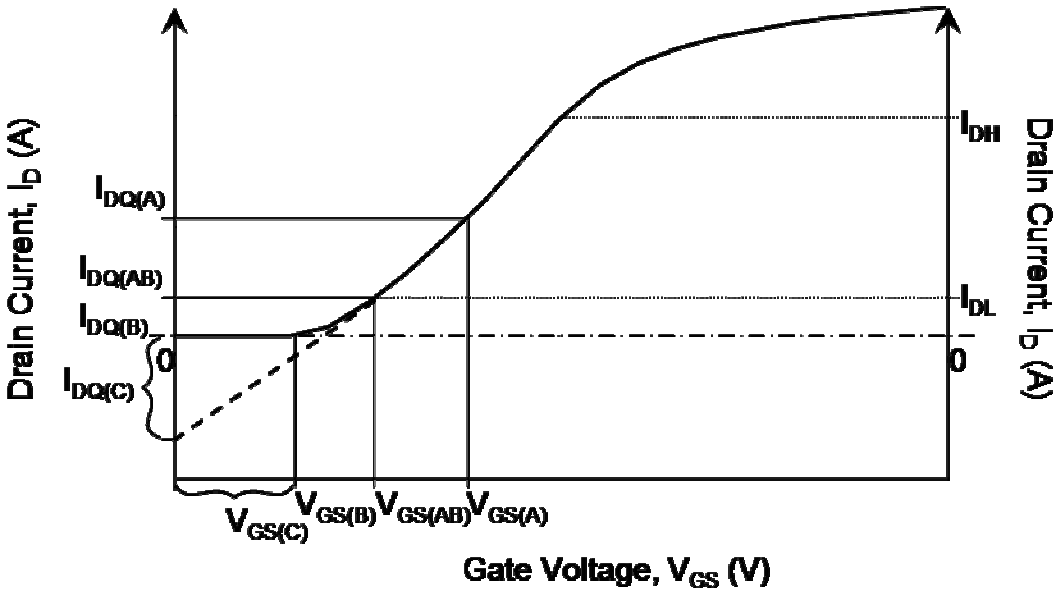

FIG. B1. Various gate bias points for linear amplification.

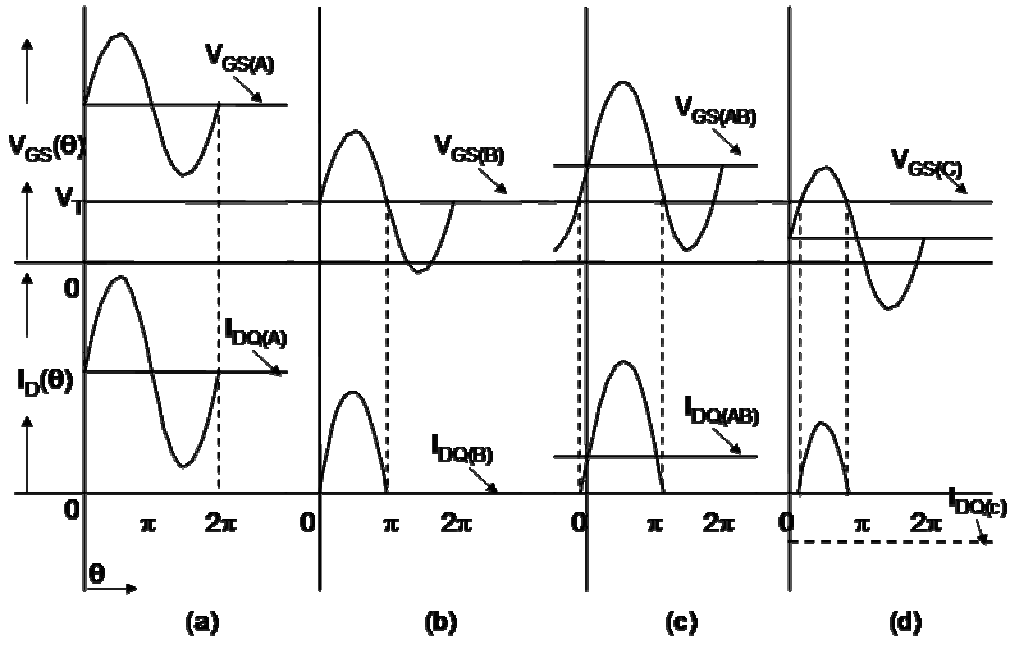

FIG. B2. Upper half of the figure represents input RF voltage. The lower half represents output current. The bias points of Class A (a); Class B (b); Class AB (c) and Class C (d) amplifiers are shown.

When $V_{GS} = V_{GS(B)} = V_T$, $I_{DQ} = 0A$, V_{GS} is less than V_T for half the sinusoidal cycle as shown in Fig. B2b. The MOSFET therefore is ON for only the positive half of the input voltage sinusoid. It is said to have a conduction angle of 180^o. The sinusoidal waveform on the output is obtained either by the use of a push-pull configuration in case of a broadband amplifier or by a tuned output network in case of a narrow-band amplifier. Such an RF amplifier is known as class B amplifier.

For class AB amplifiers, $V_{GS(B)} < (V_{GS} = V_{GS(AB)}) < V_{GS(A)}$ and $I_{DQ} = I_{DQ(AB)}$. Usually, $V_{GS(AB)}$ is set at the beginning of the linear portion of the transfer curve. The conduction angle is between 180^o and 360^o, as shown in Fig. B2c.

For class C amplifiers, $0 < V_{GS(C)} < V_T$ and $I_{DQ} = I_{DQ(C)}$, which is shown to be negative in both Fig. B1 and Fig. B2d. However, in practice, $I_{DQ(C)} = 0A$. The conduction angle for a class C amplifier usually is between 90^o and 180^o. Class C amplifiers are usually used as high efficiency tuned amplifiers.

Principle of operation of RF power amplifiers

The principle of operation of a MOSFET RF amplifier can be analyzed on the basis of the DC characteristics of the MOSFET. For simplicity, a class A amplifier will be analyzed in this section. Other amplifier classes could be analyzed on similar lines.

The schematic of a basic common source RF amplifier is shown in Fig. B3. Table B1 is a list of symbols that have been used in the schematic and their definitions.

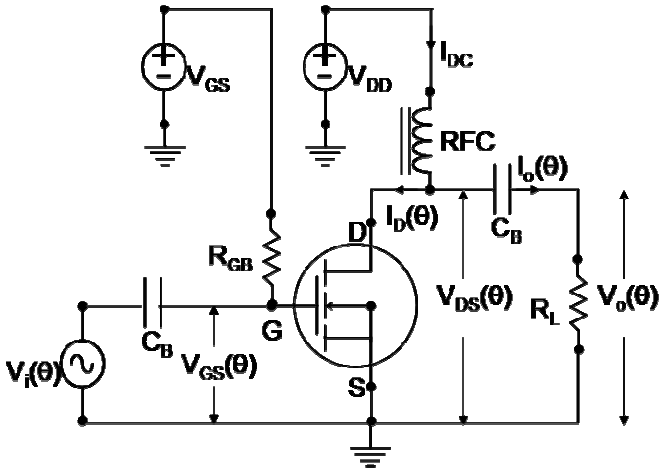

FIG. B3. Schematic of the basic RF amplifier. The parasitic output capacitances described in appendix A are ignored here. In reality, the parasitic capacitances are compensated for and the load resistance represented by R_L is a virtual load resistance.

Table B1

Table of symbols used in RF amplifier design.

Symbol	Definition
C_b	DC block capacitor
I_{DC}	DC quiescent current drawn by MOSFET
$I_D(\theta)$	Time varying drain current
$I_o(\theta)$	Time varying load current
R_{GB}	Gate bias resistor
R_L	Load resistor
RFC	RF choke
V_{GG}	Gate DC supply voltage
V_{DD}	Drain DC supply voltage
$V_{GS}(\theta)$	Time varying gate-source voltage
$V_{DS}(\theta)$	Time varying drain-source voltage
$V_i(\theta)$	Time varying input voltage
$V_o(\theta)$	Time varying output voltage

In the schematic shown in Fig. B3, let the RF source produce a sinusoidal voltage $V_i(\theta)$ such that

$$V_i(\theta) = V_{im}\sin(\theta) \quad [B.1]$$

and

$$V_{GS}(\theta) = V_{GS} - V_{im}\sin(\theta) \quad [B.2]$$

For class A operation, $V_{im} < (V_{GS} - V_T)$ and hence $V_{GS}(\theta) > V_T$ for $t > 0$ and the entire voltage waveform presented to the gate lies in the linear region of the transfer curve. Multiplication of equation [B.2] with g_{fs} signifies amplification and yields

$$I_{DS}(\theta) = I_{DQ} - I_{om}\sin(\theta) \quad [B.3]$$

I_{DQ} flows through the RF choke and $I_{om}\sin(\theta)$ flows through the blocking capacitor into the load resistor, R_L, creating a voltage drop, $V_o(\theta)$, across it, given by

$$V_o(\theta) = R_L I_{om}\sin(\theta) = V_{om}\sin(\theta) \quad [B.4]$$

The power dissipated by R_L is the output power P_o, given by

$$P_o = \frac{I_{om}^2}{2R_L} = \frac{V_{om}^2}{2R_L} \quad [B.5]$$

From equation [B.4], it is clear that instantaneous drain-source voltage, $V_{DS}(\theta)$, is given by

$$V_{DS}(\theta) = V_{DD} + V_{om}\sin(\theta) \quad [B.6]$$

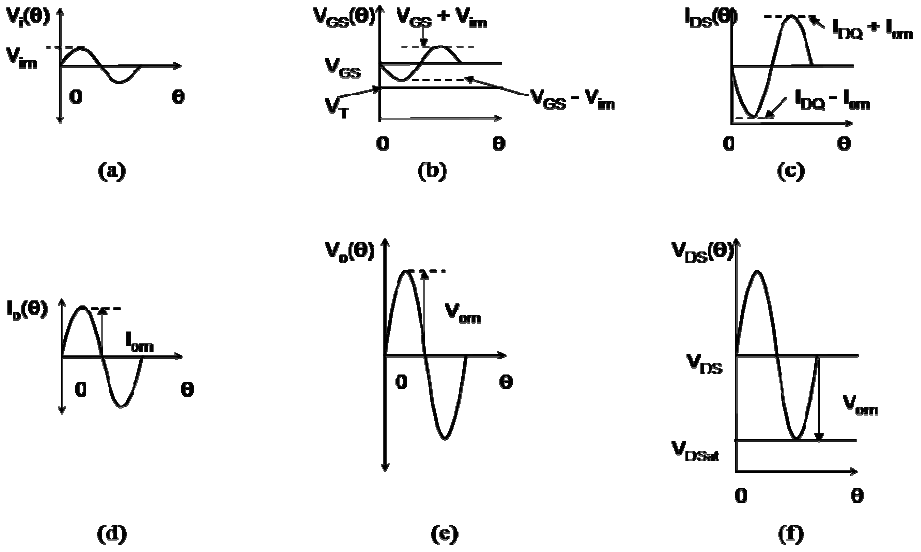

FIG. B4. Waveform diagram of Class A amplifier. (a) through (f) are pictorial representations of equations [B.1] through [B.6] except equation [B.5].

Equation [B.5] implies that the output power varies linearly as the amplitude of the output voltage swing. Since V_{om} itself varies linearly as R_L, equation [B.5] implies that when the MOSFET behaves as a current source, larger the load resistance, greater the output power. However, by virtue of the assertion that $V_{DS}(\theta) > V_{DSat}$ in order for the MOSFET to behave as a current source, equation [B.6] imposes an upper bound on V_{om} given by

$$V_{om} \leq V_{DD} - V_{DSat} \qquad [B.7]$$

From equation [B.6], it could be argued that V_{DD} could be increased arbitrarily to accommodate the condition imposed by equation [B.7]. However the avalanche breakdown voltage, $V_{BR(DSS)}$, of the reverse biased diode formed by the drain-substrate interface imposes an upper bound on V_{DD} as

$$V_{DD} < V_{BR(DSS)} - V_{om} \qquad [B.8]$$

From equation [B.5] and the conditions [B.7] and [B.8], the optimum value of R_L can be calculated as

$$R_L = \frac{\left(V_{DD} - V_{DSat}\right)^2}{2P_o} \qquad [B.9]$$

The waveform diagram shown in Fig. B4 is a step-by-step illustration of the amplification process of an input sinusoid as described by the above equations.

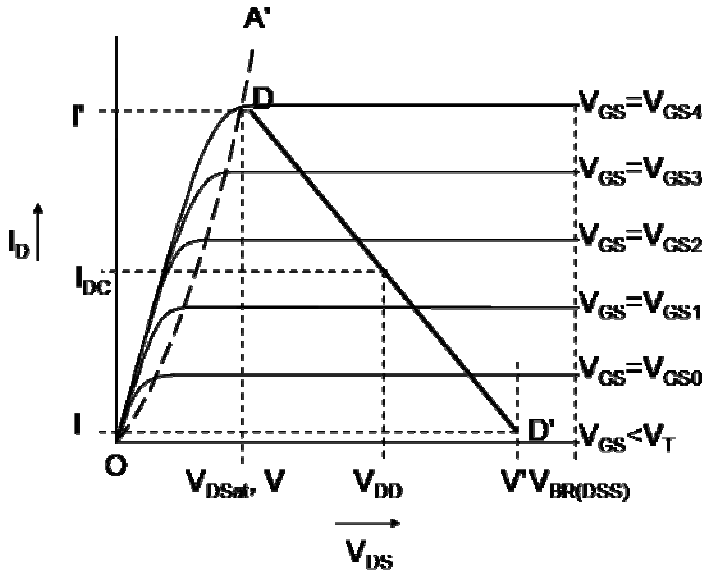

FIG. B5. Load-pull diagram for resistive load. DD′ is the locus of V_{DS} and I_{DS} during RF operation of the MOSFET. V_{DS} swing is represented by VV′. The I_{DS} swing is represented by II′. The lower limit for the V_{DS} swing is V_{DSat}. I_D swings about I_{DQ}, the quiescent current.

From the above analysis, the MOSFET may be described as a high resistance current driver. From Fig. B4c and Fig. B4f, it can be seen that the drain current is minimum at maximum voltage across the drain-source terminals and vice versa. Fig. B5 is an illustration of the operation of the RF amplifier based on the DC characteristics of the MOSFET. DD' represents the variation of I_D and V_{DS} with the sinusoidal variation of the gate voltage above the threshold voltage. Since I_D and V_{DS} for a pure resistive load are 180^o out of phase, DD' is a straight line as shown in Fig. B5. For a pure reactive load, DD' would be a perfect circle. For the mixed loads found in most practical situations, DD' would be an ellipse.

APPENDIX C

IMAGING RESULTS

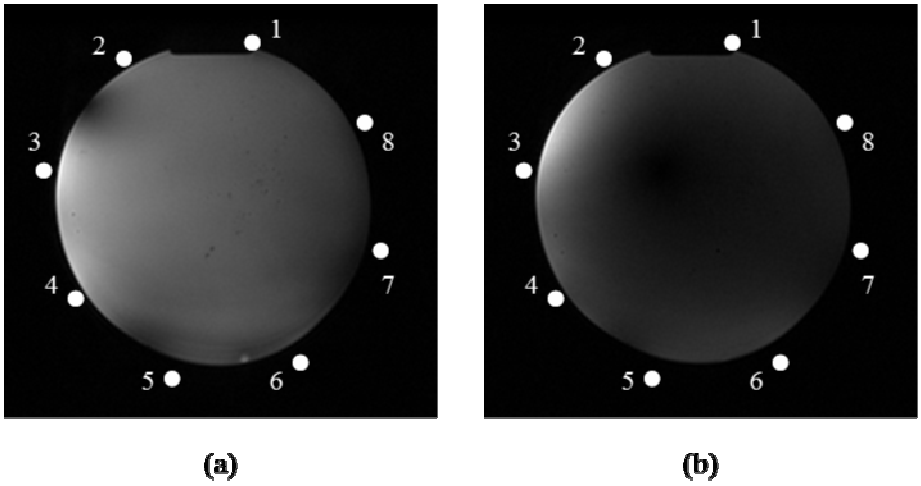

FIG. C1. Images obtained due to current in two adjacent rungs. Currents in rungs numbered 2 and 3 are set to the maximum amplitude of 1.65A. When the phase difference between the rungs is set to 0^{o} (a), field cancellation, defined by the dark spot, is seen in the region between the rungs. When the phase difference is set to 189^{o} (b), addition of fields is seen between the rungs while the fields are cancelled over the majority of the image.

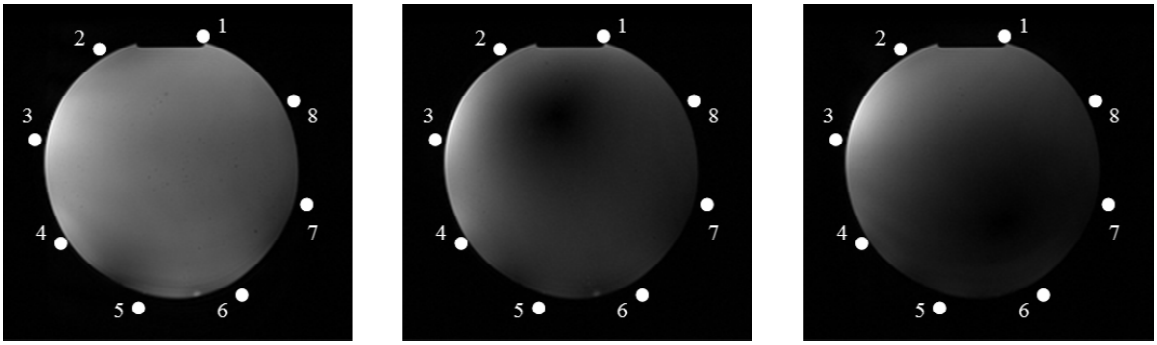

FIG. C2. Images obtained with rungs 1 and 3 active. The rungs are placed geometrically 90^{o} apart. Rungs 1 and 3 carry current of amplitude 1.65A with all other rungs turned off. When currents on rungs 1 and 3 are set with a phase difference of 90^{o} (a), a uniform image is obtained because the fields due to the two rungs are orthogonal to each other in space and time. When the phase difference is set to 0^{o} (b), there is a region between the two rungs within which the fields due to the two rungs cancel out as defined by the dark spot. When the phase difference is set to 180^{o} (c), the bright region between the rungs shows addition of the fields between the rungs as expected from a simple analysis of the fields from the right hand thumb rule and the fields cancel out everywhere else.

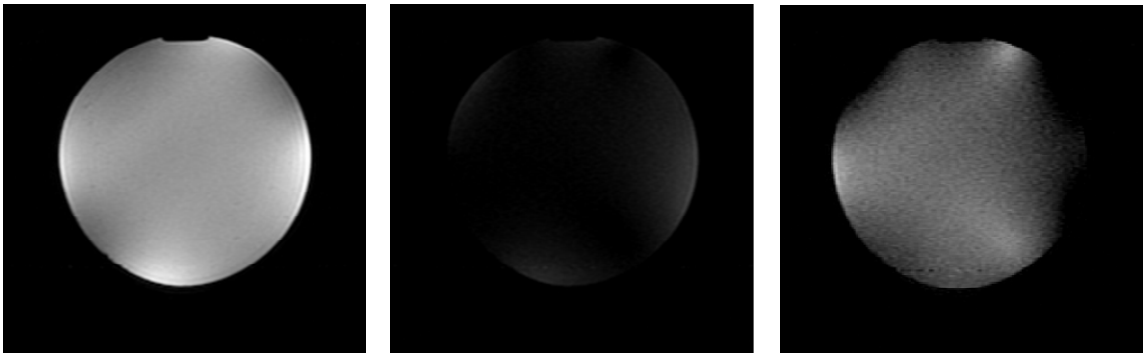

(a) (b) (c)

FIG. C3. Quadrature and anti-quadrature images. (a) shows quadrature mode excitation which means that the B_1 field is co-rotating with the nuclear magnetic spins. (b) shows anti-quadrature mode excitation which means that the B_1 field is counter-rotating with respect to the nuclear magnetic spins. Anti-quadrature mode should not yield any image when the B_1 fields are perfectly circularly polarized. (c) shows a subtraction image obtained by performing (a)-(b). This shows that except near the edges, the fields are circularly polarized. The circular polarization is degraded at the edges due to proximity to the conductors of the receive coil.

VITA

Mr. Krishna Kurpad was born to Mr. K. Nagaraj and Mrs. Geetha Nagaraj in Bangalore, India in January 1974. He received the degree of Bachelor of Engineering, majoring in electrical engineering, from the University of Mysore in November 1996. In 1997, he began pursuing a Ph.D. in electrical engineering from Texas A&M University. He received the degree in August 2004. His research, which is part of an on-going collaboration between Texas A&M University, the National Science Foundation and GE Medical Systems, focuses on the development of a transmit phased array antenna fed by RF current sources that is capable of near field pattern control. His area of expertise lies in the field of RF amplifier and RF coil design for Magnetic Resonance Imaging. In April of 2004, he became a Research Scientist with the Medical Physics group, Department of Radiology at the University of Wisconsin at Madison.

For further information, the author can be contacted at the address below:

Krishna Kurpad
10 Springview Ct. Apt C
Madison, WI 53704